High-Resolution Experiments of Flow Phenomena in Dead-ended Branch Lines for the Validation and Advancement of Computational Fluid Dynamics Modeling

by

John R. Downing

A dissertation submitted in partial fulfillment
of the requirements for the degree of
Doctor of Philosophy
(Nuclear Engineering and Radiological Sciences)
in the University of Michigan
2024

Doctoral Committee:

Professor Annalisa Manera, Co-Chair
Dr. Victor Petrov, Co-Chair
Professor Volker Sick
Professor Xiaodong Sun

John Downing

downingj@umich.edu

ORCID iD: 0000-0002-4122-6140

Dedication

To my wife, Nycole.

For your support, love, sacrifice, and patience.

Acknowledgements

I would like to thank my co-advisors, Annalisa Manera and Victor Petrov for their faith in me and their guidance through this process. Victor, your resourcefulness, hands-on approach, and knowledge made the lab an ideal learning environment.

I owe a great deal of thanks to my peers and colleagues over the years. Daniel Nunez, you never seemed to tire of my questions and always found a way to teach clearly. You were a great emotional and mental support during my time at Michigan. Zach Welker, you have been the friend I have needed for a long time. You have enriched my life in and out of the lab. To the others I have worked with in the research group (Julio, Jiaxin, Sunming, Benedikt, Aaron, Pei-Hsun, and others), thank you for your kinship and support.

Giancarlo Lenci and other industry partners that I had the pleasure of working with as I progressed in my degree, thank you for your patience and insight.

The U.S. Department of Energy's Nuclear Energy University Program and the University of Michigan's Rackham Merit Fellowship Program also deserve my gratitude for financial support during my degree work

Table of Contents

List of Tables

List of Figures

List of Abbreviations

BL	Branch Line
CFD	Computational Fluid Dynamics
CW	Clockwise
DH	Down-Horizontal
DNS	Direct Numerical Simulation
ECMFL	Experimental and Computational Multi-Phase Flow Laboratory
ECCS	Emergency Core Coolant System
EPRI	Electrical Power Research Institute
FEA	Finite Element Analysis
HCL	High-Capacity Loop (facility)
HX	Heat Exchanger
ID	Inner Diameter
LDV	Laser Doppler Velocimetry
LES	Large Eddy Simulation
NPP	Nuclear Power Plant
PB	Penetration Boundary
PIV	Particle Image Velocimetry
POD	Proper Orthogonal Decomposition
PWR	Pressurized Water Reactors
R1	Branch Line Region 1
R2	Branch Line Region 2
R3	Branch Line Region 3
RANS	Reynolds-averaged Navier–Stokes
ReBL – TF	Reactor Branch Line – Thermal Fatigue (facility)
RPL	Rectangular Profile Loop (facility)
SMC	Second Moment Closure
SSEF	Swirl Separate Effect Facility
TASCS	Thermal Stratification, Cycling, and Striping (program)
TF	Thermal Fatigue
TKE	Turbulent Kinetic Energy
UH	Up-Horizontal
VSC	Volumetric Self-calibration

Abstract

Thermal fatigue (TF) is one of the major degradation mechanisms that can lead to material failures affecting the safety relevant components of a nuclear power plant (NPP), such as the emergency core coolant system (ECCS) branch lines of the primary coolant circuit. Regarding ECCS piping, previous TF management programs and predictive computational models have proven insufficient. On the one hand, they appear to be overly conservative, leading to an unnecessarily large number of pipes screened for TF related issues, and on the other they do not capture all relevant physics. Correlations used to calculate the location of TF onset appear to be too case specific to be applied across diverse scenarios and configurations, while more advanced tools like computational fluid dynamics (CFD) models lack data for rigorous validation.

The previous body of experimental results was too coarse to meaningfully enhance the results of computational methods for predicting the location of TF onset in branch line piping across various geometries and NPP conditions. In the present dissertation, novel, high-resolution, high-fidelity quantitative measurements of flow fields in isolated branch lines are presented. The aim of building a robust database of such data is to aid in overcoming the deficiencies of past experiments, yielding a greater understanding of the associated flow phenomena and validating predictive CFD models. The present data were acquired utilizing four experimental facilities designed and constructed to systematically investigate the flow phenomena responsible for turbulence-induced TF in isolated branch lines, including scaling effects.

High-resolution measurements were obtained from the experimental facilities utilizing advanced measurement techniques such as particle image velocimetry. These measurements have clarified and solidified understanding of the flow phenomena present in dead-ended branch lines that are responsible for thermal fatigue. Comparing the results between multiple facilities has demonstrated that the complexity and demands of the measurement apparatus used to study the penetration of flow swirls in branch lines can be reduced significantly from what has previously been employed – i.e., a comparable penetrating flow swirl in a dead-ended branch line can be driven by a stirring paddle instead of a main line flow crossing the branch line opening. Quantitative measurements of the flow fields in the branch lines have aided the conclusion that Low-Re k-ε CFD models are sufficient for penetration depth predictive modeling, a stance that has been adopted by members of the NPP industry. Portions of the data presented are also being utilized in an international benchmark study in an effort to validate CFD models for penetrating flows in dead-ended branch lines.

Chapter 1 Introduction

Thermal fatigue (TF) is one of the major degradation mechanisms that can lead to material failures affecting the safety relevant components of a nuclear power plant (NPP), such as the emergency core coolant system (ECCS) branch lines of the primary coolant circuit [1]. Regarding ECCS piping, previous TF management programs and predictive computational models have proven insufficient. On the one hand, they appear to be overly conservative, leading to an unnecessarily large number of pipes screened for TF related issues, and on the other they do not capture all relevant physics. Correlations used to calculate the location of TF onset appear to be too case specific to be applied across diverse scenarios and configurations, while more advanced computational tools based on fluid dynamics (CFD) models lack data for rigorous validation.

The current body of experimental results is too coarse to meaningfully enhance the results of computational methods for predicting the location of TF onset in branch line piping across various geometries and NPP conditions [2]. High-resolution, high-fidelity measurements of flow fields and trends in particular branch line experiments can overcome this deficiency, as they would provide robust data for validating existing CFD models. The main objectives of this thesis are a) to build a high-resolution experimental database of the fluid-dynamic phenomena relevant to thermal-fatigue in branch lines where key flow structures are identified and quantified for physics discovery, yielding a better understanding of the underlying phenomena of thermal fatigue and b) to demonstrate how the novel experimental database can be used to validate high-fidelity computational methods and assess their predictive capabilities. Quantities of interest include the

magnitude of the turbulence-induced flow structures in an otherwise stagnant branch line, the decay of such flow structures, and their maximal penetration within the branch line.

1.1 General Background

Traditional pressurized water reactors (PWRs) require large networks of piping for the distribution of water, which acts as the power plant's primary coolant. Within these piping systems, branch lines are commonplace, as they are utilized to combine or divert flows as needed. Branch line junctions where flows are combined are commonly referred to as mixing tees (Figure 1-1 (a)), whereas those that divert a portion of a flow are simply referred to as T-junctions (Figure 1-1 (b)).

A number of mixing tees in nuclear power plants combine a supplementary flow of one temperature to a flow of a different temperature. Applications where mixing tees combine streams that vary in temperature have garnered a lot of attention over the years from researchers that have worked to quantify the downstream thermal mixing that occurs and the effects of local thermal cycling on piping materials [3, 4, 5, 6, 7] . However, this is not the only thermal fatigue scenario that plagues mixing tees in nuclear power plants (NPPs). The other common case is specific to a subset of mixing tees in NPPs where the branch line is predominantly dormant, having no flow intentionally driven through it during standard operation.

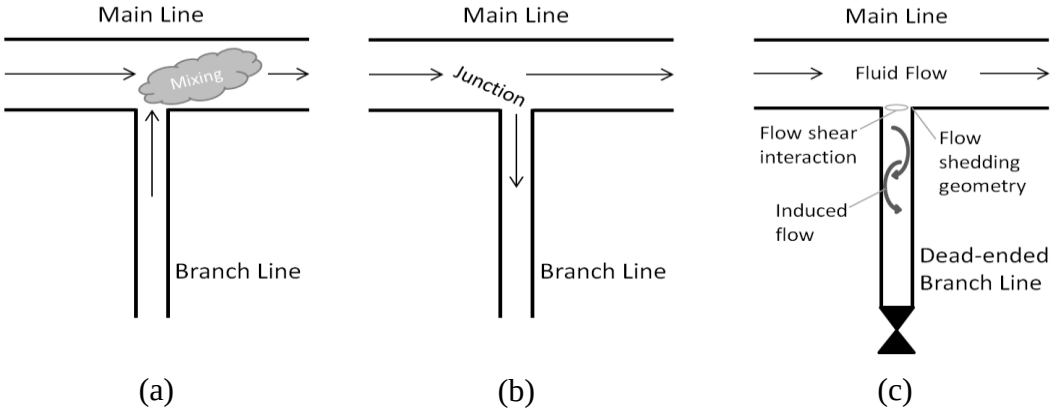

Figure 1-1 (a) Mixing tee where a branch line flow is combined with a main line flow. (b) T-junction where a portion of main line flow is diverted to a branch line. (c) Induced flow in the branch line due to shearing and shedding interactions of the main line flow.

As a part of the emergency core coolant system (ECCS), these dormant branch lines are

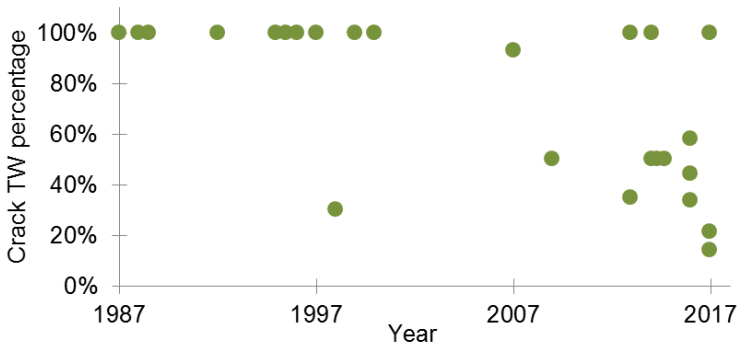

Figure 1-2 Crack through-wall (TW) percentage by date detected. EPRI MRP-146

sealed off by valves and do not supply coolant to mixing tees during normal operation. In this state, the fluid in a branch line would stagnate if it were not affected by the passing main line fluid at its junction. At the junction, the main line flow shears the branch line fluid, the main line flow boundary layer separates, and fluid is shed by the geometry of the downstream side of the branch line's opening (Figure 1-1 (c)). The resulting induced flow in the branch line is directly related to the phenomena that cause thermal stratification in the branch line and thermal fatigue in its piping wall [8, 9].

Due to the induced flow in the branch line, the hotter water of the main line (~300^{o} C) cycles into the branch line where it forms a thermal boundary with the stranded, cooler water (~25^{o} C). It is understood that this boundary occurs at the point in the branch line where the energy of the penetrating flow dissipates due to friction losses and competition with buoyancy forces. The location and temperature difference at the stratification boundary can also be affected by undetected valve leaks, allowing the ingress of the ECCS supply water into the branch line [10]. As this boundary depth fluctuates due to turbulence, the local pipe walls experience a cyclic change in temperature which fatigues the pipe wall material, leading to cracking and potentially failure if the cracks are not identified during maintenance operations.

Current management plans for predicting TF onset, monitoring at-risk components, and mitigating TF events in ECCS pipelines that affect plant safety and operations have proven insufficient to efficiently screen affected branch lines. In the last ten years, the U.S. has experienced at least 17 cracking events, which are precursors of loss of coolant accidents (Figure 1-2). As of 2023, the French Energy Utility (EDF) was conducting a mass screening of 200+ possible cracks across 56 NPPs due to a slew of recently detected piping cracks [11] [12]. Efforts to improve the accuracy of penetration boundary predictions using lower-cost computational fluid dynamic (CFD) models has proven ineffective as there is a lack of sufficiently high-resolution data to conduct validation tests on the various calibration scenarios. The available experimental data, as discussed in the following section, ranges from sparse, pointwise measurements captured by hot-wire anemometers, yaw probes, and vane-type sensors to dual flow component measurements from laser Doppler velocimetry setups and coarse particle image velocimetry.

1.2 Experimental Work Background

In 1992 and 1996 crack events occurred in branch lines of the French reactors Dampierre-2 and Dampierre-1 respectively, which caused Electricite de France (EDF) to expand their research into the phenomenon of turbulence-induced thermal fatigue in branch lines. A report authored in 1993 [13], showcased early efforts to identify the flow conditions that could cause TF in a dead-ended branch line. The research facility utilized a reduced and sectioned main line as shown in Figure 1-3. Using optically clear piping, researchers were able to determine the presence of a swirling corkscrew-like flow that penetrated he branch line (Figure 1-3 [13]). The rotation direction of the swirl was consistently the same with each experimental run, which was perplexing since there was no distinguishable geometric feature which appeared to dictate this behavior. In an attempt to alter the swirl direction, they manipulated the main line flow profile and placed obstructions near the junction of the tee in different studies. Neither scheme affected the corkscrew swirl direction but placing an obstruction at the upstream lip of the branch line junction did appear to change the flow swirl's magnitude.

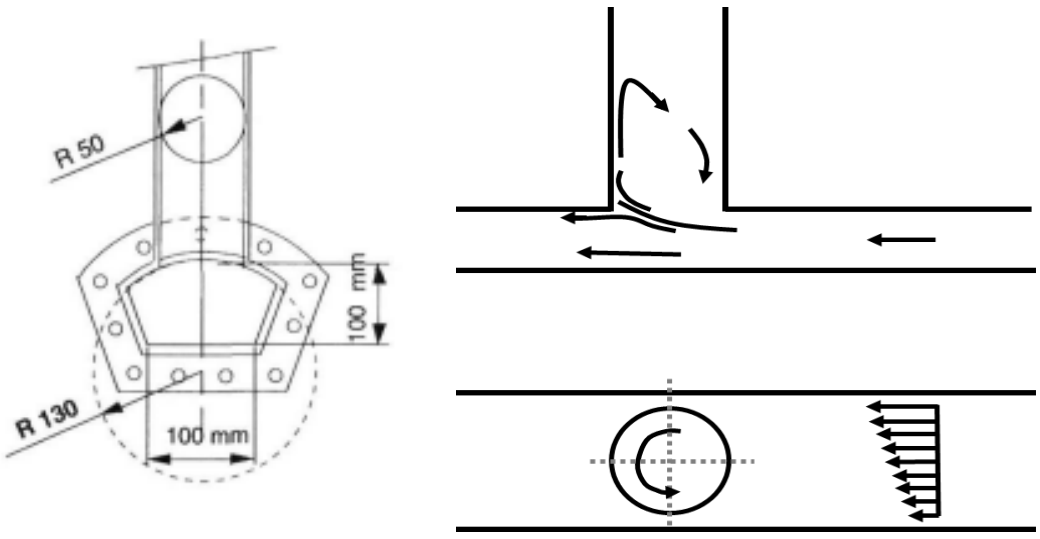

Figure 1-3 LEFT: Cross-section of main line flow channel of experimental test section. Flow characteristics observed by [13] (recreated)- TOP RIGHT: Flow shedding from main line, swirl developed about the y-axis in the branch line. BOTTOM RIGHT: Flow in branch line that swirls about the z-axis.

A follow up report in 1997 [14] tried to quantify the previously reported swirling in a branch line sufficiently to inform computational fluid dynamic (CFD) models for predicting the phenomenon analytically. Coarse particle image velocimetry (PIV) measurements (Figure 1-5) were used on a more qualitative level when comparing flow field trends with the results of a second moment closure (SMC) model and those of a k-epsilon model (Figure 1-4 [14] [15]). The SMC model was in better agreement with experimental data, but the results overall highlighted a great deficiency in the current resolution of data, which could not sufficiently inform computational methods (Figure 1-4, Figure 1-6).

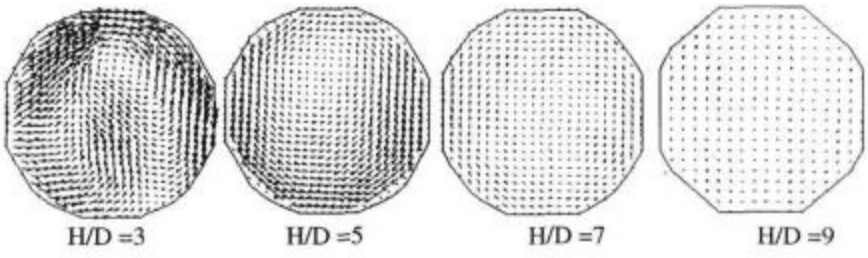

Figure 1-5 Extent of the PIV data shared from the report, which was used to illustrate the flow swirl direction and magnitude as a factor of diameters from the main line (H/D values).

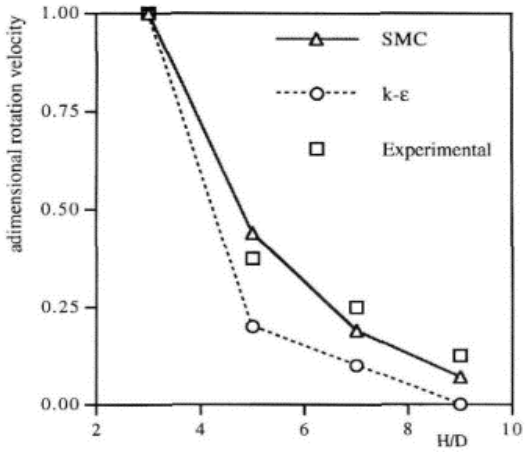

Figure 1-4 CFD modeling results compared to coarse experimental PIV data. [14]

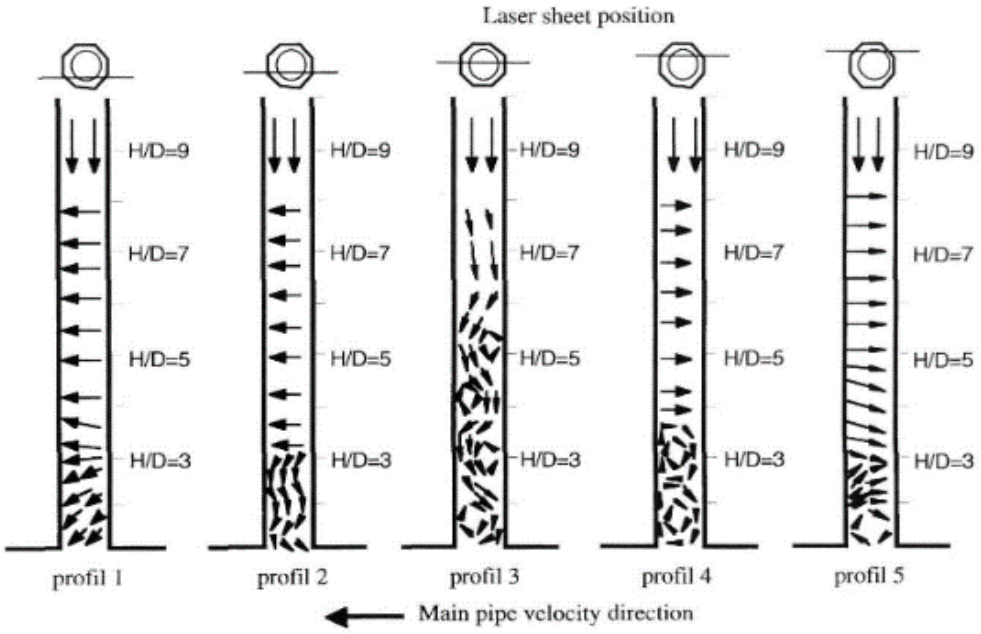

Figure 1-6 Sketched representation of visual observation of branch line flow in different planes. [14]

A similar interest in branch line TF research had been set off in the U.S. when the Nuclear Regulatory Commission issued a bulletin on the Farley-2 through wall crack incident in 1988, deeming such events as significant safety concerns [16]. In response, EPRI, the Electrical Power Research Institute (EPRI), assembled a program called TASCS to specifically address thermal stratification, cycling, and striping. The results of the principal studies [17, 18] in this initial period contradicted the theory that there was a dominant flow structure in the branch line that induced TF onset. The report claimed rather that the turbulence that penetrated the branch line came in bursts that disturbed the otherwise unrelated laminar flow. This assessment was made based on visual observations in the clear branch line and was corroborated with quantitative findings using hot-wire anemometer probes.

This report's studies using hot-wire anemometers and thermocouples yielded insight into the potential flow structures of interest within the branch line. Probes placed at various depths, aimed at measuring the tangential velocity along the branch-line axis, as well as the axial velocity, detected an exponential decay of the velocity, characterizing the swirl penetration depth within the branch line (Figure 1-7). The decay of the axial velocity along the center line of the branch line was less conclusive across tests, an example case is shown on the right of Figure 1-7. Comparing the velocities measured for the two components, it does

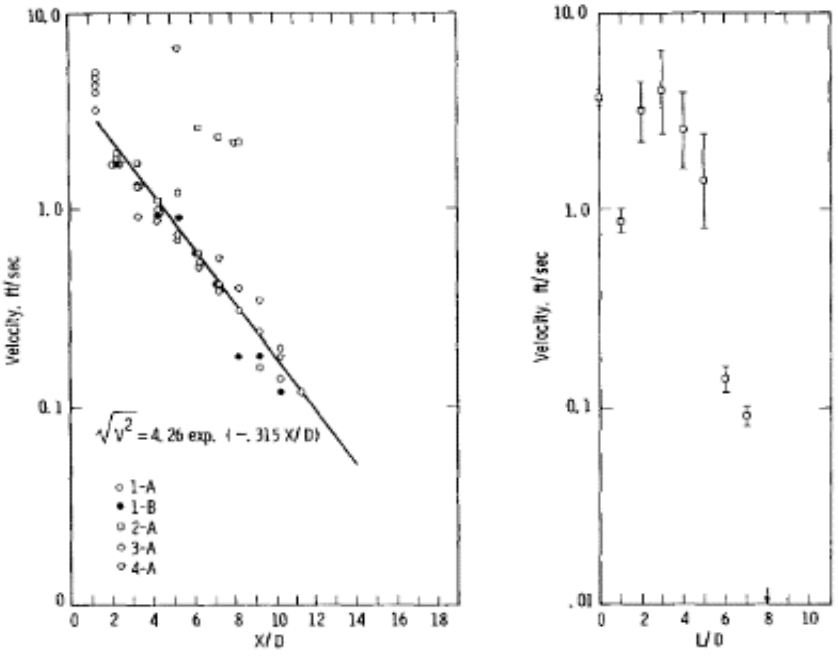

Figure 1-7 LEFT: Maximum tangential velocities at given depths in the branch line for multiple tests. RIGHT: Maximum axial velocities at given depths in the branch line. [17]

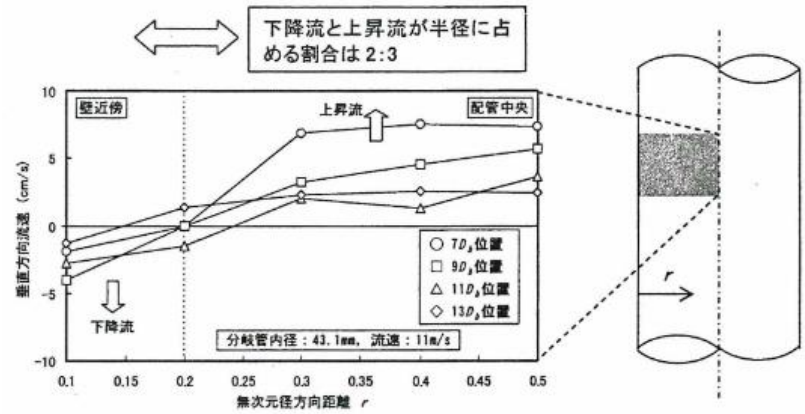

Figure 1-8 Measurements of axial velocities in the branch line at different radial positions. The axial flow is similar in direction and magnitude at equal distances from the center line across the pipe. [19]

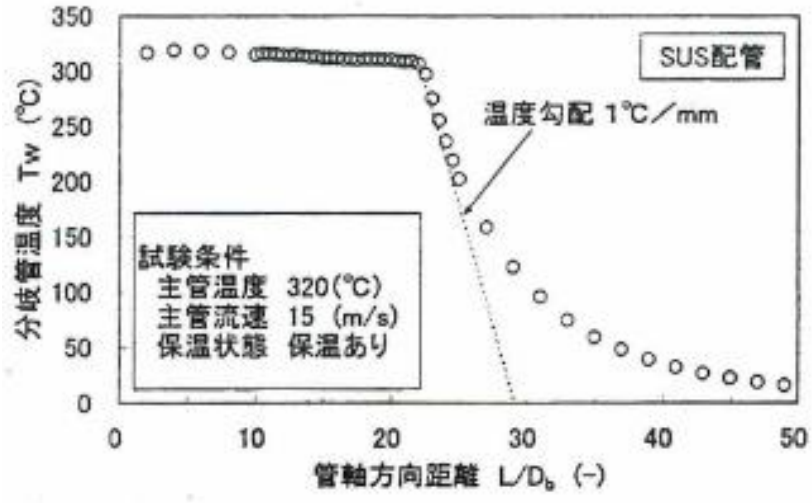

Figure 1-8 LDV measurements of Uθ, the rotational component, and Uz, the axial component, of the flow in the branch line at the same axial locations. [19]

appear that the primary transport of hot fluid from the main line to the thermal boundary in the branch line is done through the swirling that is present.

By 2003 the Japan Society of Engineers (JSME) released a lengthy analysis of branch line TF studies that were conducted at NPP temperatures in *Guideline for Evaluation of High-Cycle Thermal Fatigue of a Pipe* [19]. Findings supported the French report's claim of a persistent flow structure in the branch line and they were able to quantify the axial flow profile from 7-13 D_b (branch line diameters). Measurements showed that the corkscrew nature of the penetration is vortex-like, where the outer flow spirals away from the main line and the central flow is drawn back to the junction (Figure 1-). Temperature penetration data was also significant as it showed that the 300+^{o} C main line fluid (passing at 15 m/s) was penetrating to lengths of 22 D_b. At this boundary, the temperature of the branch line fluid drops sharply, initially at 1^{o} C/mm (Figure 1-8).

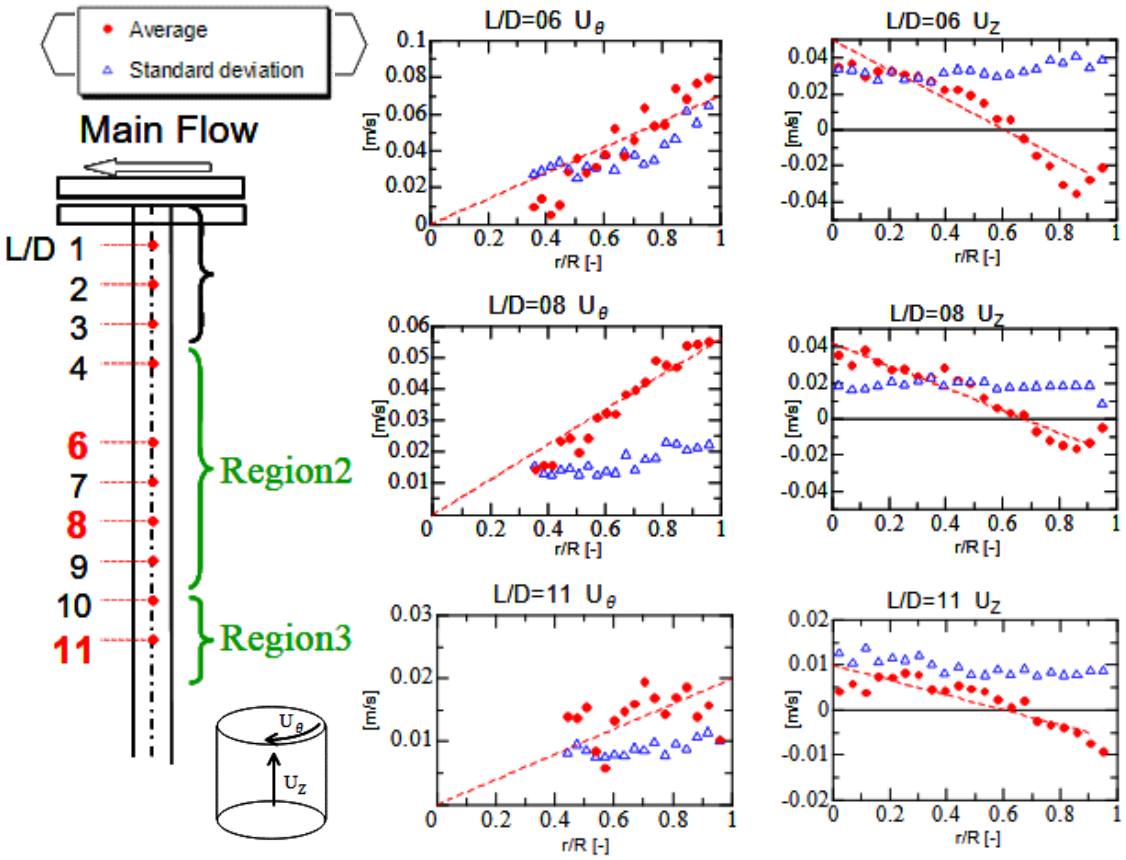

Figure 1-9 LDV measurements of Uθ, the rotational component, and Uz, the axial component, of the flow in the branch line at the same axial locations. [20]

Using an experimental loop with a rectangular cross-section for the main line channel to reduce the necessary working volumetric flow rate, researchers in Japan were able to further support the JSME findings of the branch line's flow profile, adding measurements of the rotational component [20]. Through laser Doppler velocimetry (LDV) measurements it was possible to determine that even in the turbulent region near the junction, where the eye cannot distinguish a dominant pattern, the flow structure of the corkscrew is still present. Utilizing two thermocouples one diameter apart along the branch line (11 and 12 D) thermal measurements also provided insight into the possible fluctuation frequency of the temperature at the penetration boundary in the branch line.

Utilizing the same experimental set-up with a rectangular cross-section for the main line, researchers later worked to define a correlation between main line flow conditions and the depth of the swirl penetration boundary in the branch line [21]. Some of these studies were done with a 50° C temperature difference between the main and branch lines which were sufficient to show that buoyancy forces dampened the ultimate penetration depth, compared to what would be observed in uniform temperature cases. By varying the main line flow rate (4-15 m/s) and the diameter of the branch line (8-43 mm), they were able to demonstrate a strong correlation between the main line flow rate, the branch line diameter, and the swirl penetration depth (Figure 1-10). This required calculating the Reynolds number using the main line velocity and the branch line's diameter for comparison with the observed penetration depths. The extent of penetration was visually assessed by researchers observing where the flow of tracer particles stagnated.

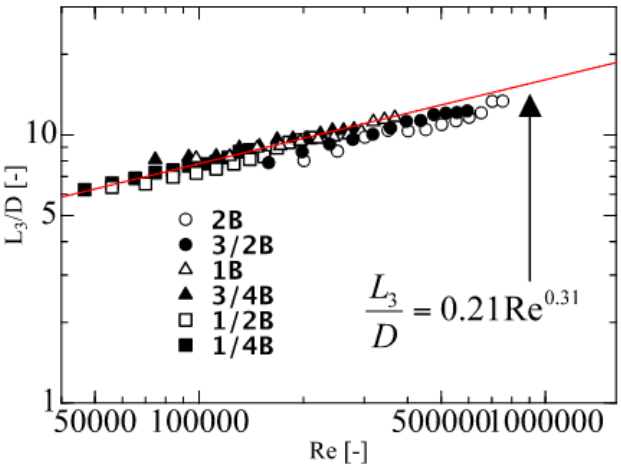

Figure 1-10 Relationship between Branch pipe Reynolds number and normalized penetration depth. [21]

The same tracer particle technique was employed with video cameras

	Pattern 1	Pattern 2	Pattern 3
	Streamlines parallel to the cross-sectional direction	Streamlines consisting of small vortexes	Streamlines of large swirl flow
$L_a=2D_b$			
$L_a=3D_b$	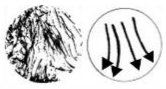		
$L_a=4D_b$			
$L_a=5D_b$		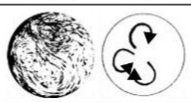	

Figure 1-11 Streamlines observed in cross-sections of the branch line at various axial locations. [22]

to determine flow characteristics in the branch line cross-sections at different axial positions [22]. The stream lines from the cross-section observations were classified into three dominant catergories (Figure 1-11). The catergories highlighted the main difference between the upper ($L/D < 3$) and lower ($L/D > 3$) sections of the branch line even though they both experienced barrages of smaller vortices. The presence of the primary axial swirl that approaches the penetration boundary was confirmed.

At the outset of this dissertation's work, references [20, 21, 22]comprised the most comprehensive, publicly available analysis of dead-ended branch line flow phenomena. Although reference [20] only presented flow components for portions of the branch line at various axial locations, the quantification of the flow swirl in the branch (Figure 1-9) provided a flow direction and magnitude touchstone for initial LDV and PIV measurments in the UM facilities. Correlations based on qualitative assessment, like that presented in Figure 1-10 for the penetration boundary, informed initial measurement regions of interest axially in test facility branch lines.

1.3 Background on Penetration Boundary Prediction Methods

Computational predictive methods for determining the penetration depth of a flow swirl into a branch line and the establishment of a thermal boundary range from simple correlations to complex multi-physics analysis like CFD. The effectiveness of any method is dependent upon the resolution of experimental data that informs its development. Preferably, data gathered would be used to inform computationally inexpensive low-order methods such as basic correlations and more expensive CFD predictive methods.

Straightforward calculations for predicting TF onset locations are computationally inexpensive and therefore the most accessible to engineers and designers. To advise such calculations in the case of TF in branch lines, this has required the development of correlations

between flow conditions, piping geometries, and the resulting penetration boundary through experimental work. As mentioned in the previous section, researchers have been able to identify certain key relationships (i.e. main line Re vs. penetration depth) that make this prediction method valid, but it is limited in scope. The correlation they presented, for example, is valid only for a straight-vertical branch line departing from a main line with a fully developed turbulent flow. To expand the relevance of these correlations, experiments must be conducted with different piping geometries and various flow conditions to demonstrate their general validity.

EPRI is one of the entities that have invested considerable research efforts to expand the body of valid correlations by conducting experiments on various geometries and introducing thermal gradients (MRP-97). Key geometries they have worked to determine the penetration length in are the down-horizontal (DH) and up-horizontal (UH) configurations, as bends in branch lines are common and quite susceptible to TF risk. To extend the applicability of correlations beyond the straight down vertical case, EPRI's current scheme applies additional factors such as the location of the bend, the length of the vertical section preceding it, buoyancy effects, and cold fluid in-leakage. The models they have developed are more complex than those proposed by references [21] [22] but they still have limitations. When the correlation calculations are made to compare with plant data, some cases agree well yet others show that EPRI model predictions of penetration depth are off by more than three branch line diameters (MRP-251, Table 6-10). There is reason to believe that the ineffectiveness of the models in such a case is due to factors that are not accounted for in the correlations, such as the branch line junction's proximity to an upstream main line elbow or the pump, which varies the main line flow conditions. This would mean that to increase the accuracy and applicability of the established correlations, more experimental work would have to be done.

At the most complex end of predictive methods, computational models have been constructed that incorporate turbulent decay, heat transfer, and finite element analysis. These models are computationally more expensive but can more easily address changes in geometries, main line flow conditions, branch line leakage, and thermal variations. This can reduce the amount of experimental work necessary to account for specific cases in NPP design processes, however, the principal physics must be properly applied to yield accurate results.

With each CFD model verification campaign, the inevitable discussion of computational cost vs result accuracy ensues: Is it necessary to use more computationally intensive models such as Large Eddy Simulation (LES) or are Reynolds-averaged Navier-Stokes (RANS) equation models sufficiently accurate? For industrial applications, it is advantageous to use the lowest cost option possible in the sense of economics, but one must be mindful of each model's limitations [23]. For example, researchers have compared the branch line penetration flow to results from LES models that capture the data's temperature fluctuations well [24] (Figure 1-12). Similar modeling of the flow has been achieved using RANS models, but given the time-average foundations of these models, fluctuation information are not provided [25].

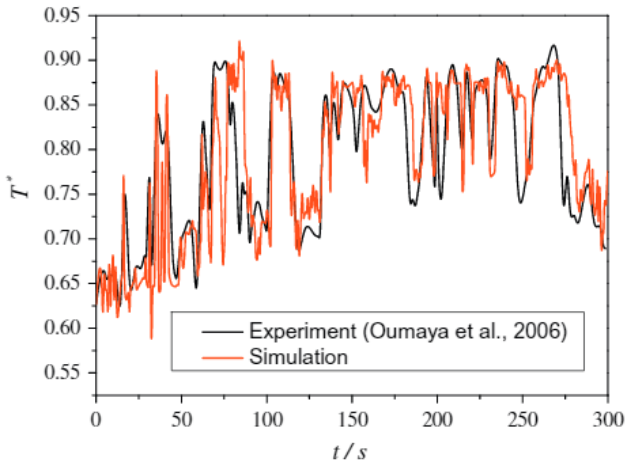

Figure 1-12 Experimental results vs LES model simulation results of thermal fluctuations at a given point in a branch line. [23]

Accurate prediction of the penetration boundary location is the most pressing shortcoming of current methods. For this reason, it is desirable to have sufficient data to validate computationally less expensive CFD models like RANS, and then use the validated models to

support the screening of NPPs branch lines that might be susceptible to TF. The main goal of the present dissertation is therefore to establish an experimental database of higher resolution data of the branch line flow at the penetration boundary with well-defined boundary conditions, so that it will be possible to identify the appropriate turbulence parameters for RANS models to be validated.

1.4 Summary

The available body of experimental work has led to significant insight into the flow conditions surrounding TF in reactor branch lines but remains too coarse to reliably inform predictive models. Measurement campaigns have led to the identification of distinct flow regions in the branch line and the formulation of penetration length correlations. These measurements lack the resolution to adequately inform CFD modeling because they are the result of sparsely placed sensors or low-density, pointwise LDV measurements. Campaigns have also overlooked the significance of main line flow condition variations upstream of the branch line on the resulting penetration depth. Validating CFD models to appropriately predict branch line flow conditions will require higher resolution data, preferably velocity field data, that accounts for variations in main line flow conditions as well.

Chapter 2 Methods and Experimental Facilities

2.1 Overview

Measurements for this dissertation were designed to gather CFD-grade, high-resolution data of flow phenomena in isolated branch lines with minimal to no obstruction of the penetrating flow. The high-resolution, non-obstructive measurement techniques used were:

- Laser Doppler velocimetry
- Particle image velocimetry.

These measurement techniques were applied to the optically clear test sections of four different measurement facilities:

- The Reactor Branch Line – Thermal Fatigue (ReBL-TF) facility,
- the Rectangular Profile Loop (RPL),
- the High-Capacity Loop (HCL),
- and the Swirl Separate Effect Facility (SSEF).

Although these facilities (Table 2-1) will be discussed individually in detail in Section 2.3, it is important to understand their relationship to one another and how they contributed to the overall goals of this dissertation.

After identifying the lack of high-resolution data available for validating CFD models related to isolated branch line flow, the Reactor Branch Line – Thermal Fatigue (ReBL-TF) facility was constructed. The ReBL-TF facility was built with a branch line ID common to ECCS piping and a main line ID that was scaled down from a typical NPP size as informed by CFD analysis. Initial measurements using this experimental loop served as a proof of concept to secure further funding for upsizing the pump or altering the facility to achieve typical NPP main line flow velocities.

Table 2-1 Experimental facility relevant geometries and dimensions

Facility	Main Line Geometry	Main Line Hydraulic Diameter (mm)	Branch Line ID (mm)
ReBL-TF	Round	101.6	50.8
RPL	Rectangular, 100mm x 15 mm	26.1	50.8
SSEF	Round	N/A	44.45
HCL	Round	101.6	50.8

Funding for the Rectangular Profile Loop (RPL) and the High-Capacity Loop (HCL) was obtained through a partnership with the Electrical Power Research Institute (EPRI). The RPL facility provided a way to validate previous measurements made by other researchers (references [20, 21, 22]) that employed a rectangular main line flow channel. With a reduced main line hydraulic diameter (26.1 mm), the RPL facility was able to utilize the pump from the ReBL-TF facility to achieve flow velocities more than three times that of the ReBL-TF facility. The HCL was constructed using the same main line and branch line diameters as the ReBL-TF facility, but with a significantly more powerful pump. With the use of this pump, the HCL was able to achieve NPP level main line flow rates (9-14 m/s).

As experiments were being conducted in the RPL, it became apparent that an experimental facility that could eliminate the need for a main line flow driving the swirl in the branch line would be of value. Instead of a main line flow penetrating and driving a flow swirl in the isolated branch

line, the Swirl Separate Effect Facility (SSEF) branch line flow was driven by a stirring paddle. The SSEF design greatly reduced the fluid demand of the system and the complexity of its operation. The experimental data of the SSEF were to be compared to the data of the RPL and HCL experiments to validate the exclusive use of an SSEF-like facility for further branch line flow penetration studies.

2.2 Measurement Techniques

Laser Doppler velocimetry (LDV) and particle image velocimetry (PIV) are commonly used high-resolution, nonintrusive measurement techniques. LDV is utilized for pointwise velocity measurements and PIV captures velocity fields. The fields of PIV measurements can contain 2D vector information, or 3D velocity fields in the case of stereographic PIV (S-PIV) and tomographic PIV (T-PIV). Both measurement methods require optical access to the flow, as they rely upon the transmission of light. As a result, the facilities discussed in Section 2.3 were designed with optically clear piping about the regions of interest.

2.2.1 Laser Doppler Velocimetry

Laser Doppler velocimetry (LDV) utilizes the fringe effect of intersecting laser beams and the Doppler principle to measure the velocity of a passing particle. Collimated laser beams emitted for LDV application are intentionally crossed at a specific location to create an interference region [26]. The fringe pattern created in this region exhibits distinct, lit and unlit intervals (Figure 2-1). As a particle in the flow passes through this region, it scatters light in each lit portion, which is detected by an optical sensor. The frequency of scattered light

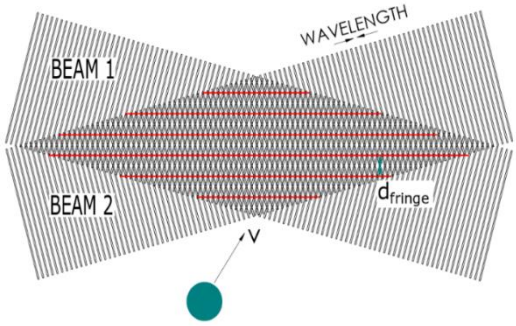

Figure 2-1 Representation of the fringe pattern (red lines) created by two intersecting beams of light.

arriving at the detector is interpreted as velocity data using the Doppler principle [27]. Because the measurement region for a typical setup is 10^{-6} mm^3 to 10^{-4} mm^3 in size, the velocity data gathered is considered pointwise.

A pair of beams used for LDV can only measure a single velocity component of a passing particle. The component of the velocity that is captured is the one that is perpendicular to the fringe pattern. Determining which component is being captured (i.e., Vx, Vy, Vz) is relative to the measurement being conducted and the user's alignment of the beams. For example, if the x-component (Vx) is desired from the flow, the beams' origins from the transmitter would be aligned along the same line parallel to the x-axis. Positioning the origins of the beams on a corresponding perpendicular line would orient the LDV to capture Vy in this hypothetical situation. Discriminating whether the particle is moving in the positive or negative direction is accomplished by a fixed frequency disparity between the beams.

The LDV setup used for this work was an Artium LDV-200TRX, which is a transceiver unit. Velocity measurement accuracy of this LDV device is ±0.1% of reading. Particles used in the fluid for LDV detection were neutrally buoyant, 10-micron glass spheres. LDV measurements were used to verify PIV measurements, capture main line flow profiles, and track the decay of a flow swirl in the branch line. To achieve these objectives, the LDV unit was mounted to a linear translation stage that allowed it to be moved precisely along two axes.

2.2.2 Particle Image Velocimetry

Particle image velocimetry (PIV) is an established optical method used to measure instantaneous fluid movement in a non-intrusive manner. PIV measurement relies upon particle seeding in the flow, illumination of the plane of interest, and high-speed imaging (Figure 2-2). Specialized algorithms are used to translate image pairs into vector data for the flow field captured.

The technique has gained popularity over the past four decades as the availability and abilities of high-speed cameras have improved [28].

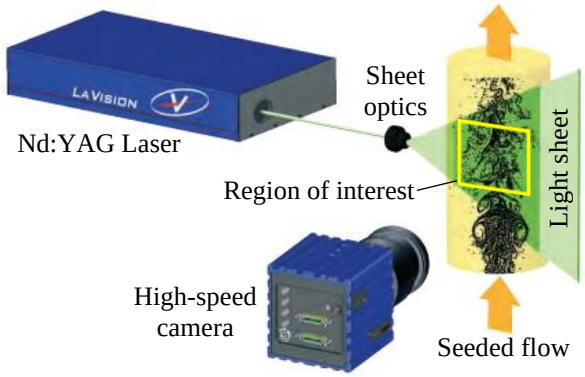

Figure 2-2 Representation of 2D PIV measurement setup, adapted from [39].

Fluids that are compatible with PIV measurement techniques transmit light easily and require the addition of opaque seeding to facilitate imaging. For liquids, seeding is usually done with specialized microspheres that are designed to match the fluid's density. These microspheres are shaped and sized to reduce any effect they may have on the local flow. Determining the appropriate size of a particle for PIV applications is done using the Stokes number. This dimensionless number characterizes the behavior of a particle suspended in a fluid flow based on particle properties, flow obstruction dimensions, and fluid flow rates. For the PIV measurements related to this work, the particles were 10-micron, hollow glass spheres.

For standard 2D PIV measurements, particles in the flow's cross-section of interest are illuminated using a thin light sheet. Generating this light sheet is usually done with a laser and the appropriate optical lenses. The light source needs to be strong enough to provide a high contrast between the lit and unlit regions of the flow. This contrast facilitates images with less out of plane particles captured, yielding a better signal-to-noise ratio. It is important to limit the noise of the images, as it has a direct impact on the accuracy of the measurements being made. To achieve measurements where the moment-to-moment evolution of a flow is captured, the light sheet must either be a continuous source or capable of rapid firing. For the PIV measurements related to this work, a dual cavity Nd:YAG laser (532 nm) with appropriate sheet optics was used.

Imaging particle movement for PIV measurements relies heavily upon the capacity of high-speed cameras. The acquisition rate and storage capacity of cameras dictate how high of a flow rate can be measured and for what period. High-speed image acquisition allows the time step (Δt) between captured images to be small. When the Δt is sufficiently small, the particle's physical displacement between images (Δx, Δy) is on the order of <4 pixels. Such low Δx/y values allow algorithms to track the movement of particles image-to-image with high accuracy. Although a short Δt provides a means of capturing time resolved flow data, limited camera memory means that it also decreases the acquisition period per measurement. For the 2D PIV measurements related to this work, a Phantom Miro 341 was used. It could capture 12 GB of full frame images (2560 x 1600 pixels) at maximum rate of 800 frames per second.

Translating a series of particle images into flow data relies upon specific computational tools. For this work, these tools were accessed through LaVision's Davis software. The algorithms in the software utilize corresponding Δt and Δx/y information of image pairs to create vector fields for that moment. The Δt is determined from camera settings used in capturing the images while the Δx/y information is derived from calibration images.

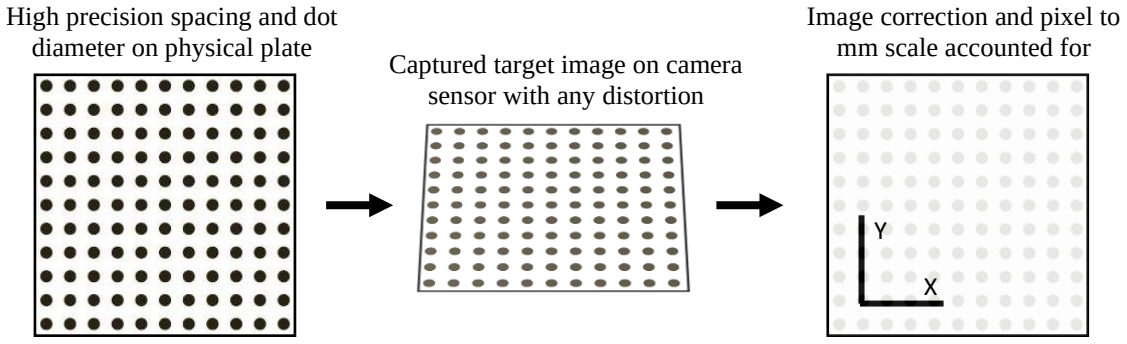

Figure 2-3 Representation of calibration target for measurements, used to account for any captured distortion and to correlate pixel values to linear space values.

Calibration images are made by imaging a calibration plate in the measurement plane and correlating the physical space captured to the pixel space of the camera's sensor (Figure 2-3). Thus, pixel displacement in an image can be identified as linear displacement in physical space. Calibration plates also provide a way to account for camera lens distortions or refraction caused by imaging through various media. Figure 2-4 shows a target with uniform dot spacing that was imaged through the curved wall of glass piping. Near the center of the pipe, there is less refractive change between the real item and the captured image than towards the edges. This is more noticeable by eye when the photo is enlarged, and a reference square is used (red square is the same size in both locations). Where the camera's line of sight passes through more glass (towards edges of the image), the refraction of the piping appears to compress the dots towards the center. Algorithms correct this refractive shift or distortion perceived by the camera using the high-precision calibration plate dot sizing and spacing information and corresponding images.

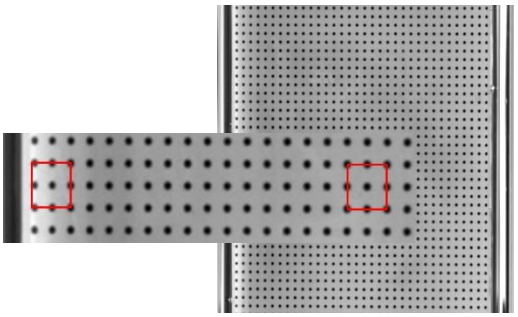

Figure 2-4 Calibration plate raw image. Square imposed as visual reference is the same size in both locations. The glass pipe surrounding the target appears to have caused a radial distortion of the true image that is greater where the thickness of the glass through the line of sight of the camera is greater.

When imaging through curved surfaces such as piping, one of the measures employed to reduce refraction related issues is the use of an optical box. The flat sided box, usually constructed of glass or clear acrylic, is filled a refractive index matching fluid. The refractive index matching fluid effectively disappears the piping boundaries as seen in Figure 2-5. This application has the added benefit of controlling the presence of reflections on the surface being imaged through. For

all PIV related imaging in this study, optical boxes filled with vegetable glycerin (n=1.47) surrounded the piping in the measurement region.

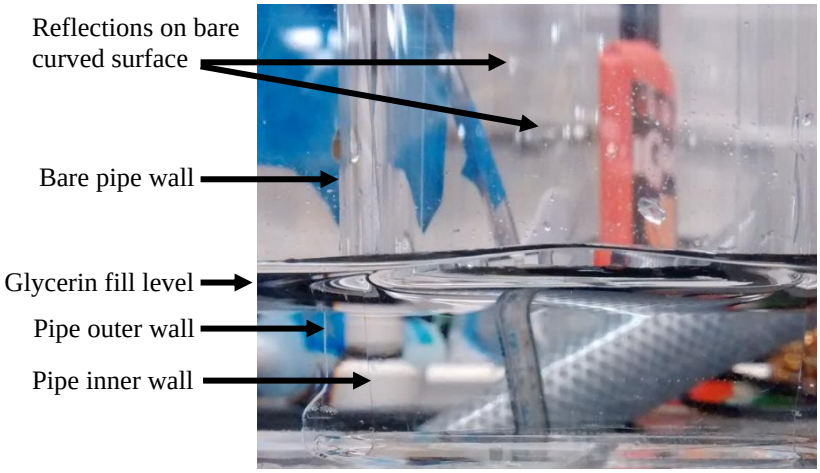

Figure 2-5 The effect of using a refractive index matching optical box when imaging through a curved surface.

The velocity vector fields that algorithms derive from image pairs are as coarse as the interrogation windows that subdivide them. From a resolution standpoint, ideal velocity vector fields would contain a vector per particle being displaced. However, this is impractical in terms of the computational resources such a process would demand and the relevance of such a field's application. As a compromise, the measurement field is divided up into interrogation windows, each of which yields a single vector. Within each window, the displacement of particles between frames is cross correlated to determine the mean displacement. Along with the Δt, this

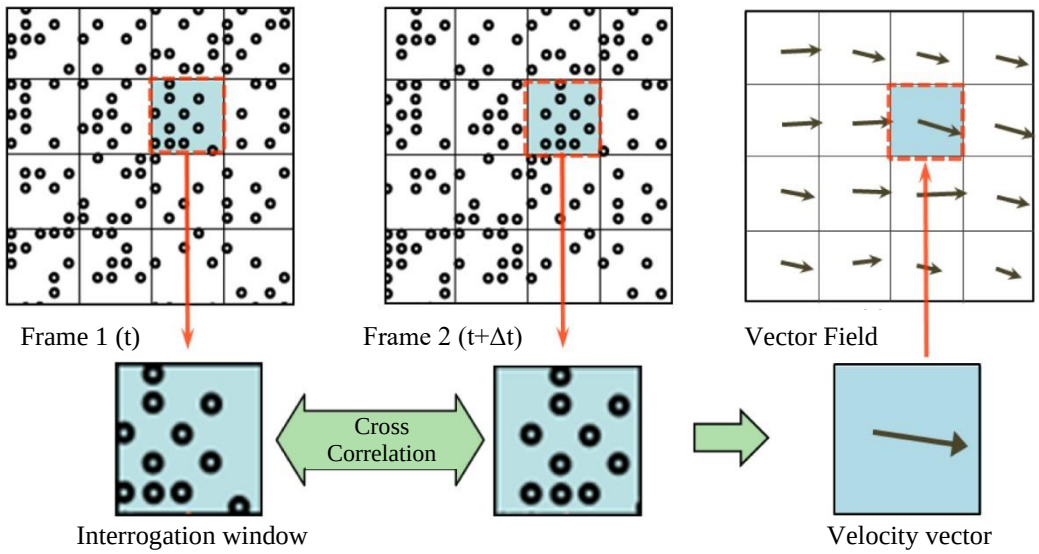

Figure 2-6 Particle displacement per interrogation window calculated to corresponding velocity vector.

mean displacement determines the magnitude and direction of the velocity vector in each window (Figure 2-6). Using multi-pass and interrogation window size reduction stepping techniques can greatly reduce the uncertainty of the resultant vectors and improve the resolution. For further discussion of these techniques or the working principles involved, refer to references [29] [30].

A typical PIV measurement for this work was conducted as follows:

- The measurement plane and region of interest in the flow volume were selected.
- A calibration target was aligned in the selected plane in the region of interest.
- The volume was filled with water, as the calibration images need to account for the refraction of the working fluid.
- The laser sheet was aligned so that it occupied the selected plane in the region of interest.
- A camera was positioned orthogonal to the selected plane so that it could image the region of interest.
- Camera focus was adjusted to the selected plane.
- Calibration plate images were captured by the camera.
- The calibration plate was removed from the volume.
- The water was seeded.
- Flow through the system was initiated.
- Simultaneously firing the laser and triggering the camera, the imaging rate (Δt) was adjusted to flow conditions for appropriate $\Delta x/y$ values.
- Images of the illuminated particles were captured.
- Measurement images were processed in Davis to yield vector data for analysis.

2.2.3 Tomographic Particle Image Velocimetry

Tomographic Particle Image Velocimetry (T-PIV) is an advanced PIV application that builds upon basic PIV principles to capture 3D velocity field data. For a review of the PIV technique, refer to Section 2.2.2. Methods for T-PIV measurement deviate from typical PIV methods in two major ways: the light source illuminating the seeding particles is volumetric, having a greater depth than the typical thin plane, and multiple cameras are used to resolve the 3D movement captured. Both features add complexity to the measurement process, but T-PIV data provides 3D component information that is critical to understanding anisotropic, non-homogeneous flows.

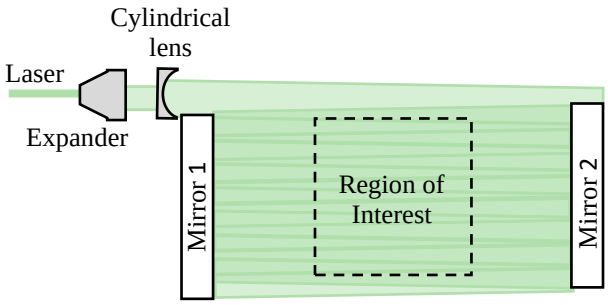

Figure 2-7 Representation of a multi-pass laser light amplification setup used to illuminate the region of interest.

Volumetric illumination for T-PIV measurement can be achieved using high-efficiency LED lighting banks or high-powered lasers with the appropriate optics. At its simplest, the laser illumination method employs a beam expander and concave lens to fill the volume with sufficient light. However, spreading the energy of the beam over a large volume may require additional treatments to reach a desired energy deposition in the region of interest. One approach to create the illuminated volume is using a mirror arrangement to pass the light multiple times to amplify the light present or to completely fill a large region of interest (Figure 2-7). Illumination using LED arrays for large volumes is typically less complicated because they are designed to

Figure 2-8 LaVision LED Flashlight 300, 72 white emitting diode array.

emit powerful light from a large area. The bulk lighting emitted from an array is trimmed to the desired height and width of the measurement volume via a knife-edge filter (essentially a rectangular slit in a thin panel). Because light is still divergent after passing through the filter, it is best practice to place the filter as close to the region of interest as possible. In the case of this study, the LaVision LED-Flashlight 300 was used, and the knife-edge filter was placed nearly touching the involved piping (Figure 2-8).

Volumetric illumination of the region of interest presents two primary problems for the T-PIV measurement process that must be overcome. First, the contrast between the illuminated particles and ambient light in an image can be quite low, which translates to images with low signal to noise ratios. To improve image contrast, the flow in this study was seeded with fluorescent particles that emit at a wavelength 550 nm when illuminated. Using spectral lens filters, the cameras were able to image these particles while much of the ambient light was prevented from reaching the sensors. Second, volumetric lighting can increase refraction issues, especially when interacting with curved surfaces like in this study. Issues of refraction were greatly reduced by encasing the round pipe in rectangular prism filled with a refractive index matching solution. For application with the borosilicate piping, the solution used was vegetable glycerin (n=1.47).

Translating T-PIV measurements of 3D physical space into image space with 3D information relies heavily on accurate image capture through multiple high-speed cameras [31]. Cameras must be aligned and focused for their individual image capturing as well as having their imaging planes mutually aligned in the physical space. While the imaging planes must overlap in the region of interest for all cameras, it is important to note that each camera must be oriented on its own viewing axis. To meet these two requirements, cameras are typically oriented in a cross or

linear formation as shown in Figure 2-9. Orientations where a pair of cameras is positioned on the opposite side of the region of interest is also possible when using a double-sided calibration plate.

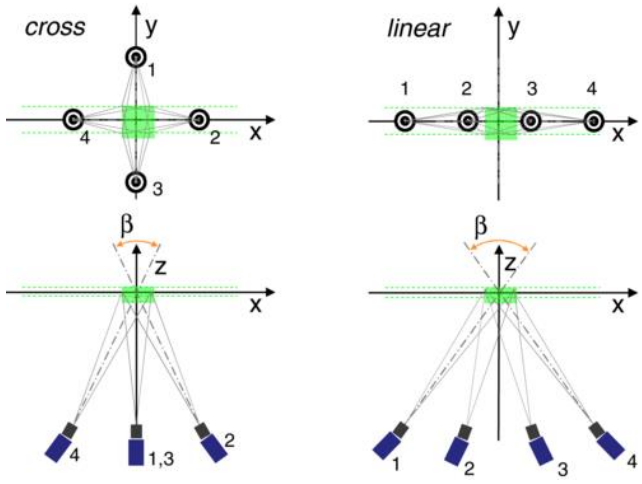

Figure 2-9 Common camera orientations used for T-PIV measurements. Borrowed from [32]

The alignment and focus of each camera requires attention to the viewing axis of the lens, the lens aperture, and the orientation of the camera's imaging sensor relative to the focal plane. In T-PIV applications, the position of each individual camera in relation to the other cameras in use is important. No lens axis should be collinear with another, and when possible, the bisection of a lens pair viewing angle should be orthogonal to the focal plane. Both conditions are represented in Figure 2-9, where the viewing angle, β, is bisected along the z-axis [32]. The numerical aperture of each lens needs to be increased to the point that the focal depth matches the thickness of the measurement volume. Ultimately, this is how particles across the depth of the measurement volume will be clearly imaged. Adjusting the aperture is best done after the sensor, lens, and focal planes have been properly aligned. Proper alignment is achieved when all three planes intersect along what is known as the Scheimpflug line (Figure 2-10). This allows the full focal plane to be imaged clearly on the sensor after passing through the off-angle lens.

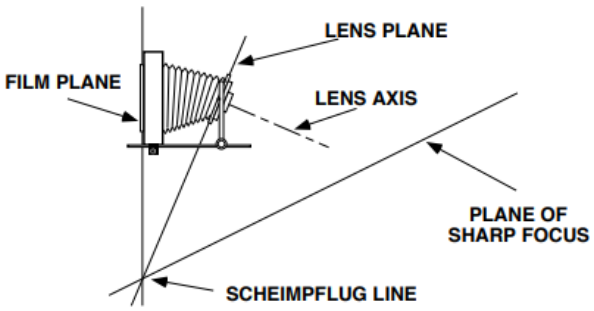

Figure 2-10 Demonstration of the Scheimpflug principle, orienting the focal plane, the lens plane, and the sensor plane appropriately. Borrowed from [40].

T-PIV measurements for this study employed two pairs of Phantom brand high-speed cameras. The first pair were Miro 341 units with 12 GB of memory installed. The second pair were 340-L units with 18 GB of installed memory. Both sets of cameras were capable of a full frame (2560 x 1600 pixels) imaging rate of 800 frames per second.

Figure 2-11 Double-sided 3D calibration target.

Interpreting T-PIV images of 3D physical space from multiple cameras to yield a coherent image space requires images to be co-calibrated. Calibration provides a way to account for lens distortion and any refraction caused by imaging through various media. In the case of 3D measurements, a 3D calibration plate like that of Figure 2-11 is used to additionally account for image depth. The depth of the plate or distance between its two dotted planes is generally less than the thickness of the measurement volume. Before imaging, the calibration plate is oriented in the measurement volume with one of its faces co-planer with the focal plane in the region of interest. At this point, each camera simultaneously captures an image of the plate. These images are brought together in specialized software to form a combined calibration that will inform each particle image taken thereafter.

To obtain the level of precision necessary for tomographic image reconstruction, additional digital corrections must be applied to the initial image calibration. This is known as volumetric self-calibration (VSC). Part of what the process yields is a disparity map between the real-world space and the reconstructed image space. This can help to overcome inaccuracies in the measurement setup related to calibration plate placement, lens optical issues, and possible camera sagging due to mechanical vibration or poor mount stability. Ultimately, the goal is to reduce the calibration error across the whole measurement volume to less than 0.1 pixel.

To conduct VSC, a set of particle images from the measurement are passed through series of calibration mapping functions. First, VSC calculates the shift of particles in 2D space. Second, this particle shift is correlated to possible 3D positions of the particles in the volume. The possible 3D positions that the algorithms will consider per particle are determined by the size of the maximum allowed triangulation error [33]. This error value, which can be approximated through an iterative VSC process, is a user input that should exceed the expected calibration error.

The degree of triangulation error that is present in the measurement set is proportional to the additional error caused by the appearance of ghost particles. Ghost particles are spurious light intensity peaks that appear as 3D image space is reconstructed from the triangulation of particles between sets of 2D image pairs. Ghost particles appear randomly distributed, which contrasts the distinct disparity peaks that the correlation mapping produces for the real particles. This means that as measurement images are processed and ghost particles appear, the VSC information from the calibration process can greatly discriminate spurious particles in each sub volume of the measurement. For further discussion on ghost particles see [34].

A typical T-PIV measurement for this work was conducted as follows:

- The measurement volume and region of interest in the flow were selected.
- A calibration plate was aligned with a face in the central focal plane of the region of interest.
- The volume was filled with water, as the calibration images need to account for the refraction of the working fluid.
- The volumetric light source was aligned with the knife-edge filter to fill the selected volume in the region of interest with light.

- A camera array was arranged in a linear formation with camera pair viewing angles between 30^o – 60^o.
- The camera array was appropriately distanced from the focal plane in the region of interest. Fine tuning the array's position was done using a linear translation stage.
- Camera angles were adjusted using the Scheimpflug technique to capture the full region of interest clearly.
- Individual camera focus was adjusted to the selected plane.
- Calibration target images were captured by the cameras.
- The calibration target was removed from the volume.
- The water was seeded with fluorescent particles.
- Flow through the system was initiated.
- Simultaneously firing the LED light bank and triggering the camera, the imaging rate (Δt) was adjusted to flow conditions for appropriate $\Delta x/y$ values.
- Images of the illuminated particles were captured.
- Measurement images were processed in Davis to yield vector data for analysis.

2.2.4 Analysis Software

After acquisition, data was processed and analyzed using three primary tools, Microsoft Excel, LaVision's Davis software (8.3-10.1 editions), and MATLAB. Simple tabulations of LDV data were compiled in Excel and passed to MATLAB for frequency analysis. Both PIV and T-PIV data were collected using Davis software. Built in, tailored features specific to working with PIV data made Davis the favored choice for processing raw measurements. Some of these features include image calibration mapping, image filtering and sharpening, volume self-calibration, and

raw particle image processing to vector field results. Davis also has strengths in easily representing the data in various ways, as will be demonstrated in Sections 3-6 with scalar and vector field representations in both 2D and 3D results. Post processing analysis of PIV data was also conducted using MATLAB.

2.3 Experimental Facilities

Within the Experimental and Computational Multiphase-Flow Laboratory (ECMFL) at the University of Michigan, four facilities have been constructed to investigate branch line flow characteristics related to the onset of thermal fatigue in reactor emergency core coolant injection lines, namely:

- The Reactor Branch Line - Thermal Fatigue facility (ReBL-TF), was the first facility to be constructed, and was designed to utilize a low working-fluid volume, maintaining a round cross-section for the main line piping.
- The Rectangular Profile Loop (RPL), which was a modification of the ReBL-TF facility, in which a rectangular cross-section was used for the main pipe to reduce the demands on the working-fluid volume, while at the same time raising the maximum velocities in main line flow achievable with the same equipment.
- The Swirl Separate Effect Facility (SSEF) was constructed to investigate the decay of a flow swirl along the branch line axis with clean, well-defined boundary conditions, without the interference of other flow phenomena.
- The High-Capacity Loop (HCL), which shares geometric similarities with the ReBL-TF, was constructed to investigate branch line flow phenomena at nuclear power plant level main line flow rates.

2.3.1 Reactor Branch Line – Thermal Fatigue

The Reactor Branch Line – Thermal Fatigue (ReBL-TF) facility was designed to be a scaled down segment of a reactor coolant loop with a single, isolated branch line (Figure 2-12). Scaling a research apparatus is common and practical. In this case, reducing the main line diameter was done to decrease the necessary working-fluid volume, the physical space needed, and the electrical power required to drive the fluid. Only a single, alterable branch line junction was necessary for the planned investigations with this facility.

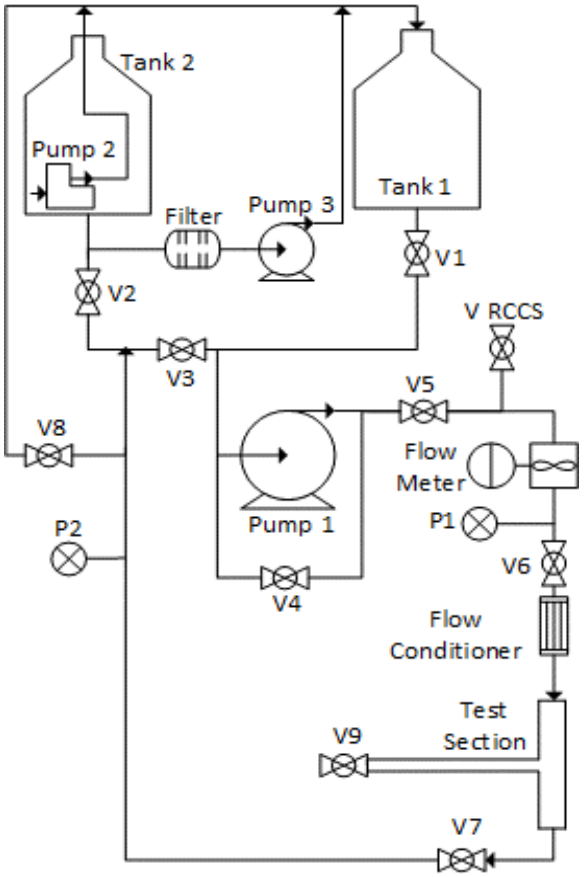

Figure 2-12 Schematic of ReBL-TF facility. Corresponding information about the components labeled can be found in Table 2-1.

The degree of scaling for the facility was determined using the results of pre-test computational fluid dynamics (CFD) simulations. The primary geometric feature investigated for size reduction was the main line of the loop due to its direct effect on the amount of fluid being driven in the system. A typical nuclear power plant (NPP) main coolant line diameter is 700 mm, which means a high volumetric flow rate is required to achieve typical main line flow velocities around 10 m/s. As a baseline, the first CFD simulation of the study used a geometry with a main line 700 mm in diameter that intersected with a perpendicular branch line 50.8 mm in diameter. Further simulations were run with the same branch line size and orientation, while reducing the size of the main line diameter per run.

CFD results showed that reducing the main line from 700 mm to 100 mm did not greatly alter the resultant flow profiles near the branch line opening. This was not so for cases where the main line diameter was less than 100 mm. Figures 2-13 – 15 demonstrate the similarity between the 700 mm case and that of the 101.6 mm case (101.6 mm corresponds with the inner diameter of readily available 4 in. piping, which was in turn selected as a primary construction material). Figure 2-13 contains comparisons between the velocity and turbulent kinetic energy present in three cross-sectional planes near the junction of the branch line. Figure 2-14 and Figure 2-15 illustrate the velocity magnitude and turbulent kinetic energy along lines in those same planes. Some disagreement between the 700 mm and 101.6 mm plots is expected (and was present in the other intermediate simulation cases as well) as

Table 2-2 Schematic labels from Figure 2-12.

ReBL-TF Schematic Component List

Component Label	Description
Filter	Model: SF90110T, Intex Clear Sand Filter for clarifying water being reused.
Flow Conditioner	Honeycomb of 3 mm channels to accelerate flow straightening.
Flow Meter	Model: TM400, GPI turbine flow meter, accuracy 3% of reading.
Pump 1	Model: E2.5J7A-CC, Patterson pump, capable of 1,135 LPM at efficiency. Coupled to 7.5 kW WEG motor and controlled by ABB ACH550 variable frequency drive
Pump 2	Drummond 0.19 kW submersible pump for tank to tank transfer, capacity 189 LPM
Pump 3	Intex filter component, capable of 66 LPM flow rate
P1	Direct readout pressure gauge
P2	Direct readout pressure gauge
Tank 1	Loop supply water tank
Tank 2	Used water holding tank
Test Section	Borosilicate processing glass, H.S. Martin 4"x4"2" tee with various 2" branch line sections.
V RCCS	Valve to RCCS facility water supply line
V1	Tank 1 isolation valve
V2	Tank 2 isolation valve
V3	Return flow diversion to Tank 2 valve
V4	Loop bypass valve
V5	Pump head charging valve
V6	Upstream line isolation valve
V7	Downstream line isolation valve
V8	Air evacuation valve
V9	Branch line injection/drainage valve

there are inherently differences between simulation cases due to the geometric change. Issues between cases related to the generation of meshing schemes between cases were mitigated by analyzing their respective wall treatments. Discussion of the wall treatment analysis, additional plots, and representations from the CFD study are found in Appendix A.

Although the main line for the ReBL-TF facility was reduced from a typical NPP diameter, the branch line diameter used in the CFD study, 50.8 mm, was maintained. This diameter is at the upper end of typical NPP emergency coolant injection lines (38.1-50.8 mm). Reducing it would not have a distinguishable benefit in terms of cost or operational energy expenditure like reducing the main line. However, the larger diameter branch line made internal access for measurement alignment and calibration purposes easier (Section 2.2.2).

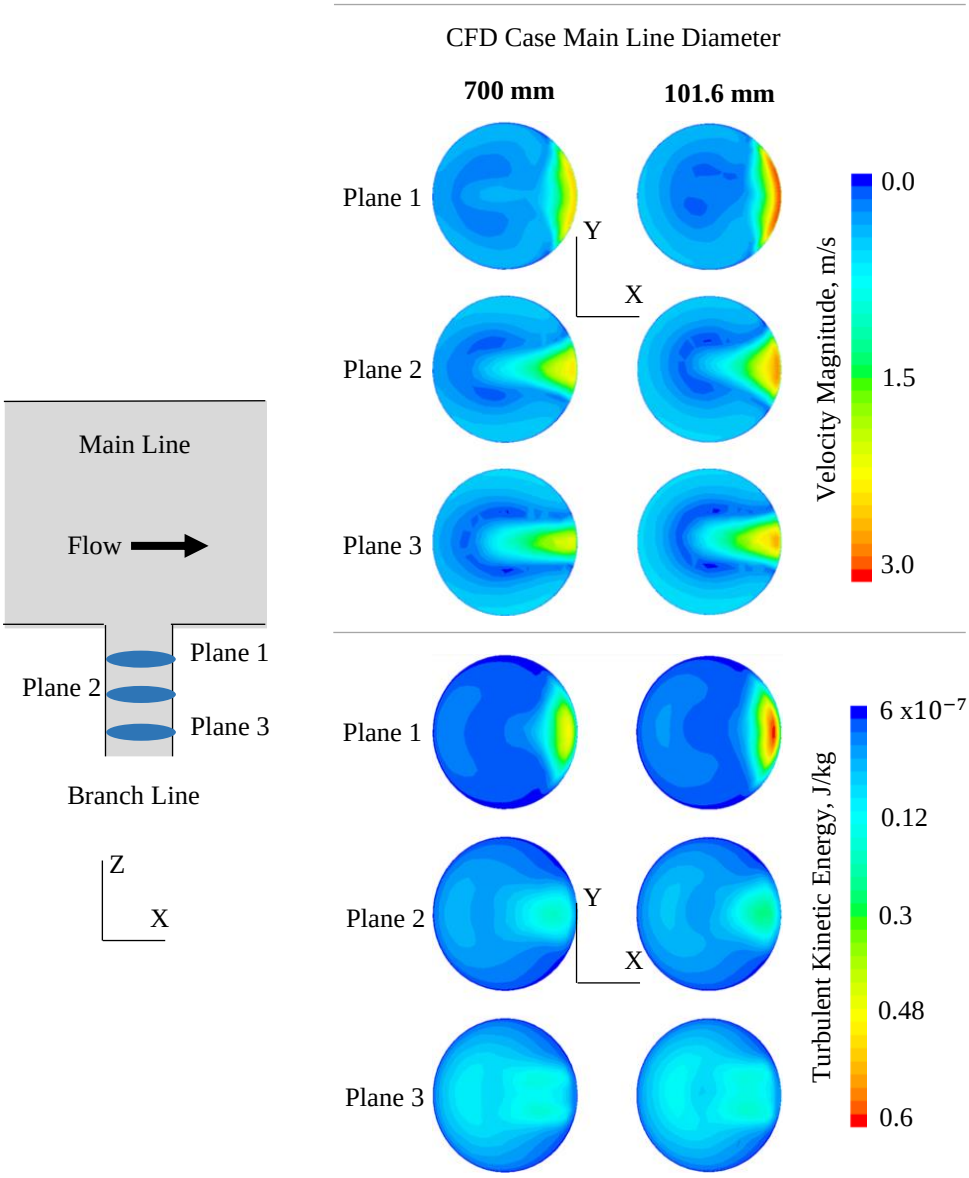

Figure 2-13 Selected planes from the branch line of two different CFD cases. The velocity magnitude and turbulent kinetic energy do no vary greatly between the 700 mm and 101.6 mm cases. Further discussion in Appendix A

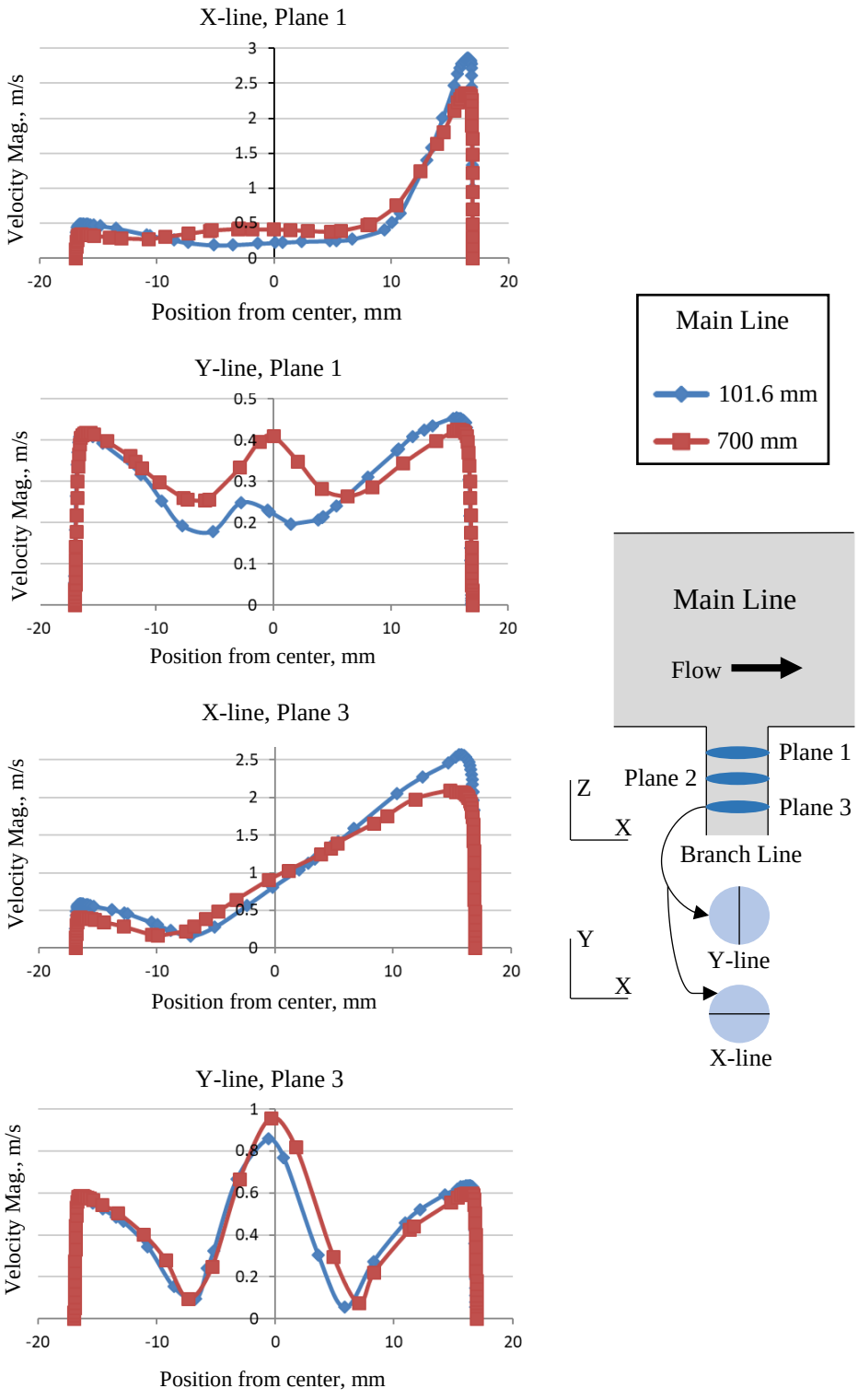

Figure 2-14 Velocity profile comparisons of CFD study cases used to inform ReBL-TF scaling. Baseline NPP scale 700 mm diameter case and the selected 101.6 mm case. Plane 2 plots can be referenced in Appendix A.

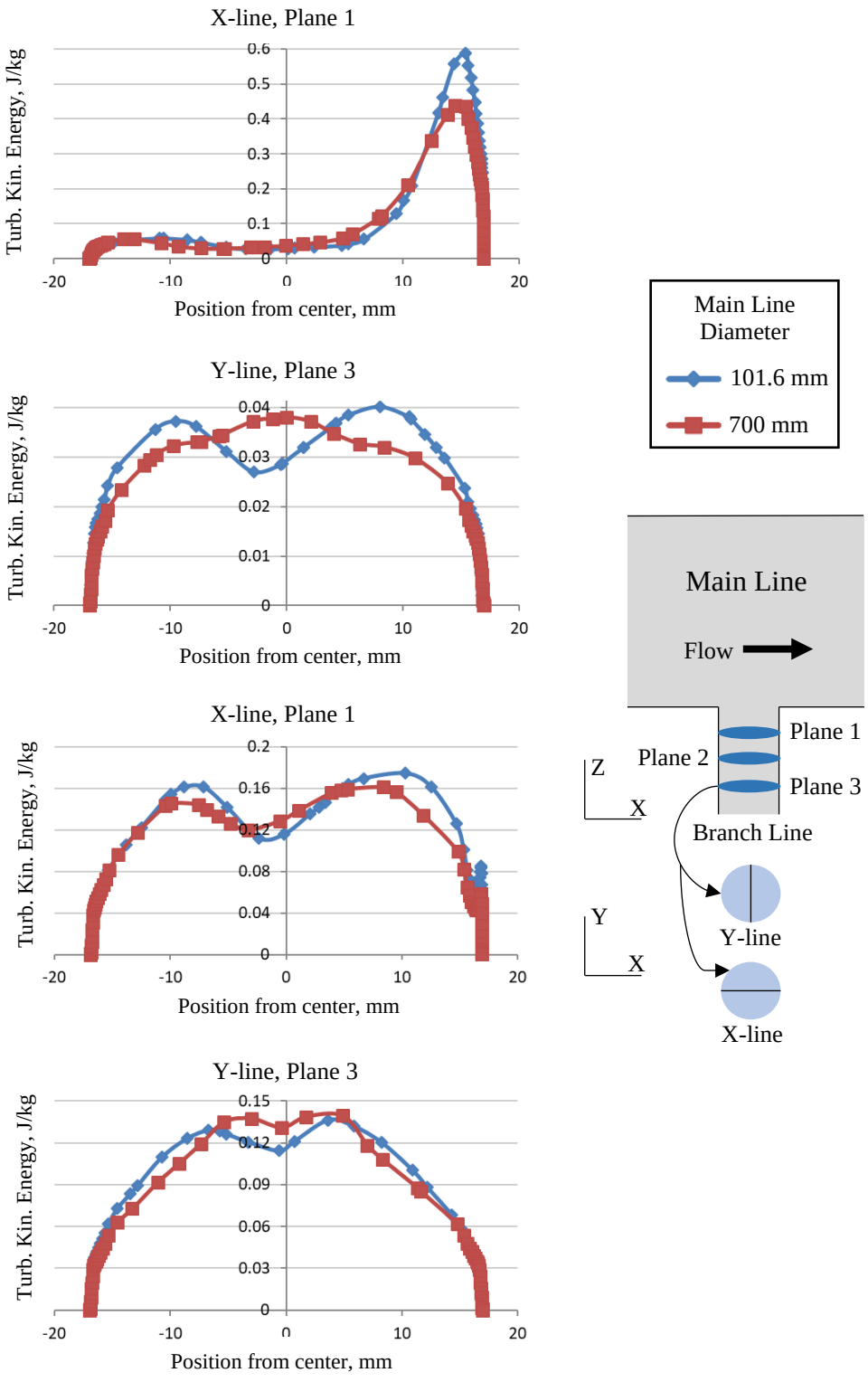

Figure 2-15 Turbulent kinetic energy profile comparisons of CFD study cases used to inform ReBL-TF scaling. Baseline NPP scale 700 mm diameter case and the selected 101.6 mm case. Plane 2 plots can be referenced in Appendix A.

The test section, comprised of the main line immediately upstream and downstream of the branch line junction and the branch line itself, was made of clear, borosilicate glass to facilitate optical measurements (Figure 2-16). As discussed in Section 2.1, the use of non-intrusive, high-resolution measurement techniques were a primary goal of this work and therefore dictated the use of optically clear piping. Borosilicate glass piping is widely used in industrial-chemical processes and is easily available off the shelf. The coupling style of the glass components makes rearranging them, or adding parts like elbows for future work, convenient.

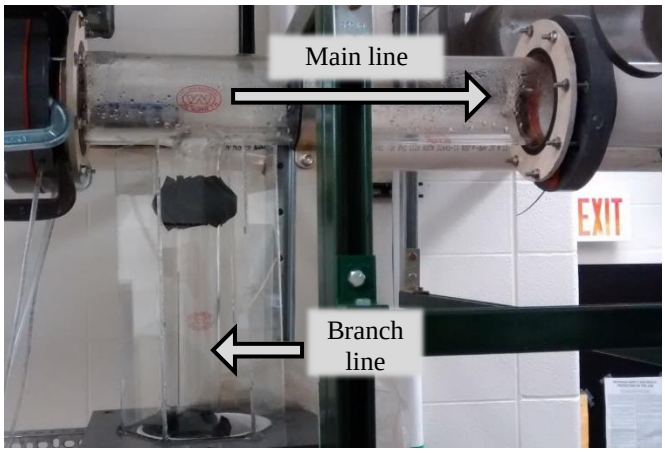

Figure 2-16 Glass test section installed in the ReBL-TF facility.

Initial plans to pump water through the main line of the loop at NPP typical rates near 10 m/s were inhibited by the laboratory's power supply. However, at the time of design and construction of the ReBL-TF loop, additional ECMF space and electrical capabilities were forthcoming. It was decided at that point to implement what was currently feasible and plan to retrofit greater pumping capabilities when possible. The initial pump installed, which was used for the duration of the ReBL-TF studies, was designed to move a maximum of 1,135 LPM at max efficiency. Along with the chosen main line diameter of 101.6 mm, this flow rate yielded a maximum main line flow rate of 2.33 m/s.

Consistent main line flow rates were achieved by controlling the pump motor with a variable frequency drive. When steps in the drive frequency did not correspond with the desired flow rate, a valve on the bypass loop was throttled for minor adjustment. The main line flow rate

was determined by readings from a turbine style flow meter (Table 2-2) and verified using LDV measurements of the flow profile.

Preceding the branch line junction, the main line section was straight and uninterrupted for 4.5 m to allow the turbulent flow to become fully developed. Immediately before the test section, three azimuthally positioned, 3 mm injection lines were installed. These lines allowed measurement or visualization particles to be seamlessly added to the flow. After the main line flow crossed the branch line junction there was a 0.7 m straight length of piping before elbows were used to redirect the water for circulation.

2.3.2 Rectangular Profile Loop Facility

The Rectangular Profile Loop (RPL) was constructed as one part of ECMF laboratory's expansion of research capabilities related to thermal fatigue onset in reactor coolant branch lines. Construction of the loop was expedited through retrofitting the existing ReBL-TF facility (Section 2.3.1) with a different main line segment (Figure 2-17). The rectangular main line profile, which is akin to a facility first reported on by reference [35] allows flow rates above 10 m/s to be achieved with the same ReBL-TF operational components.

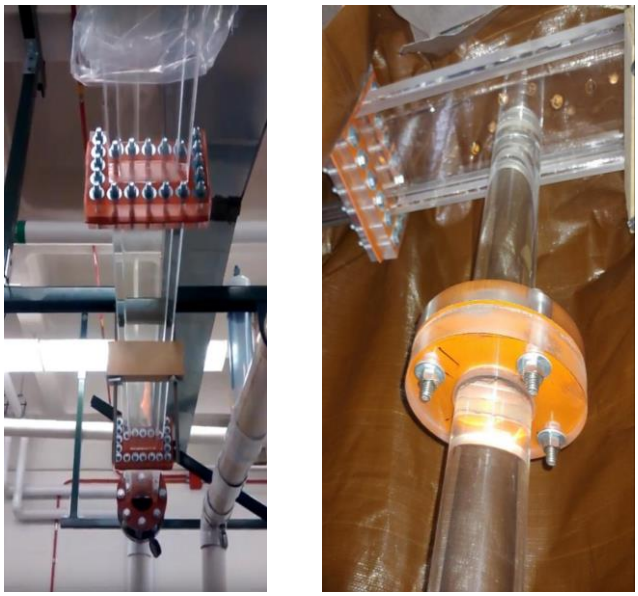

Figure 2-17 Left: RPL main line flow development section upstream of branch line junction. Right: RPL branch line junction, with branch line oriented downward.

Expanding ECMF facilities to include an experimental branch line loop with a rectangular profile main line adds functionality and breadth to its research endeavors in three specific ways. First, the similarity of the RPL main line geometry to

the that of the studies addressed in Section 1.2 ([21] [22]) allows ECMF work to build upon it directly, adding high-resolution branch line data. Second, the flat geometry of the RPL main line that intersects with the branch line more closely resembles the curvature of the main line of a NPP scale loop intersecting a 50.8 mm branch line (Figure 2-18). Third, the flat geometry of the main line makes it straightforward to adapt the branch line opening lip to have various curvatures for further studies (Figure 2-19).

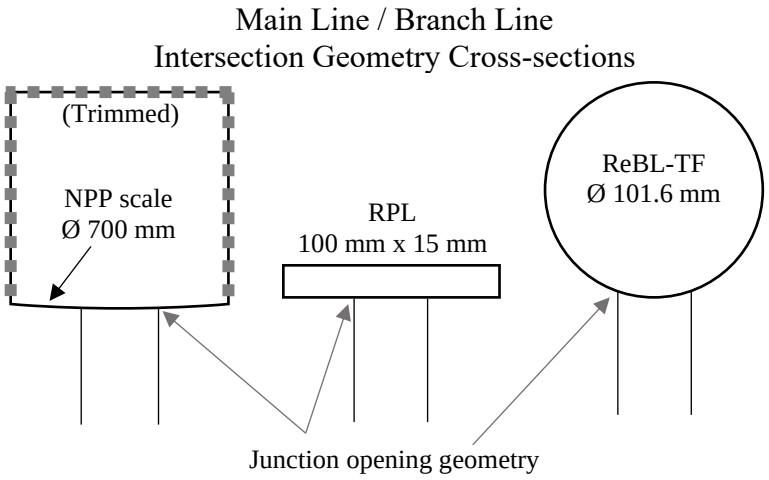

Figure 2-18 Main line and branch line intersection geometries for a NPP junction, the RPL, and the ReBL-TF

Construction of the RPL required replacing a section of the ReBL-TF main line, which included the test section, with custom rectangular profile piping. The segment that was replaced was between P1 and V7 of the Figure 2-12 schematic. As with the ReBL-TF facility, the round profile branch line intersected the main line perpendicularly and was oriented downward.

RPL custom rectangular piping was constructed from cast acrylic. Sheet and tube acrylic have become common building materials in the ECMF lab due to their low relative cost and their conduciveness with optical measurement techniques. The piping was designed in-house and professionally fabricated by a third party.

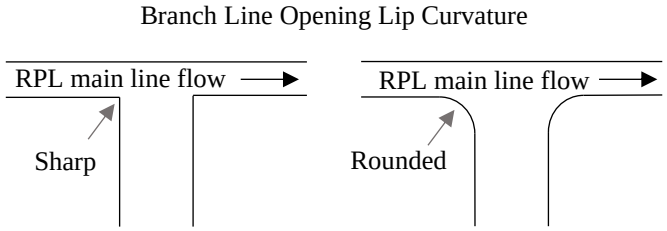

Figure 2-19 Branch line opening lip geometry curvature. Left: currently installed branch line lip geometry. Right: exaggerated reference of potential lip geometry change.

Sizing the custom rectangular piping's flow channel was informed by CFD studies. Dimensioning the channel had to meet two critical criteria. First, the combination of the channel's cross-sectional area and the 1,135 LPM flow capacity of the existing pump had to produce main line flow rates above 10 m/s. Second, the width of the channel had to be great enough so that secondary flow phenomena in the corners of the channel would not greatly disturb the flow profile crossing the branch line opening. To meet the first criteria, the cross-section could be no larger than 1850 mm^2. CFD simulations of suitable geometries ranging from 60-100 mm in width and 10-15 mm in height were conducted using Star-CCM+. Evaluating the developed bulk flow that would cross the branch line opening per case was done by comparing the velocity and TKE along various line probes. Figure 2-20 represents some of those line probes overlain on the results of the 100 mm x 15 mm case, which was selected as the geometry for construction. Corresponding velocity profiles for those probes are shown in Figure 2-21. The strong similarity across the profiles was not present for

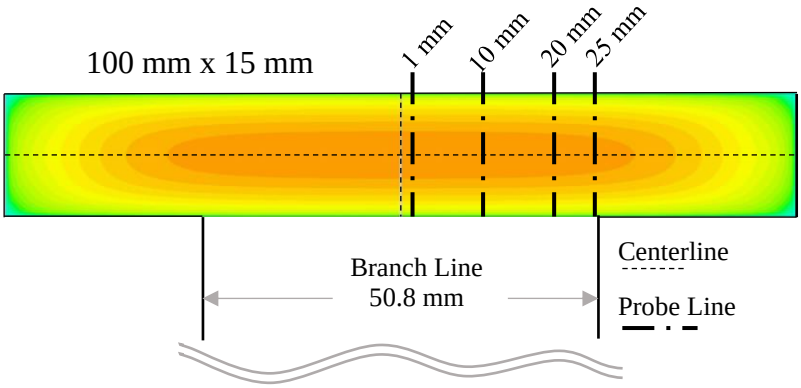

Figure 2-20 Cross-section of the RPL geometry with results from the profile development CFD study.

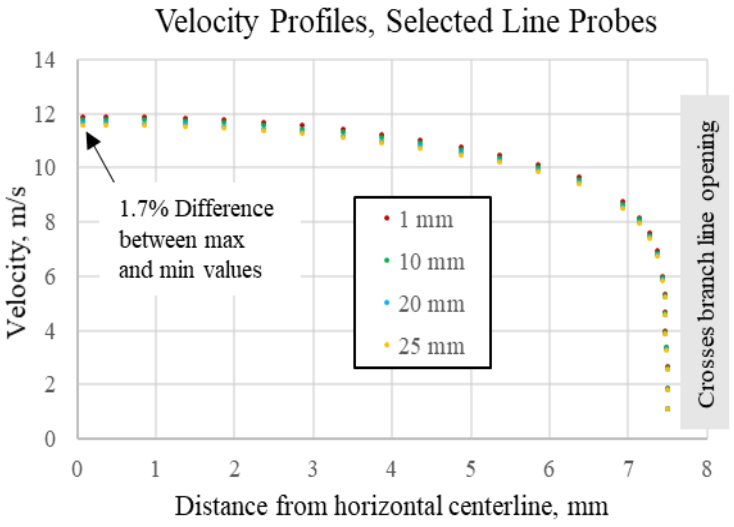

Figure 2-21 Plot of velocities along selected line probes from the rectangular flow channel sizing CFD study.

cases closer to 60 mm in width, where the centerline velocity values between probes differed by ~20%. The 100 mm x 15 mm dimensions (1500 mm^2) also permitted a max theoretical flow rate of 12.6 m/s, thus satisfying both criteria.

Wall thicknesses for the channel were determined using FEA and practical lab experience. An FEA study was employed to ensure that the rectangular channel would not deflect greatly when internally pressurized. As expected, the study showed that the greatest deflection would be along the longer dimension of the channel and the greatest stress would be at the corners. Acrylic sheeting of 25.4 mm thickness was used for the walls of the long dimension (100 mm) to ensure rigidity. Side walls along the short dimension (15 mm) were 19 mm thick to ensure strength at the corners and a large surface area for material bonding in construction.

The branch line that extended from the main line, was made of 6.35 mm thick acrylic tubing. As constructed, the branch line stubbed out 330 mm from the main line uninterrupted before a flange. The fixed acrylic flange at the end of the stub was designed to mate with a 2-inch Class 150 flange for easy adaptation. The junction section of the main line is 0.5 m long and able to be replaced for future work as needed. This will facilitate future work that includes studies of the branch line opening geometry's effect on the overall branch line flow.

2.3.3 Swirl Separate Effect Facility

After measuring and observing the flow structures in the ReBL-TF branch line, it became clear that a separate effect facility for investigating the flow that approaches the penetration boundary in the branch line would lend insight. As will be discussed in Chapter 3, the dominant structure in the flow that precedes the penetration boundary (PB) is a swirl about the branch line axis. This axial swirl develops several diameters before the PB, so understanding its decay leads a better understanding of the PB's formation in the branch line.

To generate an isolated swirl in a branch line, the SSEF was constructed from three primary components: a servo motor, a stirring paddle, and a branch line (Figure 2-22). The servo motor, model: 640-DST-A6HS1, was used to rotate the paddle at constant rates within 1 rpm of specified. The 25 mm diameter coin style paddle (Figure 2-23) was used to stir the fluid in the branch line, creating the flow swirl. The branch line was constructed of 3.2 mm thick acrylic tubing with an inner diameter of 44.4 mm. This diameter falls between the common NPP emergency coolant branch line diameters of 38-51 mm, making results from this system directly transferable. Seamless acrylic construction allowed high-fidelity, high-resolution optical measurements to be made at any position in the 30-diameter long, straight branch line.

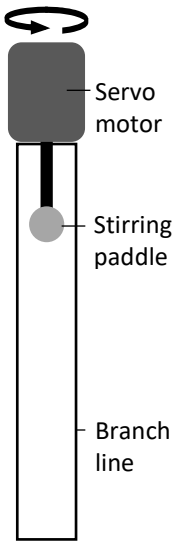

Figure 2-22 Diagram of swirl separate effect facility.

During design of the SSEF, we became privy to additional work done by EPRI [36] with separate effect facilities of their own. Their facilities were constructed with 152-203 mm diameter branch lines to accommodate instrumentation. The primary measuring devices were vane type swirl sensors and cobra type yaw probes that directly interacted with the flow. The SSEF in the ECMF lab had distinct advantages over the EPRI facilities due to the nonintrusive measurement methods employed and the scale of the branch line. However, the coin style paddle used in the EPRI studies was adopted as the fluid driver, along with corresponding stirring rate correlations.

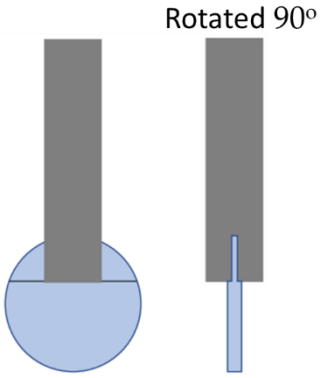

Figure 2-23 Coin style stirring paddle adapted from EPRI reference.

2.3.4 High-Capacity Loop Facility

The High-Capacity Loop (HCL) was constructed as one part of ECMF laboratory's expansion of research capabilities related to thermal fatigue onset in reactor coolant branch lines. The main line design was based on the previously implemented ReBl-TF facility, with the goal of achieving NPP main line flow rates around 10 m/s (See Section 2.3.1). The facility was constructed in the new ECMF laboratory space recently acquired in the Nuclear Engineering Laboratory on the University of Michigan campus.

Increasing the flow rate through the 101.6 mm main line for the HCL was done by acquiring a high-capacity pump and upsizing the remaining circulation piping accordingly. At peak efficiency, the Berkeley Pump (B6JPBM) could supply 5,300 LPM, which yielded a main line velocity of 10.9 m/s. Pushing the flow rate to 7,200 LPM to achieve a main line velocity of 14.8 m/s was also possible due to the strength of the pump. The 37.3 kW motor of the pump was

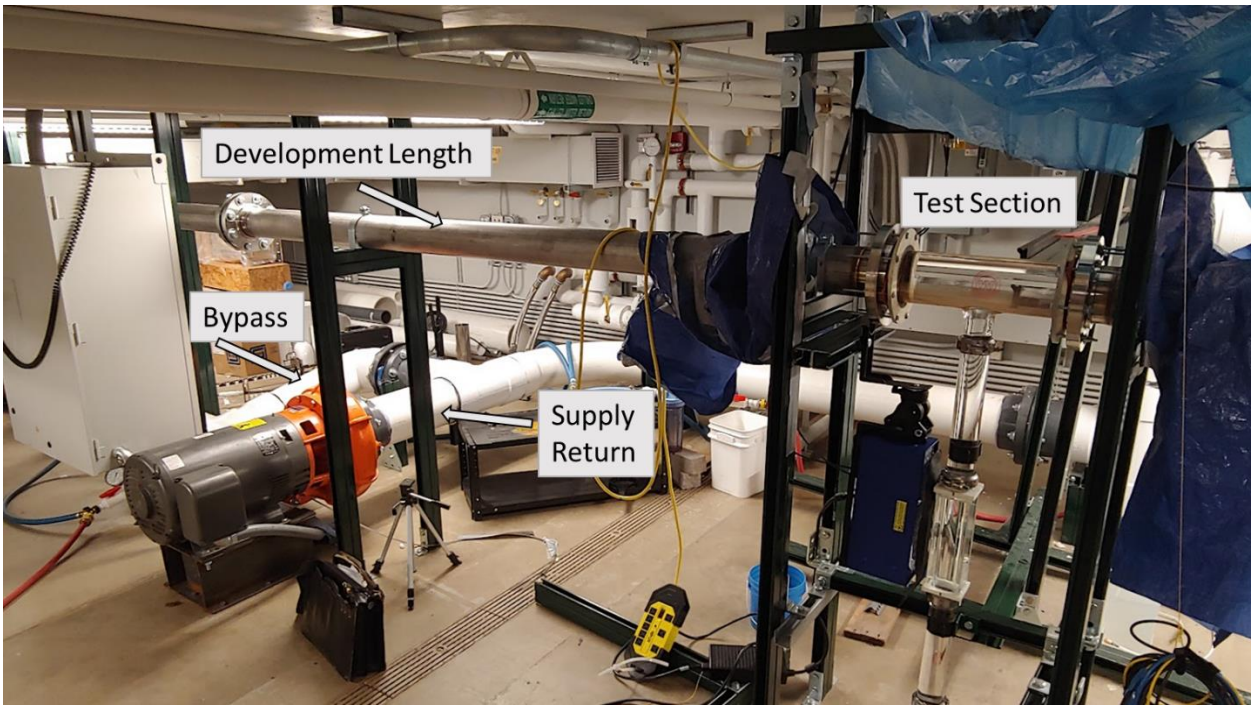

Figure 2-24 HCL facility, glass test section with branch line oriented downward.

Table 2-3 List of schematic components and their respective details from Figure 2-25.

HCL Schematic Component List

Component Label	Description
Chilled Water	Lab facility supplied service. 10° C supply temperature, max flow rate
Filter	Canister filter, 5-micron media
Flow Meter	Model: 8" Promag55, Magnetic flow meter, accuracy 0.2% reading
HX	Plate style heat exchanger
Pump 1	Model: B6JPBM, Berkeley pump, capable of 5,300 LPM at efficiency. Coupled to 37.3 kW Baldor motor and controlled by ABB variable frequency drive
P1	Direct readout pressure gauge
Test Section	Borosilicate processing glass, H.S. Martin 4"x4"2" tee with various 2" branch line sections.
V1	Loop bypass valve
V2	Loop filling and draining valve
V3	Branch line injection and drain valve
V4	Air bleeding valve
V5	Filter line valve
V6	Heat exchanger supply valve

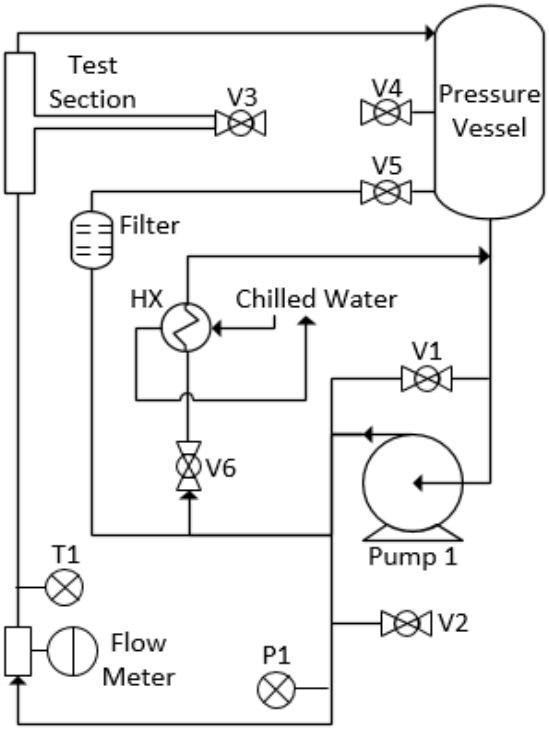

Figure 2-25 Schematic of HCL facility. Corresponding information about the components labeled can be found in Table 2-2.

controlled using an ABB variable frequency drive. Circulation piping was sized to a diameter of 203.2 mm to adequately supply the centrifugal pump and to reduce possible friction losses.

The HCL also deviates from the ReBL-TF design by reducing the number of valves involved, removing the flow conditioner, and utilizing a non-obstructive flow meter to reduce flow resistance. Reducing the valves in the circulation loop yielded direct decreases in the loop's overall resistance. Removing the flow conditioner decreased the loop's theoretical flow resistance significantly, increasing the potential maximum flow rate. Its removal was justified by the 4.8 m long flow development length preceding the test section. Such a length is 48 diameters, which exceeds the general recommendation of 10 diameters and the conservative 40 diameter proposed by Nikuradse [37] for turbulent flow development in smooth pipes (Figure 2-24). The flow meter

installed was an Endress+Hauser magmeter (ID 203.2 mm), which does not obstruct the flow significantly.

A heat exchanger (HX) loop was installed on the HCL to counteract the heat generated by operating the loop at high flow rates. The loop's circulated water was driven through the HX loop by the primary pump (Figure 2-25). The chilled water exchange was provided by the laboratory facilities which supplied 10^{o} C water at a maximum rate of 56 LPM. Chilled water flow rates between 2-5 LPM maintained the loop to within 1^{o} C of desired temperatures during operation.

Flow through the filter media of the loop was also driven by the primary pump. The canister style filter used a cartridge to filter out particles greater than 5-microns. The filter was only used between experimental runs to clarify the water as needed.

The test section was positioned in the lab in a location that allowed it to be rotated 360^{o} about the main line axis. This flexibility in the design allows the branch line to be oriented downward, horizontally, or upward to meet measurement objectives (See Chapter 5). For the current work, the branch line was maintained in the downward orientation.

The pressure vessel is a column of larger diameter piping that served as the loop's air evacuation system. Each time the branch line piping was rearranged, the filter cartridge replaced, or the water supply exchanged, refilling the loop with water introduced air into the system. To remove the resulting bubbles, the flow was circulated at progressively higher rates to sweep them to the pressure vessel. The physical layout of the loop, with the pump low and the return line high, was designed to not trap air in any other location. Once in the pressure vessel, bubbles rose to be vented out the top. Ensuring that bubbles rose in the pressure vessel and were not simply swept along with the flow was accomplished by augmenting the pressure vessel's cross-section. At 254 mm in diameter, the cross-section of the pressure vessel yielded a volumetric flow rate 6.25

times lower than that of the 101.6 mm main line. After the primary bubble removal process, flow still passed through the pressure vessel, helping to ensure that any possible remaining air would likely be removed from the flow during measurement runs.

Chapter 3 Experimental Results

3.1 Overview

As described in Chapter 2, the experimental work for this study included multiple facilities and measurement systems. Within the discussion that follows, results will be shown from combinations of the following facilities and techniques:

- Experimental facilities: Reactor Branch Line – Thermal Fatigue (ReBL-TF), Rectangular Profile Loop (RPL), High-capacity Loop (HCL), and the Swirl Separate Effect Facility (SSEF)
- Measurement techniques: Laser Doppler Velocimetry (LDV), Particle Image Velocimetry (PIV), and Tomographic Particle Image Velocimetry (T-PIV).

The facilities and techniques used demonstrate the evolution of the work as knowledge was obtained and more sophisticated measurement systems were acquired. Table 3-1 and Table 3-2 contain lists of the measurements that will be referenced in the discussion that follows.

*Table 3-1 Measurements of the flow swirl's tangential velocity in the branch line at various axial positions. Each case listed has measurements at sequential axial positions, which demonstrate the decay trend of the flow swirl as it penetrates the branch line. Values marked with * are based on EPRI provided correlation.*

LDV Measurements of Tangential Swirl Velocity in Branch Line				
Facility	**Main Line Flow Velocity (m/s)**	**Stirring Rate (rpm)**	**Fluid**	**Tempertature (C)**
RPL	6.8		Tap water	20
RPL	10		Tap water	20
SSEF	*3.76	400	Tap water	19.4 C
SSEF	*4.7	500	Tap water	19.4 C
SSEF	*5.64	600	Tap water	20
SSEF	*6.58	700	Tap water	20
SSEF	*9.41	1000	Tap water	20
SSEF	*12.22	1300	Tap water	20
SSEF	*14.1	1500	Tap water	20
SSEF	*9.13	971	Brine	19.4
SSEF	*13.04	1387	Brine	19.4
SSEF	*16.95	1803	Brine	20
SSEF	*10.39	1105	Glycerine Sol.	20
SSEF	*12.6	1341	Glycerine Sol.	20
SSEF	*14.84	1578	Glycerine Sol.	20
SSEF	*10.35	1101	Sugar Sol.	19.4
SSEF	*12.6	1336	Sugar Sol.	19.4
HCL	1.5		Tap water	19.4
HCL	5.0		Tap water	19.4
HCL	8.0		Tap water	19.4
HCL	9.43		Tap water	20

First, results from initial investigations of the flow phenomena in dead-ended branch lines will be shared. The initial studies were conducted utilizing the ReBL-TF with LDV and PIV measurements. Next, comparable LDV measurement results from the RPL branch line will be

*Table 3-2 Measurements of branch line velocity fields. PIV measurements for the ReBL-TF cases, and T-PIV for the remaining cases listed. Values marked with * are based on EPRI provided correlation.*

PIV and T-PIV Measurments of Swirl Velocity Fields in Branch Line					
Facility	**Main Line Flow Velocity (m/s)**	**Stirring Rate (rpm)**	**Branch line Region**	**Fluid**	**Tempertature (C)**
ReBL-TF	2.13		R1	Tap water	20
ReBL-TF	2.13		R2	Tap water	18.9
ReBL-TF	2.13		R3	Tap water	20
ReBL-TF	2.13		PB	Tap water	20
ReBL-TF	2.33		R1	Tap water	19.4
ReBL-TF	2.33		R2	Tap water	20
ReBL-TF	2.33		R3	Tap water	19.4
ReBL-TF	2.33		PB	Tap water	19.4
SSEF	*8.0	850	Near Paddle	Tap water	20
SSEF	*8.0	850	Mid region	Tap water	20
SSEF	*8.0	850	PB	Tap water	19.4
HCL	7.30		R2	Tap water	20
HCL	9.43		R2	Tap water	18.9
HCL	5.97		R3	Tap water	19.4
HCL	9.34		R3	Tap water	20
HCL	5.53		PB	Tap water	20
HCL	6.52		PB	Tap water	19.4
HCL	7.94		PB	Tap water	19.4
HCL	8.62		PB	Tap water	19.4
HCL	8.85		PB	Tap water	20
HCL	9.40		PB	Tap water	20

discussed. Following that discussion, results from the SSEF, where LDV and T-PIV techniques were employed will be presented. Then, to build upon the previously acquired data, LDV and 3D velocity field measurements from the HCL facility will be presented.

3.2 Initial Findings – ReBL-TF

Previous research established that there are three distinct regions of interest in determining the flow development in reactor emergency coolant branch lines (Section 1.2). Figure 3-1 illustrates the locations of these regions relative to their position in the branch line. The first region (R1) is believed to be dominated by a cavity-like flow structure. The second region (R2) exhibits an unclear transition from the cavity-like flow structure to the swirl that persists into the branch line. The third region (R3) contains a vortex like flow, rotating about the branch line axis until reaching the penetration boundary (PB).

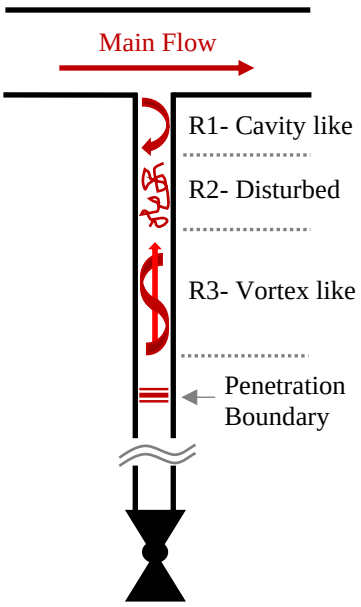

Figure 3-1 Representation of the regions of interest in the branch line.

Measurements in the regions of interest were conducted at the ReBL-TF test section using PIV and LDV techniques. Measurement locations were selected for PIV measurement based initially on the findings of Ref. [21], so that the perceived flow behaviors of each region could be quantified. LDV measurements were used to verify the results captured using PIV. Locations of measurements are referenced using L/D values, where L is the distance into the branch line from the opening and D is the branch line diameter.

3.2.1 R1 Velocity Field Measurements – ReBL-TF

When there is no leakage into or out of a standard emergency coolant branch line, all the fluid exchange in the branch line is caused by the interaction of the passing main line flow. The main line flow shears the branch line fluid at the junction opening as it passes and interacts with the branch line opening's lip geometry (Reference Figure 2-19). Theoretically, this initiates a

cavity like flow in R1 of the branch line. However, seeing that the translational energy of the main line is converted to a rotational energy about the branch line axis, it is evident that there are other competing traits in the flow of R1.

PIV measurements in the x-z plane of R1 captured the expected cavity flow structures and measurements in the y-z plane of the same segment revealed strong z-directional flows (Figure 3-2). Considering both velocity fields in Figure 3-2, the upper segment (L/D < 2) contains a rotation about a y-axis that is counterclockwise, while the lower segment's average motion is less distinct. Large arrows overlaid on the figure highlight the average flow direction in each region. For the upper portion, Vx is moving left-to-right, Vz is moving downward on the left and upward on the right, demonstrating a likely counterclockwise eddy with a center near L/D = 1.5. The lower segment of the same measurement possibly contains a secondary eddy (rotating the opposite direction) but it appears that most of the flow's energy in that section of the plane is concentrated in the z-components. This is further demonstrated by the Vz component in velocity field measured in the y-z plane of Figure 3-3.

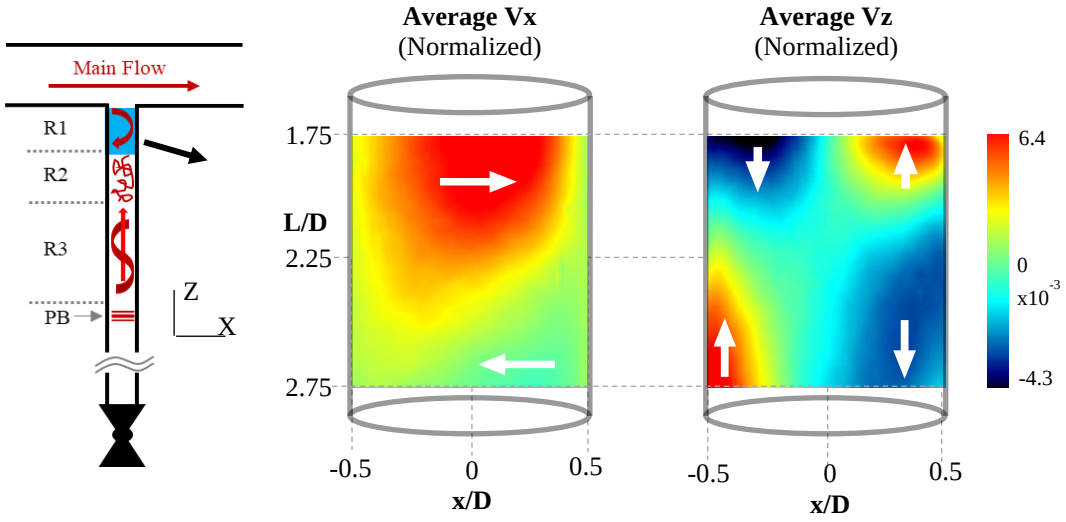

Figure 3-2 Measurement of the x-z center plane. Example flow profile in the R1 region.

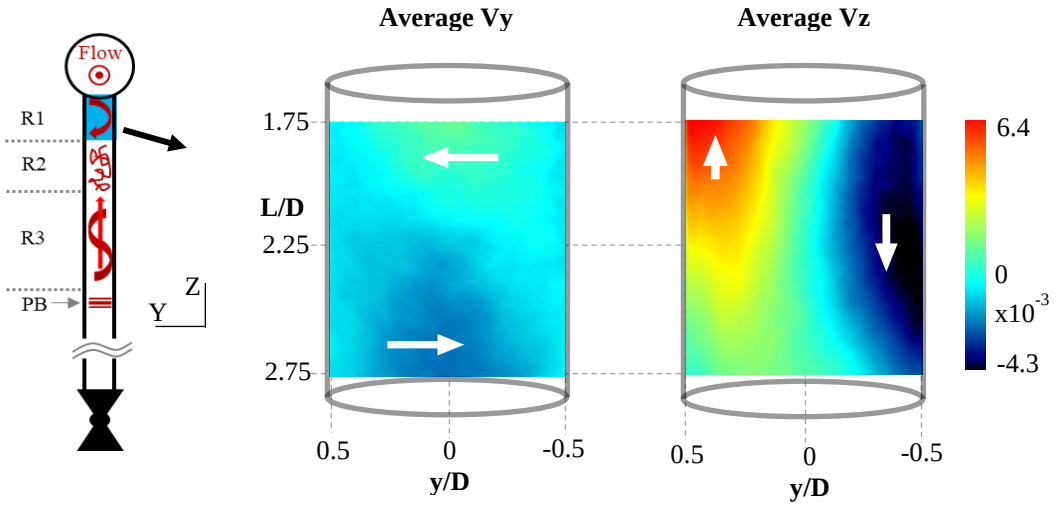

Figure 3-3 Example flow profile in the R1 region at the center y-z plane of the branch line.

Rotating the measurement plane 90° in the same segment of R1, the strength of the vertical flow is demonstrated. The vertical flow characteristics present resemble the flow structures that persist further into the branch line (see further discussion of R3, Section 3.2.2). The strength of the upward and downward flows is evidence for the phenomena driving the exchange of main line fluid into the branch line.

The disparity between the patterns of the average velocity fields captured in the x-z and y-z center plane measurement merited further investigation. As part of that effort, LDV measurements were made to see which characteristics of the flow dominated around a distance from the branch line inlet of L/D = 2.1, where there appeared to be an inversion in the direction of the flow structures, as indicated by the change in sign of the velocity component Vy (Figure 3-2). The LDV measurements were conducted by scanning the cross-section of the branch line from multiple angles and mapping the results (Figure 3-4). To capture measurements within the bulk of the selected cross-section, the LDV was rotated to different viewing angles while being held in the same plane. At each viewing angle, the measurement point was advanced across the diameter to collect data. Each measurement line yielded a velocity trend that was eventually combined with

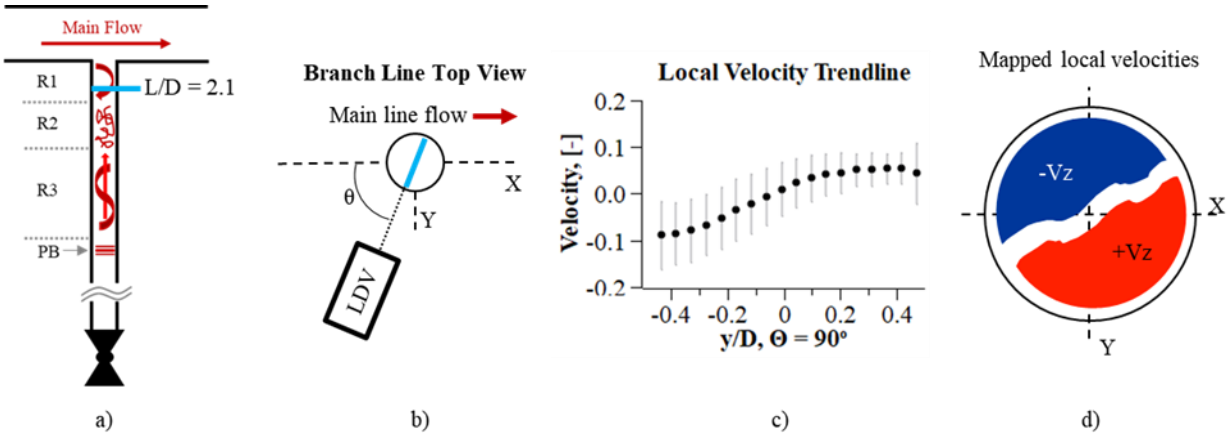

Figure 3-4 LDV scanning measurement process and result. a) Location of the cross-section being investigated, b) The LDV was rotated in the same plane to different viewing angles for measurement. At each angle, the LDV measurements point was advanced across the diameter to collect a local trend, c) Each measurement line yielded a trend of the velocity, d) The local trends were mapped to the cross-section for a view of the general trend.

the others collected to produce a general velocity field. Due to alignment/refraction difficulties LDV techniques face with curved surfaces (Section 2.2.1), measurements across the diameter in this fashion were not conducted for Vy/x. However, Vz was straightforward, as the LDV lasers effectively pass through the same flat surface of the glass when properly oriented.

Although the LDV scanning measurement method cannot capture data at all the points simultaneously, it does demonstrate the stability of the dominant structure in that region. This stability is evident in how the trends persisted over large periods of time. Each trend line gathered constituted about 25 minutes of measurement collection time, requiring several hours to collect all data over all measurement locations. In addition, some of the measurements were repeated towards the end of the measurement process for this cross-section to verify the trends captured and test for repeatability of the measurements.

The magnitudes of the average velocities captured using the LDV scanning method more closely resembled the magnitudes captured in the y-z PIV measurements. This leads to the conclusion that the x-z plane PIV measurements may have captured a unique transition in the flow. This transition may be a crisscrossing of the vertical flows which yields the visible cross like zone

of low average velocity (i.e., upward flow passing from the left to the right side of the volume and the downward from left to right in the same volume in Figure 3-2. This is possibly a consequence of only being able to measure a 2D field at the center plane. Verifying the complexity of the flow in this region would greatly benefit from 3D measurement.

3.2.2 R2 and R3 Velocity Field Measurements – ReBL-TF

After the initiation of the flow in R1of the branch line, previous qualitative observations suggested that there was distinct transition in flow behavior near an axial distance from the branch line inlet of L/D = 3 [21]. This position in the branch line was considered the onset of R2, where a disturbed flow persisted. Although reports of the R1-R2 boundary were based on main line flow velocities of 4 m/s and higher, the flat trend observed (Figure 3-5) suggested that it would also be present near L/D = 3 for lower main line flow velocities near 2.3 m/s.

Measurements of the average branch line flow around L/D = 3 did not exhibit the R1-R2 boundary expected. The flow behavior in the expected R2 portion of the branch line resembled that of much of the flow further into the line (R3), as seen in Figure 3-6. Within the figure, it is apparent that the Vz component of the flow is dominant at the center plane of the branch line. Given the swirling nature that has been observed in the branch line flow about the axis, the Vy component is likely to be only a manifestation of the helical nature of the swirl. As a result, Vy shows how the swirl is not perfectly centered along the axis, with highs and lows where the swirl is most offset. The pattern in the center plane of the

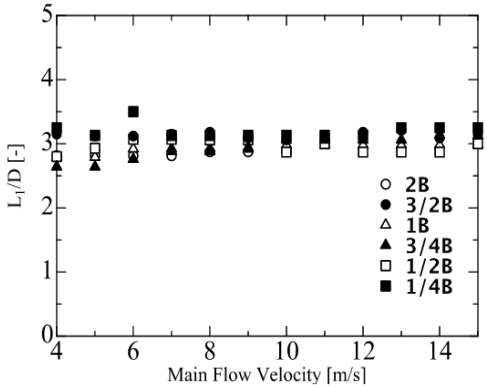

Figure 3-5 Depth of the R1-R2 boundary location in the branch line as observed by reference [21]

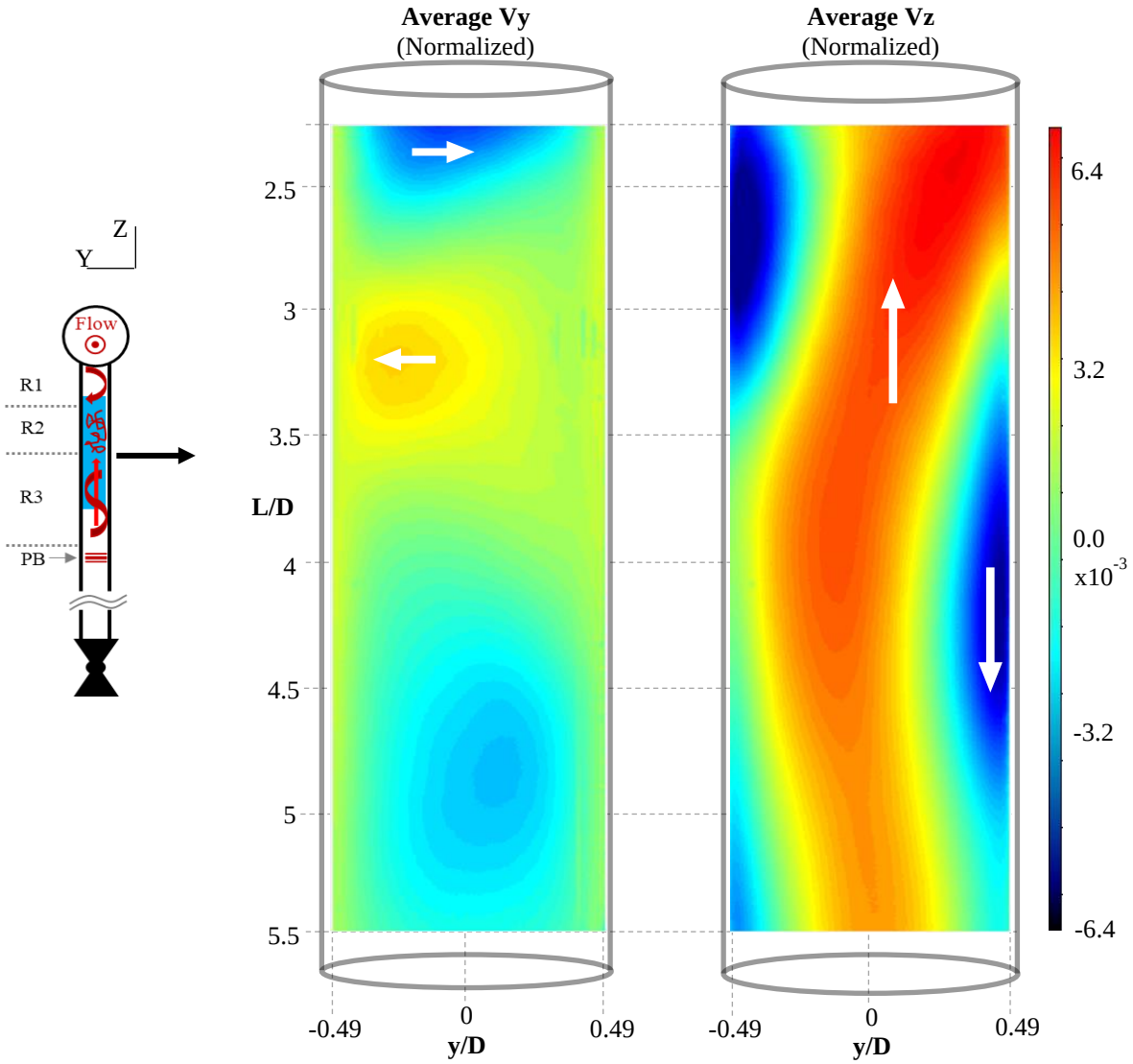

Figure 3-6 Measurement of the branch line flow capturing R2 and R3 trends at the center plane of the branch line.

Vy field (negative-positive-negative) reflects how a helix would shift the vortex of the swirl at one L/D position into the page plane, and then at another L/D out of the page plane.

The branch line's helical flow presents a serpentine structure at the center plane in Vz, which is rather stable over time. Figure 3-7 contains analysis of a complimentary measurement made in the x-z plane for the same portion of the branch line. The average velocity field shown on the right was calculated from data collected over a period of 10.1 minutes, where velocity fields

were captured at a rate of 10 Hz. The larger plot of the figure demonstrates the convergence to the mean of the Reynolds stress with respect to the number of collected data points at selected locations in the measurement field. The locations selected for the plot are labeled 1-9 in the velocity field image. Reynolds stresses are good indicators to determine convergence of flow statistics, being second order statistics of the flow's turbulent fluctuations. With the convergence to the mean demonstrated, it can be confidently said that average velocity field in this portion of the branch line at the center plane does in fact contain the serpentine structure observed over long periods of time.

Knowing that the data presented in Figure 3-7 converges well to the mean, it was worth exploring aspects of the flow in more detail. Within the figure there are three inset plots that reflect the work of such study. In the left side of Figure 3-7 there are two histograms of the velocity data gathered at location Point3 (component Vx above and Vz below). The results at location Point3

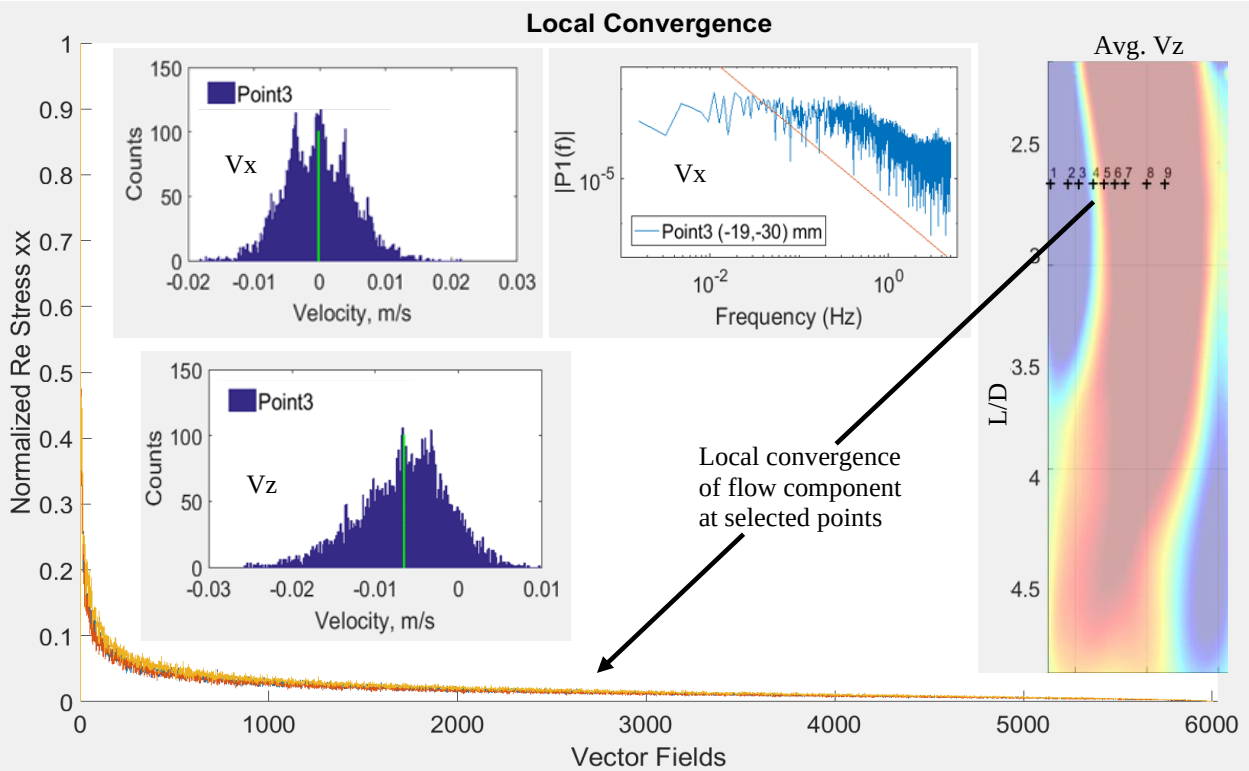

Figure 3-7 Statistical analysis of branch line measurement. Over a 10 min period the serpentine structure of the flow in the z-component was persistent.

are a good example of what was observed generally at various points in the field; fluctuations in Vz tended to be more normally distributed, while Vx fluctuations were almost all multimodal in nature. It is likely that the multimodal results of Vx reflect the sensitivity of measuring this velocity component in the center plane. If the dominant swirl were perfectly stable about the axis of the branch line, Vx would be expected to be near zero in magnitude. This is because in that plane, the tangential velocity along the axis would be comprised of the Vy component alone. Vx is therefore a telltale of the deviations from such an ideal swirl structure. It was expected that a spectral analysis of the velocity frequencies at each point would shed more light on the multipeak observations. However, there were no distinct periodic fluctuations observed on the order of 5 Hz or less, as can be seen in the inset plot to the right side.

Fluctuation frequency information above 5 Hz would have been interesting to determine to understand the local rapid changes in the flow, but it would not contribute greatly to this work. This is primarily because the rapid fluctuations present do not greatly influence the flow structure over longer periods of time. Such rapid fluctuations in the flow velocity would likely not play a part in significant thermal fluctuations at the pipe walls.

3.2.3 Axial Swirl Within R3 – ReBL-TF

With the camera's viewing angle oriented perpendicular to the branch line axis as in previous measurements, it was impossible to capture velocity fields that characterized the axial swirl. For 2D measurements in x-y cross-sections, the camera was positioned at the end of the branch line with the viewing angle parallel with the branch line axis (Figure 3-8). Viewing positions in the branch line were restricted by the focal distance of the 50 mm lens used and the obstruction of the branch line piping. A custom cap for the end of the branch line was made with an acrylic viewing window to facilitate imaging.

The position of the camera relative to the branch line piping restricted the application of a calibration plate as previously employed. This is due to the high risk of accidentally leaking water onto the camera or translation stage. As outlined in Section 2.2.2, to use the calibration plate, it must be placed in the fluid of interest, imaged, then removed to proceed with measurement. This wet procedure required opening the branch line directly above where the camera would be positioned for measurement (with the cap used as a viewing port, it was not possible to drain the branch line before opening it). Although the camera could have been translated out of the riskiest zone and then accurately returned when safe, that would have still left the translation stage vulnerable to an accidental spill. It was decided that in place of using the calibration plate, a scaling technique would be used to account for particle displacement. Scaling is done by identifying a feature in one of the images post measurement and assigning it a physical dimension. In the case of these measurements, the inner diameter of the branch line was used. Orienting the axes for this method was done through careful alignment of the camera, but it lacked the inherent accuracy of the calibration plate method. Therefore, the resultant magnitudes of isolated velocity components will not be reported here.

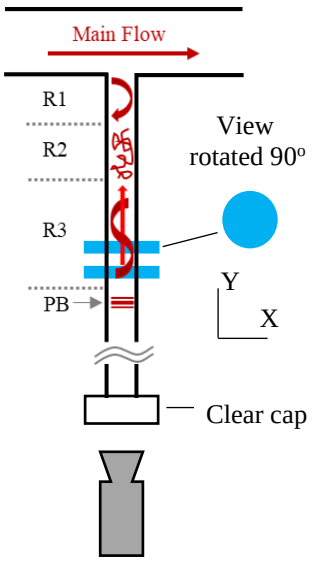

Figure 3-8 Camera orientation and field of view for axial swirl study.

Measurements at positions 7.9 - 10.3 L/D revealed a dominant axial swirl persists through the region. The general trend at each slice captured is demonstrated in the average vector field of Figure 3-9. Between cases, the average swirl rotational direction (CW) was the same. The location of the swirl's vortex varied by L/D position but

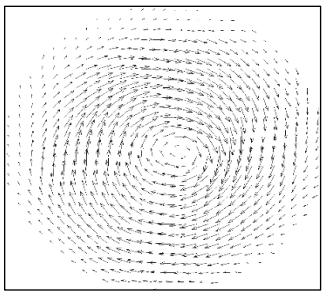

Figure 3-9 Average x-y velocity field at L/D = 10.2, main line velocity 2.33 m/s

did not deviate greatly from the central axis. As expected, the swirl's average velocity magnitude decreased at each greater L/D position (Figure 3-10).

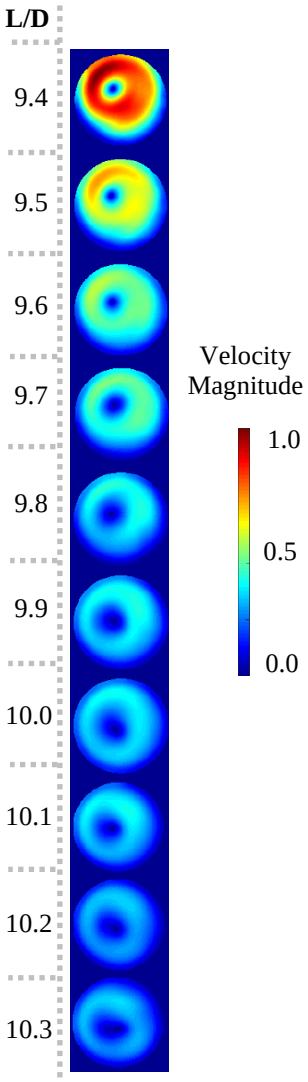

Figure 3-10 Decay of the axial swirl's velocity magnitude.

Given the significance of the swirl as a mechanism of the flow's penetration into the branch line, selected slices were further analyzed using proper orthogonal decomposition (POD). The resulting eigenvalues from the analysis supported the finding presented previously that the dominant swirl structure is rather stable. Two slices are presented in Figure 3-11 for discussion.

From measurements of the flow swirl in R3, POD analysis showed that it is primarily disturbed by minor passing vortices. With the central, axial flow moving toward the main line and the flow near the walls moving in the opposite direction, the plane being measured is affected by disturbances in both directions. Additionally, the flow was bounded by walls on all sides, isolating the dominant circular flow in the plane. With the high interdependence of the x and y components of the circular flow, it was expected that the dominant modes of one component would be an out of phase reflection of what would be found in the corresponding mode of the other component. However, this was only occasionally the case, as in the example of 8.3 L/D, Mode 4 of Figure 3-11. What was more commonly observed was a mode switching behavior like in Modes 1&2 of the same figure (Mode 1 x – Mode 2 y, split field. Mode

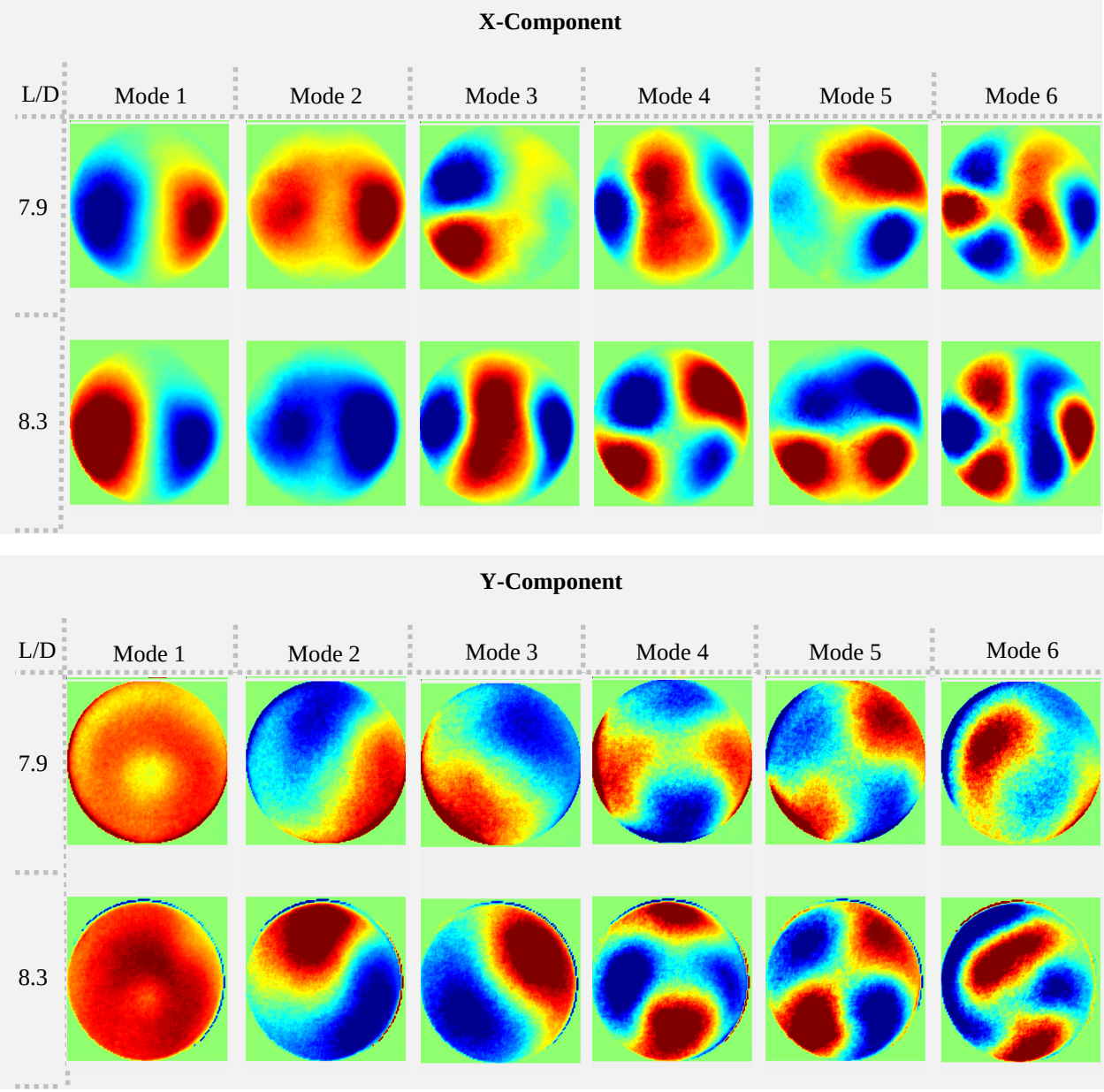

Figure 3-11 Dominant structures in the branch line swirl flow that were identified using POD. The designations of x and y components are labeled to distinguish the components of the fluctuation that are perpendicular to one another. They are aligned with the x and y axes assigned in the camera alignment process as noted in the text. Slight misalignment is conceivable so possible error should be considered in the results.

2 x – Mode 1 y, full field). In the case of the first two modes, this suggests a flow feature exists where the fluctuation of the y-component is higher energy than that of the x-component. That said, the energy contribution of the first two modes were almost the same in each of the slices measured, differing about half a percent. Figure 3-12 contains a plot of the energy of each mode for the x-component at 7.9 L/D. The total energy contribution from the primary modes is not high (~3%),

which shows that the field is not generally disturbed a great deal from the mean. There are obvious fluctuations from the mean flow but the energy in those fluctuations is low, suggesting a rather stable flow structure in R3.

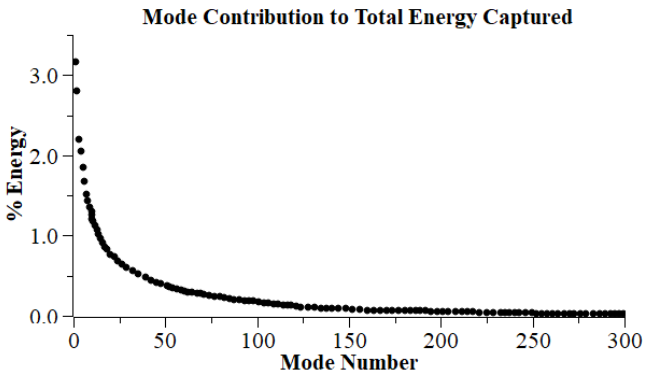

Figure 3-12 Energy contribution to the captured flow per mode.

3.2.4 Penetration Boundary – ReBL-TF

The serpentine structured flow observed in R3 persists in the branch line until reaching the penetration boundary (PB). At that point, the energy of the swirl appears to dissipate, leaving the fluid further on nearly stagnant. Within the flow, the upward central flow can be seen entraining the downward flow from near the pipe walls. This flow termination behavior can be inferred from Figure 3-13, where arrows are overlain upon the velocity fields.

Measurements of the exact location of the PB, like a crisp line between where the fluid flows and stagnates, are unlikely to be achieved due to the fluctuating nature of turbulence. In addition, as addressed in Section 2.2.3, PIV methods require particle displacement to make accurate measurements. Furthermore, the boundary is not naturally "thin" in adiabatic cases where buoyant forces do not add penetration resistance. However, to better identify the PB in the PIV measurements achieved, secondary calculations were made using components of the velocity fields to find Q-criterion values.

The Q-criterion uses the vorticity magnitude (Ω) and the mean strain rate (S) of the flow to calculate a value that relates to the energy dissipation as follows,

$$Q = \frac{1}{2}(|\Omega|^2 - |S|^2). \quad (1)$$

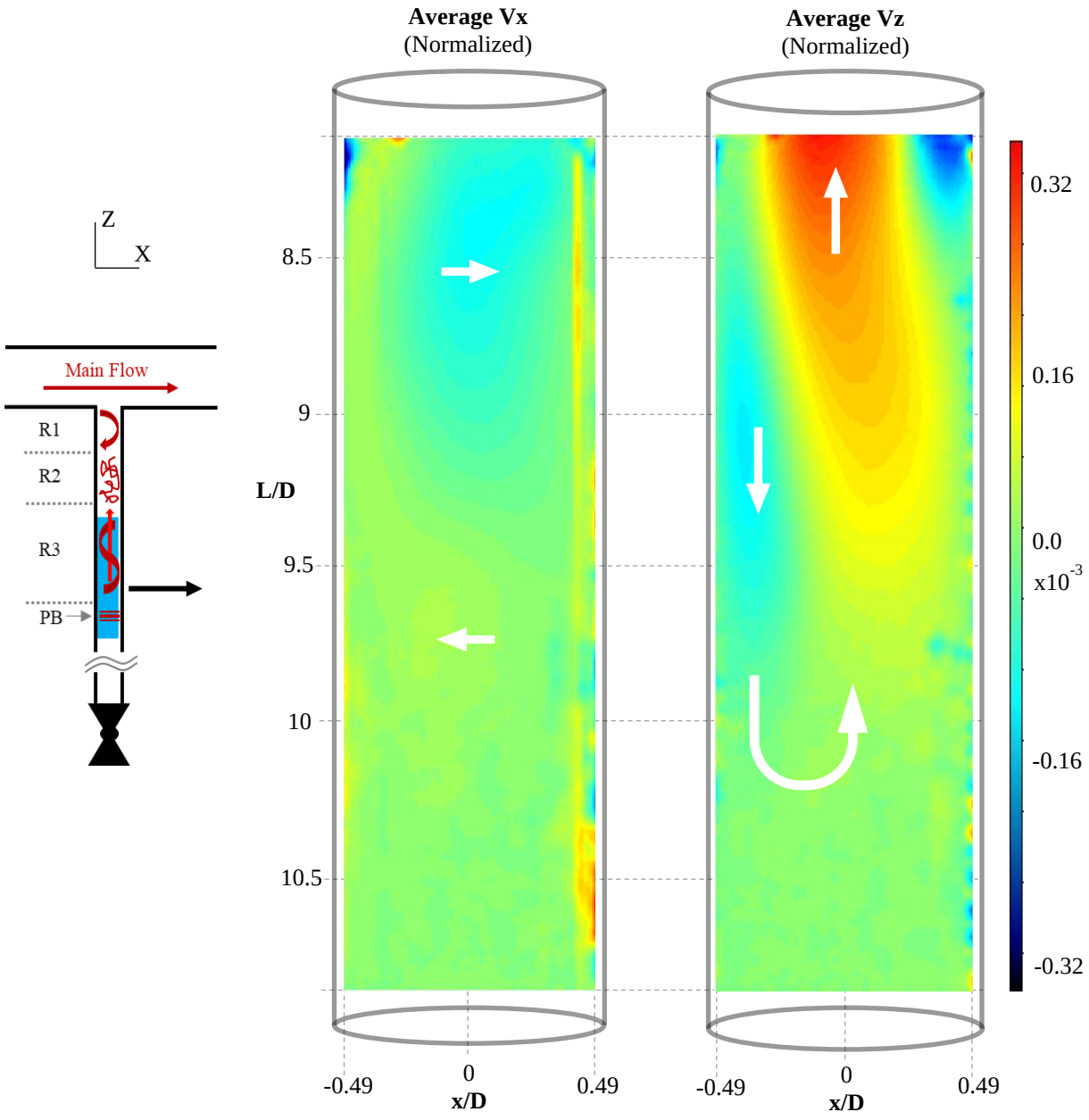

Figure 3-13 Measuremnt in the branch line of the penetration boundary. To the right side in each measurement, the outlying velocity quantities are due to reflections on the glass surface of the pipe.

In cases where the resultant value is positive, the flow is dominated by the vortical forces, whereas negative values demonstrate the dominance of viscous stresses [38]. For 3D cases, this can be an especially powerful visualization tool for identifying regions containing vortex structures of similar magnitude. In its 2D application for this study, individual Q-criterion values were not

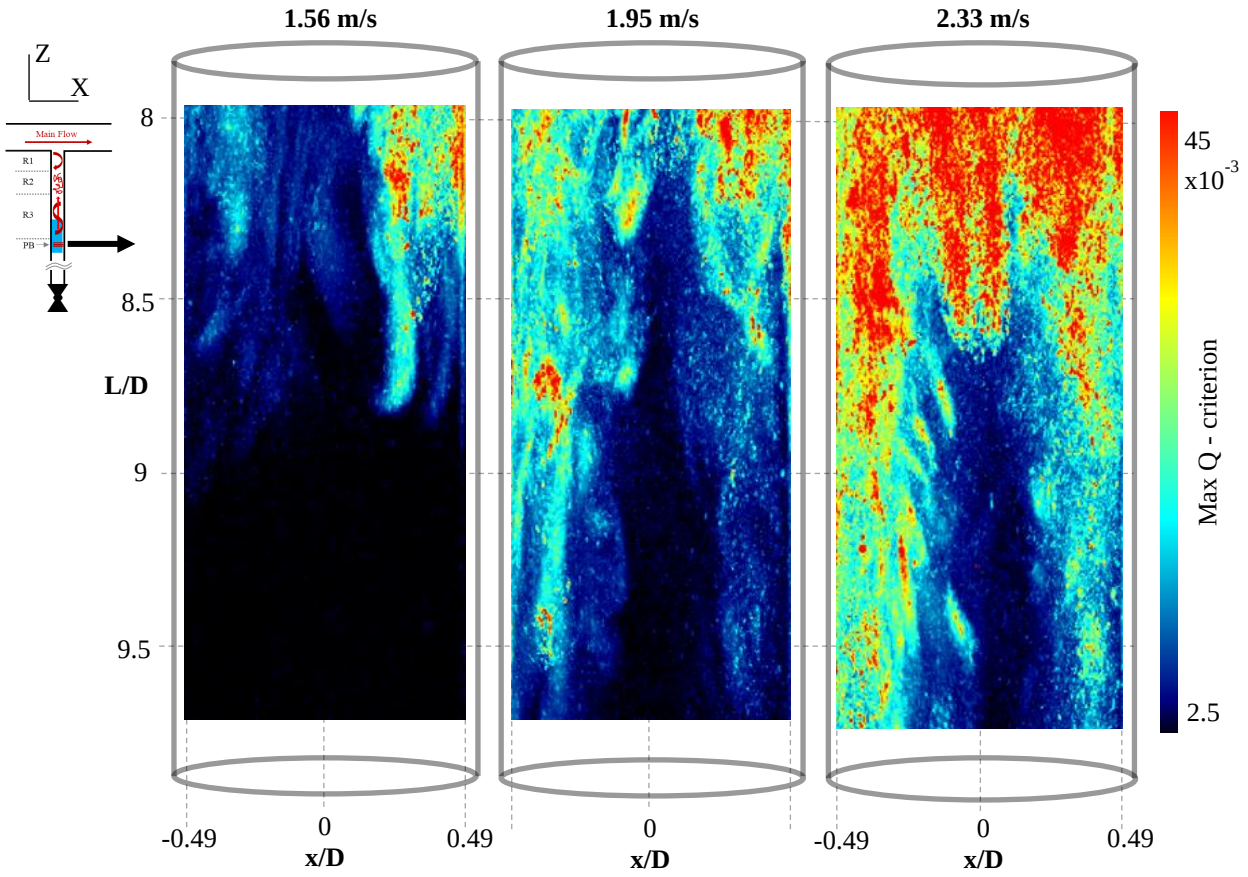

Figure 3-14 Maximum Q-Criterion value at any instant within the measurement at each location.

selected for analysis but rather the local maximum values at any given time in the measurement. This method yielded the energy dissipation fields in Figure 3-14, used for visualization of three velocity cases. The contrast for visualization and identification of the PB location is significant between this figure and their complimentary Vz fields (reference Figure 3-13).

The relationship between branch line flow penetration depth (the location of PB) and the main line flow rate is easily demonstrated in Figure 3-14. As the velocity of the main line flow is increased, the turbulent energy penetrates to greater L/D positions in the branch line. Part of what makes the Q-criterion visualization so striking is the fact that using secondary flow features, it effectively filters out some of the less energetic regions in the measurement field. As a result, values where the Q-criterion is very low is a strong indicator of where the flow is significantly

laminar or stagnant. A feature of the flow that the Q-criterion also brings to light is the final entrainment zone where the downward flow near the pipe walls is caught up in the flow at the center of the pipe returning towards the main line. This feature, where the vorticity is stronger near the walls than in the center, can be seen in the figure at the cross-sections of the 1.95 m/s case at L/D > 8.6. It appears from results that, with increasing main line velocity, this termination zone at the PB elongates. This is potentially a greater aspect of the penetration depth reached by the penetrating flow than the elongation of the preceding serpentine structure.

3.3 Rectangular Profile Loop Facility

Measurements in the Rectangular Profile Loop (RPL) were conducted using LDV methods to obtain tangential velocity data in the branch line and main line flow profiles. LDV measurements of the tangential velocity at various depths in the branch line were made to assess the presence of an axial swirl. As a reminder, this facility was built to investigate the effects on the branch line flow swirl when higher velocities are present in the main line flow. For comparison with the results obtained with the SSEF facility discussed in Section 3.4.3 and elsewhere, Re* is used to denote the normalized tangential velocity magnitude at each measurement location. Re* is effectively a local Reynolds number, comprised of fluid properties, the branch line diameter, and the local tangential velocity. Because the main line cross-section was not round, two flow profile measurements were made upstream of the branch line junction to account for the differences between the y and z axes.

3.3.1 Swirl Velocity Decay – RPL

As a means of informing the later implementation of T-PIV, LDV was used to measure the tangential velocity of the flow in the branch line. The intensity of the tangential velocity in the

branch line is a strong indicator of the swirl that develops in the flow. Tracking the tangential velocity in the RPL branch line between L/D = 2-12, yielded a trend with two distinct regions (Figure 3-15). The velocity trend preceding L/D = 5.5 was referred to as the oscillating region. For L/D ≥ 7, the trend of the flow swirl can be considered decaying. The onset of the decay portion of the trend may be sooner, but observation of the flow is obstructed by a flange. Measurements for L/D <2 were not initially made because the translation stage used had a track length of only 10 diameters and it was desirable to get data on both sides of the flange in a single measurement run.

The oscillation of the average velocity between L/D = 3.5-5.5 was not expected to have so little uncertainty. With the magnitude of velocity decreasing and then increasing slightly, it was expected that the uncertainty would be larger, manifesting the swirl's competition with other flow phenomena. For this reason, the measurement at a main line flow rate of 6.8 m/s was re-setup and repeated. The low degree of error was observed again, as shown in Figure 3-15. At each measurement point, about 10,000 counts were collected over about a two-minute period. By eye, this region looked more disturbed than measurements showed. It is unclear what this indicates about the flow, and merits further investigation.

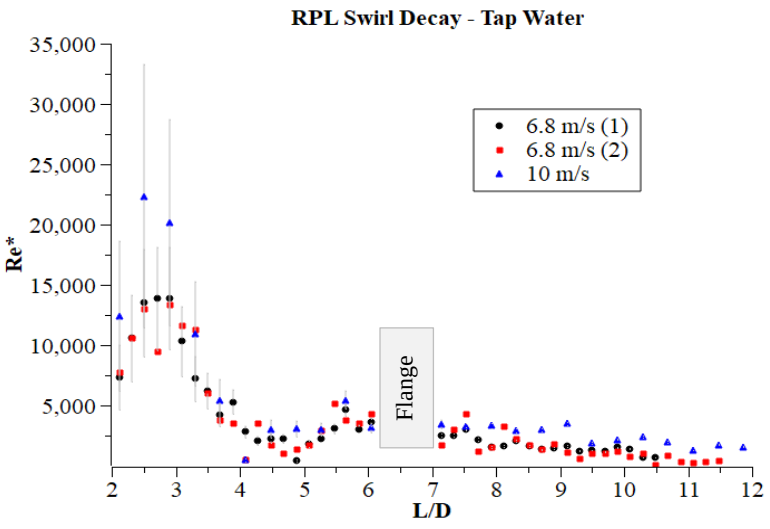

Figure 3-15 RPL branch line swirl decay measured via LDV

The decay portion of the collected velocities, L/D ≥ 7, exhibited flatter trends than expected based on SSEF results

(Section 3.4). The constants of proportionality of the respective exponential trendlines were between -0.33 and -0.19. It is unclear if this is the result of competing flow phenomena, which will take further measurements to determine. The discrepancy in the flow phenomena is possibly related to the opening geometry of the branch line (See Section 2.3.2).

3.3.2 Main Line Flow Profiles – RPL

Main line profiles were measured along center lines of the Y and Z axes of the RPL upstream of the branch line junction. The measurement line orientations are demonstrated in Figure 3-16. Each LDV measurement line was at the center of the channel in their respective orientation (i.e., the Y-axis measurement line was 7.5 mm from both parallel channel walls). The data gathered from the measurements was compared to the results of CFD predictions for the flow in the designed RPL channel.

The agreement of CFD predictions and the measurements of the flow profiles can be seen in Figure 3-17 RPL Z-axis main line flow profile for the 10 m/s case.and Figure 3-18 RPL Y-axis main line flow profile for the 10 m/s case.. In each plot, there is a gray box highlighting the part of the profile that would interact with the branch line opening. For the Y-axis, the portion of the profile 25.4 mm either side of center would pass over the opening. Although it would have been preferable to get a profile for the complete width of the channel, it was not feasible. Measurements at the far side of the channel to the LDV device (-50 mm)

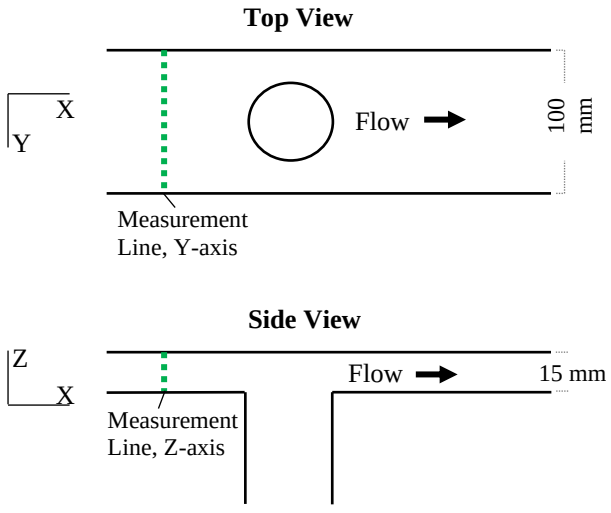

Figure 3-16 Main line profile measurement lines along two axes.

were difficult to get good statistics for due to the beams traveling through 100+ mm of acrylic and water. For the Z-axis, the flow's boundary layer would directly cross the opening. Measuring the profile closer to the wall for the Z-axis was prevented by the lack of optical clarity caused by the acrylic cement used in channel construction.

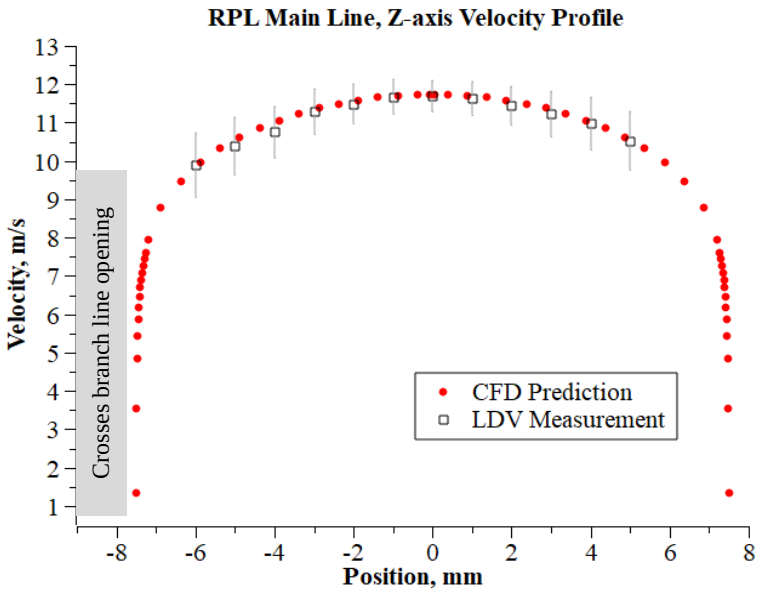

Figure 3-17 RPL Z-axis main line flow profile for the 10 m/s case.

Having main line flow profile information allows CFD efforts to proceed while branch line measurements are pending. Investigations of the effect of branch line opening geometry (sharp/rounded as discussed in Section 2.3.2) on branch line flow swirl development in the branch line may prove critical to experimental design decisions going forward. For example, preliminary simulations show that the flow is significantly altered within the $L/D \leq 3$ segment of the branch line when the branch line opening is changed from sharp to rounded.

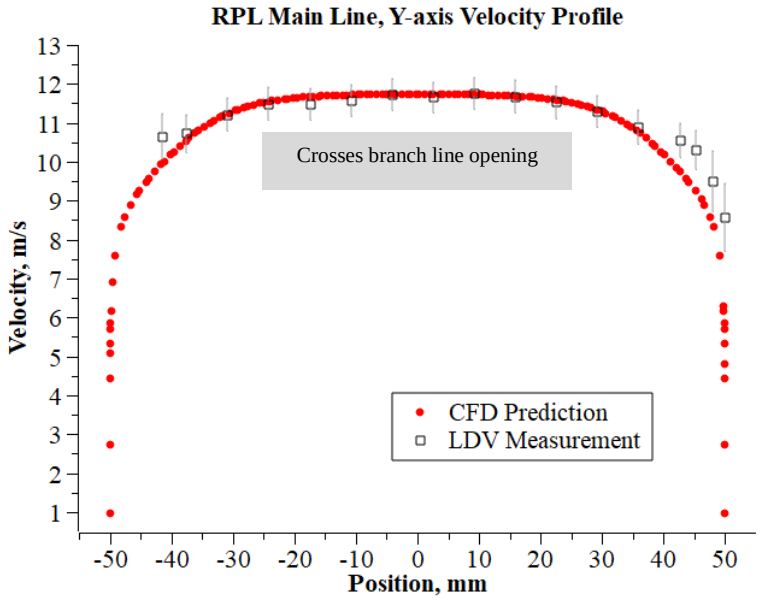

Figure 3-18 RPL Y-axis main line flow profile for the 10 m/s case.

3.4 Swirl Separate Effect Facility – SSEF

Measurements of the flow in the swirl separate effect facility (SSEF) were conducted using LDV and then T-PIV methods. The purpose of these measurements was to investigate the structure of the developed flow swirl in the branch line with well-defined boundary conditions, having the flow interaction of the main line and branch line fluids at the branch line opening eliminated. Making LDV measurements at various depths in the branch line, the tangential velocity of the swirl was tracked from the paddle tip to a point of dissipation. Measurements of the swirl's intensity were repeated for cases where the kinematic viscosity of the branch line fluid had been varied, to investigate scaling effects and be able to extrapolate the results to prototypical NPP coolant temperatures. After determining the swirl's tangential velocity trend, T-PIV measurements were made in three regions of interest in the branch line.

3.4.1 Swirl Tangential Velocity Studies – SSEF

Initial investigation into the characteristics of the swirl in the SSEF were conducted using the LDV for pointwise measurements at various depths in the branch line. Of particular interest was the tangential velocity of the swirl and how its intensity decayed further downstream of the swirler paddle. To capture the tangential component of the flow, the beams of the LDV were oriented on a horizontal plane, orthogonal to the branch line axis. The point of measurement in the fluid was held near 2 mm from the inner pipe wall. Per experimental run, measurements were gathered at various L/D depth positions in the branch line, where L was the linear distance and D was the pipe's inner diameter (Figure 3-19). Stirring rates

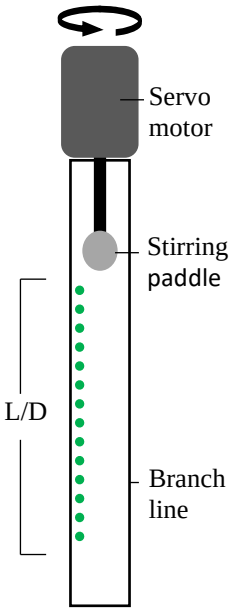

Figure 3-19 SSEF facility with measurement points referenced as different L/D distances from the paddle tip.

input to the servo motor of the system were held constant for the duration each measurement run.

The initial stirring rates investigated during the experimental campaign were determined using correlations provided by previous EPRI measurements [36]. According to the correlations, it is possible through stirring to generate a branch line swirl of a given intensity as would likewise be created by a given main line flow crossing the branch line opening. With a paddle diameter of 25.4 mm, initial stirring rates of 1500, 1300, 1000, and 700 rpm were determined to correspond with main line flow velocities of 14.1, 12.2, 9.4, and 6.6 m/s respectively. After initial measurements were made, cases with a stirring rate of 1500 rpm were excluded from the findings. At such a high rate of rotation, it was found that the paddle caused a vortex of entrained air to be drawn down around it as fluid was displaced. In turn, a stirring rate of 850 rpm was added to the principal rates for study.

Measurements in the SSEF were repeated using fluids with differing kinematic viscosities to simulate viscosity differences that would exist in thermally affected conditions and examine scaling effects; namely, the following fluids were used tap water, sugar solution, glycol solution, and brine. Liquids of different properties that could be selected for this study were restricted to those that were optically clear, non-corrosive, and non-flammable. This effectively restricted fluids with lower kinematic viscosities than that of tap water from this study. To account for the fluid property differences between cases, velocity measurements are shown as Re* values. Re* is effectively a local Reynolds number, comprised of fluid properties, the branch line diameter, and the local tangential velocity.

3.4.2 Tap Water Measurements – SSEF

Swirl velocity decay trends for the 850-1300 rpm cases exhibited three distinct features, as can be seen in Figure 3-20. Those regions will be referred to as the plateau (L/D < 2), the drop

(2 < L/D < 3), and an exponential decay region (L/D >3). The presence of these features in the decay trend were intriguing, as the plateau and the drop were not expected. Due to the coarseness of the related data presented in the EPRI reports, it was unclear how irregular the appearance was of these two features in the SSEF results.

To help rule out the possibility that reducing the diameter of the branch line had introduced the plateau and drop to the swirl's velocity trend, a larger diameter separate effect branch line was arranged. The larger diameter apparatus was adapted from an existing facility in the ECMF lab with a 101.6 mm acrylic tube. With the stirring rates that correspond to the diameter of the tube and the 50 mm diameter paddle used, the swirl trend measurements were repeated. The plateau and drop were present in those measurements as well.

Returning to the SSEF, various other partial measurements around 1.5 < L/D < 3 were conducted for selected paddle rpms to see if the drop was present in their respective swirl trends. For stirring rates above 800 rpm, the drop was clearly distinguishable. When stirring rates were 700 rpm and lower, the trend had no plateau or drop in the expected region. Between 700-800 rpm, the presence of the drop fluctuated, showing a transition from one swirl decay regime to another.

Full measurements for tap water cases where the stirring rate was below 700 rpm were not conducted by the time of this report. The primary reason for this was the fact that water cooled NPP main line flow rates are around 10 m/s. At the time, it was reasoned that going to stirring rates lower than

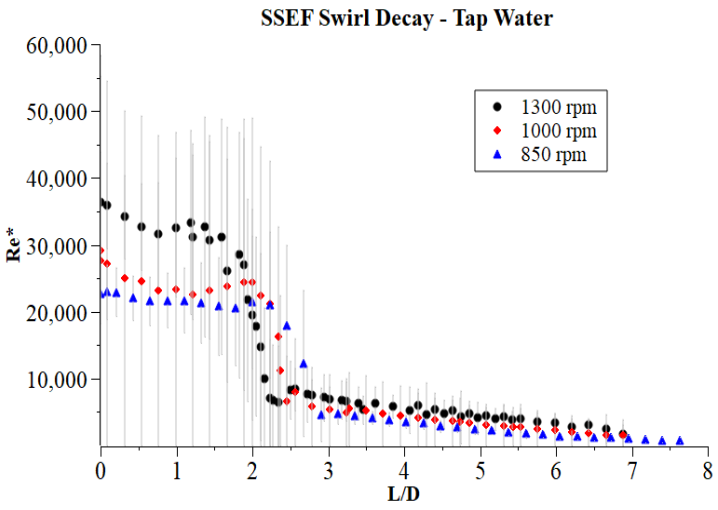

Figure 3-20 Swirl decay trend in SSEF for selected velocities.

700 rpm (and therefore lower correlated main line flow rates) would not yield the directly relatable data being pursued. Instead, measurements were then repeated for equivalent rates with fluids at different kinematic viscosities.

3.4.3 Fluids with Various Kinematic Viscosities – SSEF

Cases where the fluid in the SSEF was either sugar solution, glycol solution, or brine, exhibited the same trends as discussed in Section 3.4.2. Comparison with those tap water trends can be seen in Figure 3-21 for higher velocity cases and in Figure 3-22 for the 700 rpm cases. The stirring rates of the non-tap water cases are denoted in quotations to signify that they were stirred at different yet equivalent rates.

Determining different yet equivalent stirring rates was done to account for the differences in kinematic viscosity between the fluids (Table 3-3). As discussed in Section 3.4.1, the stirring speeds initially investigated were determined from EPRI findings that correlated them with main line flow rates. To preserve the correlation, the theoretical main line Reynolds number (Re-M) of each case was matched to that of the tap water case. For example, using the 850 rpm tap water main line velocity of 8.0 m/s, respective fluid properties, and an arbitrary main line diameter, a baseline Re-M can be calculated. Working backwards from this Re-M value, fluid properties of the glycol solution would yield an equivalent stirring rate of 1341 rpm.

Table 3-3 Properties of the fluids investigated in SSEF measurements.

Fluid at room temperature	Density (g/ml)	Dynamic Viscosity (cP)	Kinematic Viscosity (10^{-6} m^2/s)
Tap water	0.99	1	1.01
Brine	1.17	1.638	1.40
Glycol solution	0.93	1.487	1.60
Sugar solution	1.02	1.625	1.59

It was expected that accounting for the stirring rate equivalency and the Re* value at each L/D position in the branch line would yield similar trends to those found for tap water cases. The similarity shows that main line flow conditions are highly correlated to the intensity of the swirl created in the branch line. Therefore, branch line flow experiments conducted using tap water can be used to extrapolate the trends expected from cases of different fluid properties, like those expected in typical NPP conditions. For the present work, this is significant because the water flowing in NPP coolant lines is generally upwards of 300° C. Being able to conduct adiabatic studies for branch line flow conditions greatly reduces the complexity of the measurement process and facility requirements.

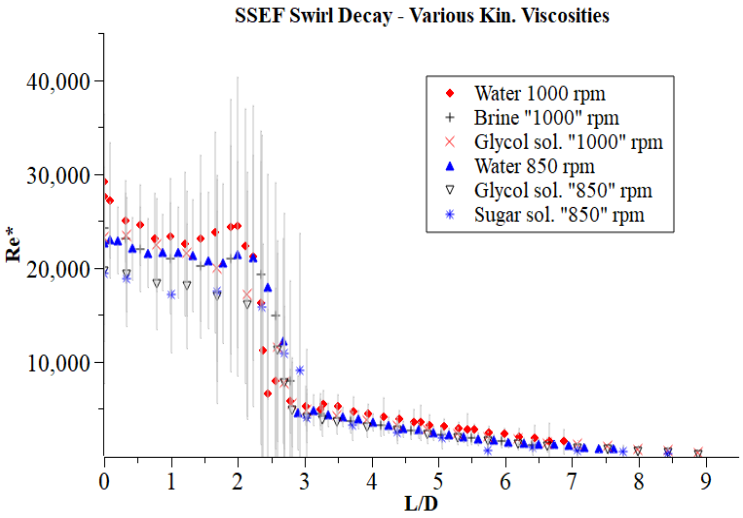

Figure 3-21 Swirl decay trends of various fluid cases compared to tap water results.

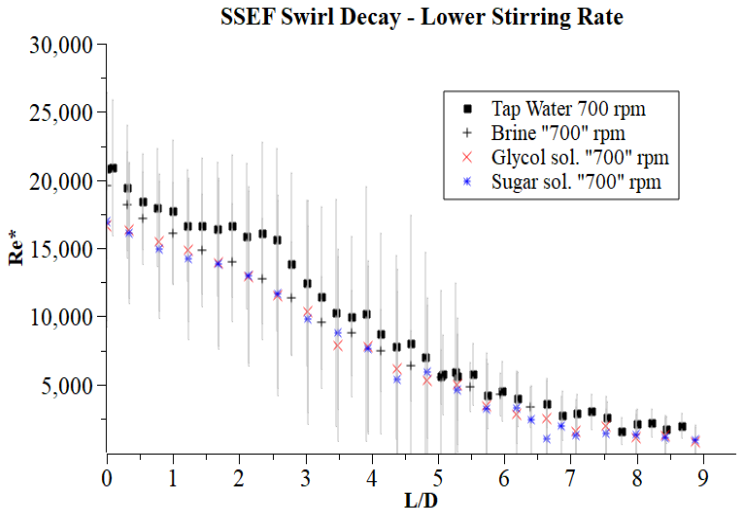

Figure 3-22 Swirl decay trends of various fluid cases compared to 700 rpm tap water results.

3.4.4 Making Sense of the Plateau and Drop – SSEF

As discussed in the previous two sections, for higher stirring rates the tangential velocity of the swirl in the branch line exhibited three distinct features: the plateau (L/D < 2), the drop (2

< L/D < 3), and an exponential decay region (L/D >3). Investigating why this was the case led to comparative measurements in a larger diameter branch line and extra review of the available EPRI reports. It appears that the presence of the plateau and drop features were the result of the facility design.

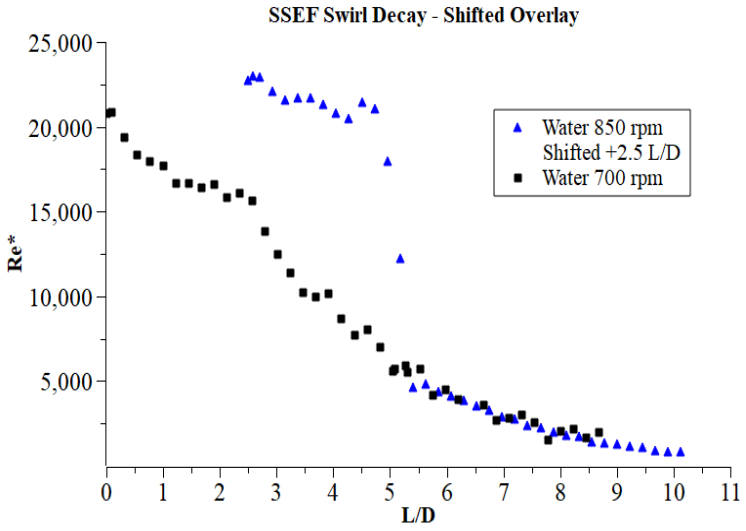

Figure 3-23 Overlayed data from two different tap water measurements. Results of one plot are shifted to show the early onset of the exponential decay in high rpm cases.

The design of the SSEF differed from the EPRI separate effect facility in that the paddle was spun in the branch line, instead of in a basin at the mouth of the branch line. The EPRI design employed a large diameter basin at the top of the branch line where the paddle was inserted. With the paddle in the large diameter basin, the radial fluid displacement of the paddle did not significantly affect the swirl that entered the branch line. In the SSEF design, this displacement caused additional flow turbulence about the paddle because of flow interactions with the nearby walls. The additional flow complexity effectively created a cylinder of rotating fluid that comprised the plateau region. This cylinder, although not a solid object, acted as a stirring mechanism shearing the fluid below. For this reason, the swirl's velocity dropped sharply around L/D = 2.

Although the presence of the plateau and drop were undesirable for the results of this investigation, the data gathered overall was still very useful. Analysis of the data showed that the exponential decay region of the 850+ rpm stirring cases was similar in trend to the 700 rpm cases. The similarity can be seen in Figure 3-23, where an 850 rpm case is shifted to the right to overlay

the decay region of the 700 rpm case. The need to shift the data for overlay exemplifies the early onset of the decay region caused by the turbulent flow of the plateau region. Trendlines of the decay region of all the cases fit with a decay constant of proportionality from -0.5 to -0.36 in magnitude. Accounting for the L/D shift, the decay trend data from the cases collected can still be used to predict swirl decay in branch lines. Trends with the plateau and drop also provided more interesting data for CFD analysis once the flow was measured using T-PIV. Without the drop, T-PIV would have only been used to measure at a location in the decay of the swirl and at the extent of the swirl. Because the drop was present, it was measured with T-PIV to provide special data for CFD validation. As will be discussed in Section 4.1, CFD RANS models struggle to accurately predict and model abrupt flow transitions like the drop.

3.4.5 T-PIV Measurements – SSEF

Flow measurements of tap water stirred at 850 rpm were collected using T-PIV in three different regions. These locations were selected for T-PIV investigation based on the results of the swirl decay trend data gathered previously (Section 3.4.2). The first region, closest to the stirring paddle, includes the drop trend discussed previously. The second region of interest included the exponential decay region of the swirl decay trend. The third region was of the extent of swirl penetration, referred to as the penetration boundary. Although data was gathered for all three velocity components, it is difficult to represent the 3D data in a 2D document such as this. For discussion of results, the most relevant components will be used, and the most straightforward presentation selected.

3.4.5.1 The Drop Region – SSEF

For the measurement region of $1.28 \leq L/D \leq 3.30$ of the SSEF test section, the flow structures of the plateau and the drop identified in Section 3.4.2 were captured in T-PIV results.Figure 3-24, shows the average fields of two flow components in the central plane of the branch line. Within the figure, there are overlain white arrows to highlight flow directions. For the vertical flow component, Vz, the central flow in the branch line trended towards the paddle and the flow near the walls trended away. The Vy component, which in the center plane represented is effectively the tangential velocity of the swirl, is going into the page plane on the right side and coming out on the left. The transition of intensity in both velocity field trends around L/D = 2.29

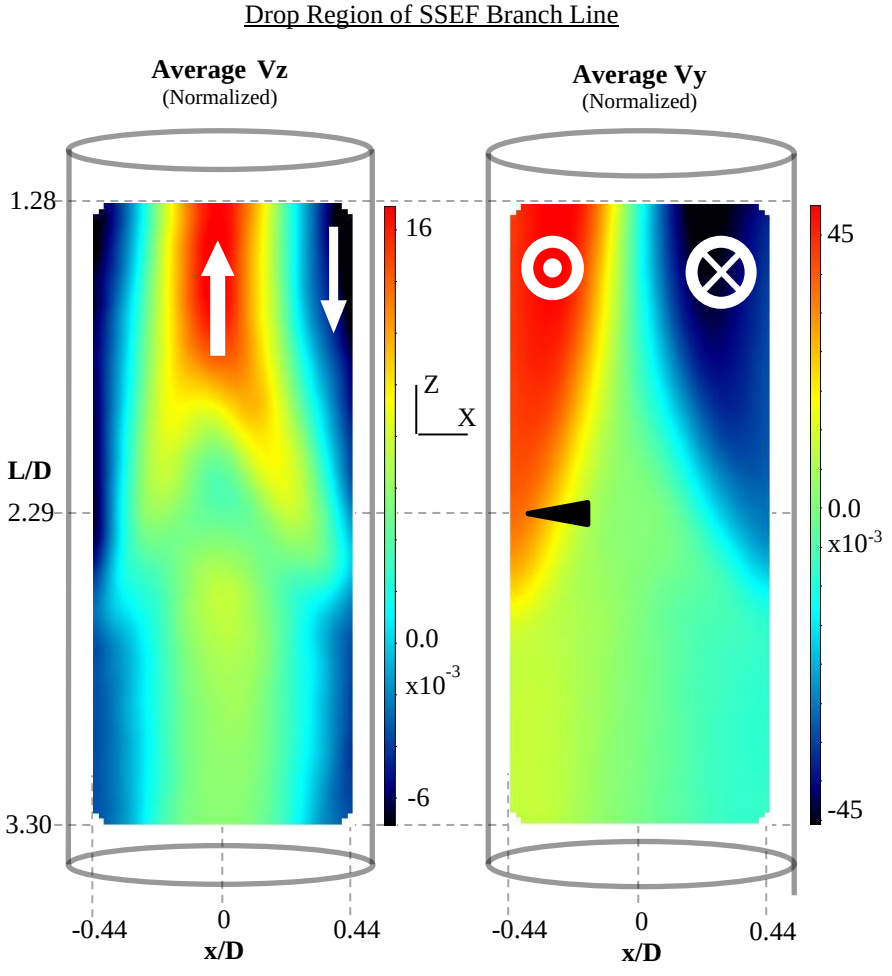

Figure 3-24 T-PIV measurement of the upper region of the SSEF where the drop in swirl velocity was present.

highlight the presence of the velocity drop that separates the plateau from the exponential decay region.

Extracting average velocities along a z-line from the T-PIV data, the presence of the plateau and drop trend can be compared with the previous LDV data (Figure 3-25). The magnitude disparity between the two trends for the plateau region is partially due to the difference in measurement location. The T-PIV measurement volume of interest did not capture the flow within 2 mm of the wall as was the case for the LDV measurements. This is due to the physical limits of placing a 3D calibration target in the pipe. Although T-PIV measurements captured data 2.5 mm from the wall, this data is not inherently as accurate as the central portion of the field. The drop in accuracy is due to the fact that the edges of the measurement volume are where previously uncaptured particles enter the measurement volume. Frame-to-frame analysis of the particles captured in this case yields poorer correlation, thus lower accuracy.

The persistence of the plateau region of the flow is evidently supported by the strength of a circulating vortex. The stirring and displacement of the paddle in the branch line formed a vortex that spiraled about the branch line axis. The spiraling of the vortex is readily evident in 3D representations of the flow and it can be visualized in the 2D

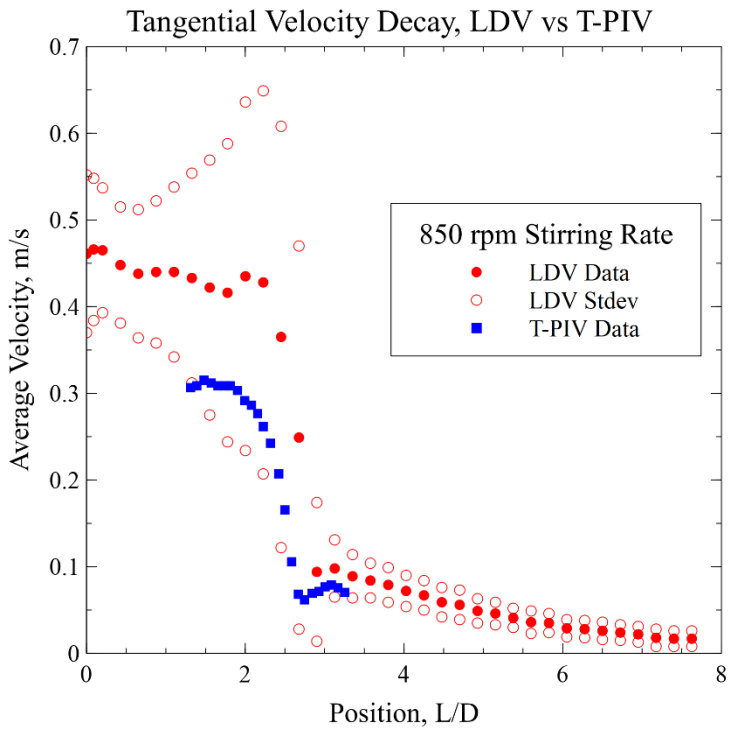

Figure 3-25 Comparison between the Tangential Velocity Trends Extracted from the SSEF Swirl Measurements Made Using LDV and T-PIV Techniques.

fields presented. First, consider the average Vz field where the upward flow is forked. The fork shows how the center of the vortex where the upward flow is strongest, revolved about the branch line axis as it came in and out of the central plane. Second, notice the central portion of the Vy component field, where the average magnitude is nearer to zero, widens past L/D ~ 1.8. Although the widening may appear to be a drop in velocity, it is actually the product of averaging an oscillating velocity field. As the tail of the initial vortex revolved, it would raise and lower the velocity in that region cyclically. Even the regions with a higher average velocity experienced cyclical oscillation. At the location in the Vy velocity field marked with a black arrow, the peak velocity was observed at a rate of 3Hz (Figure 3-26).

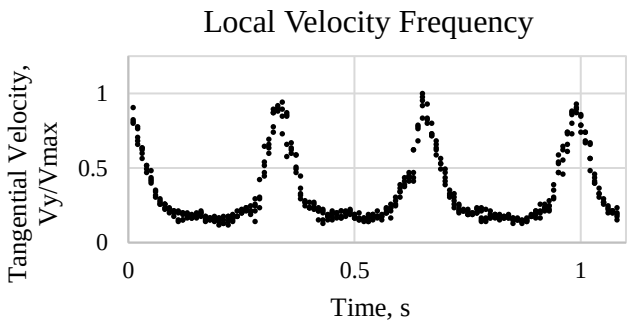

Figure 3-26 Local Velocity Fluctuation, location denoted in Figure 3-24 T-PIV measurement of the upper region of the SSEF where the drop in swirl velocity was present. with black arrow.

As proposed in Section 3.4.4, T-PIV measurements also suggest that the swirl in the exponential decay portion of the overall trend is not directly driven by the paddle itself. It is clear the initial vortex created by the paddle does not persist beyond the drop region. Instead, the fluid of the tail end of that vortex shears the fluid below as it spirals about the branch line axis. The displaced fluid about the paddle interacting with the surrounding walls no doubt led to the irregular vortex behavior. This is more evident when considering the swirl structure observed in measurements of the exponential decay region (Section 3.4.2). Nevertheless, as it will be demonstrated in section 3.5.1, the swirl decay measured in the SSEF facility is also representative of the behavior to be expected in cases where the branch line swirl is driven by the flow in the main line. Therefore, the SSEF data can be used to characterize the flow decay in typical NPPs branch lines.

3.4.5.2 The Exponential Decay Region – SSEF

For the measurement region of $3.52 \leq L/D \leq 5.62$ of the SSEF, T-PIV results showed a stable, decaying swirl that persisted as expected. This flow behavior can be seen in Figure 3-27, where the average velocity of two flow components in the central plane of the branch line are shown. Within the figure, there are overlain white arrows to highlight flow directions. For the vertical flow component, Vz, the central flow in the branch line trended towards the paddle and the flow near the walls trended away. The Vy component, which in the center plane represented is effectively the tangential velocity of the swirl, is going into the page on the right side and coming out on the left. The swirl's tangential velocity can be seen decreasing in average intensity at increasing L/D values.

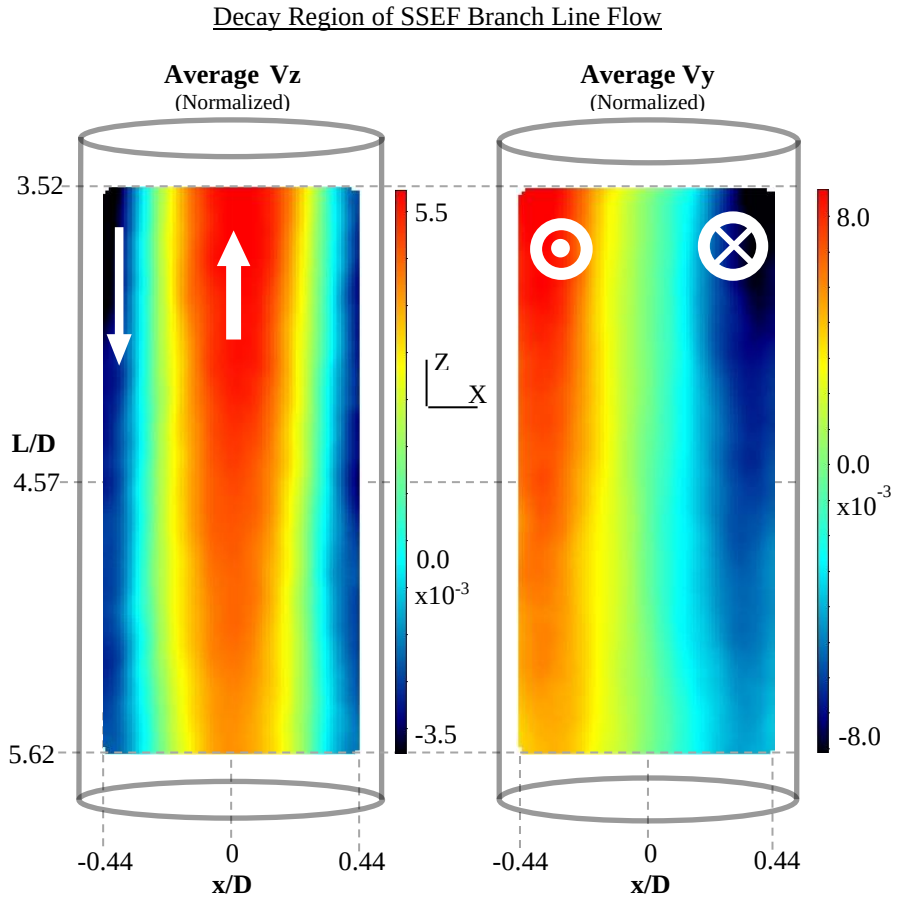

Figure 3-27 Decay region T-PIV results.

The upward central flow and the downward outer flow combined with the rotation of the swirl in this region confirmed the EPRI assessment of the present vortex. EPRI had previously determined the vortex in the branch line to have a double helix nature as illustrated in Figure 3-28. T-PIV results show that the helical aspect is less pronounced than shown in that rendering, but the measurement field was too narrow to see if the central flow coils to interact with the walls of the pipe or not.

Figure 3-28 EPRI representation of double helix like flow in the branch line where both upward and downward flow are entrained in the same swirl.

3.4.5.3 The Penetration Boundary – SSEF

For the measurement region of $9.26 \leq L/D \leq 11.06$ of the SSEF, T-PIV results showed the swirl terminate as downward flow was entrained into the upward flow. This flow behavior can be seen in Figure 3-29 where the average fields of two velocity components in the central plane of the branch line are shown. Within the figure, there are overlain white arrows to highlight flow directions. For the vertical flow component, Vz, the central flow in the branch line trended towards the paddle and the flow near the walls trended away. There is U-turn arrow highlighting a multicomponent flow that is not well represented with a single component illustration. The Vy component, which in the center plane represented is effectively the tangential velocity of the swirl,

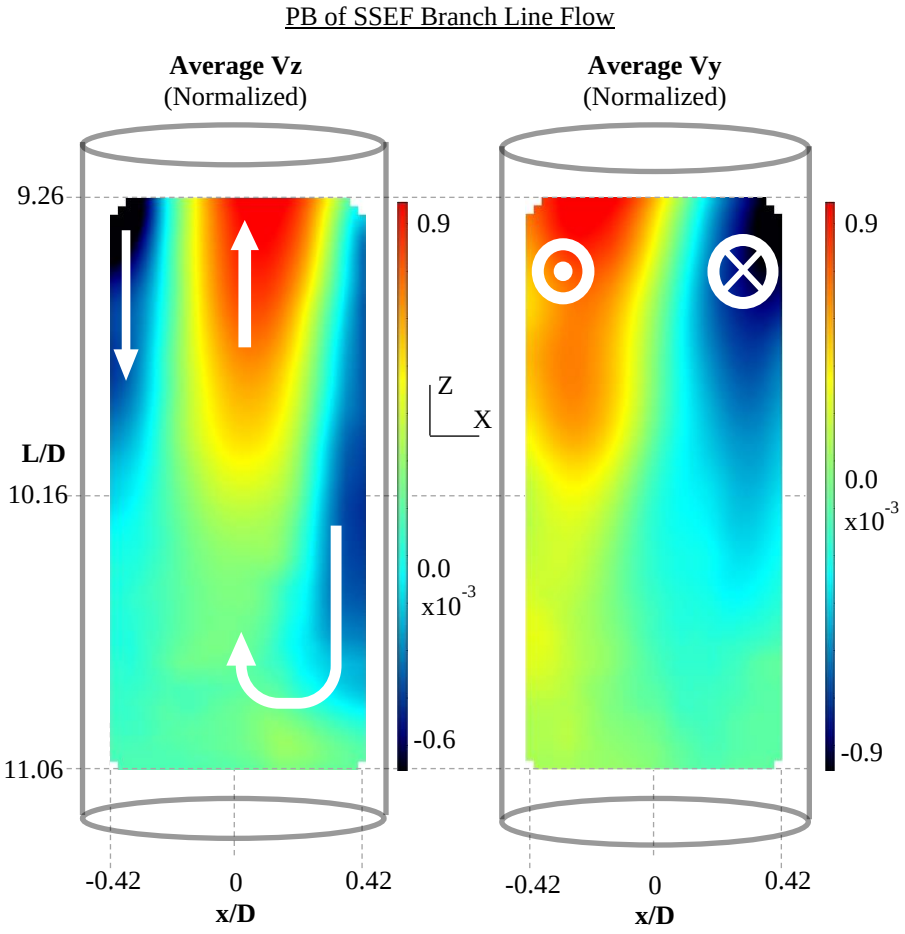

Figure 3-29 Swirl decay reaching the penetration boundary in the SSEF when swirled at 850 rpm

is going into the page plane on the right side and coming out on the left. The swirl's tangential velocity can be seen decreasing in average intensity at increasing L/D values.

Until the point of the swirl's penetration in the branch line, the tangential component of the flow is dominant. At the extent of the swirl's penetration, the magnitudes of the vertical and tangential flow components reach parity. The similarity in energy between the two components allows the downward flow near the pipe walls to be more easily entrained in the central upward flow. There is a degree of mixing between the two streams that occurs naturally as the upward and downward flows interact, but it is the most distinct at this point in the flow.

Even with a constant stirring rate, the fluctuations of the turbulent flow made defining a crisp horizontal penetration boundary difficult. Contributing to the difficulty was the fact that measuring velocity values nearing zero is a hurdle for mechanical and optical sensing systems. The optical method of T-PIV had the benefit of not obstructing the weakening flow, but it is still limited by its dependance on particle movement between frames. As a result, measurement of the flow L/D > 10.5 had more erroneous vectors and weaker overall correlation in instantaneous vector fields.

3.5 High-Capacity Loop Facility

Previous research determined that there are three distinct regions of interest in determining the flow development in reactor emergency coolant branch lines (Section 1.2). Figure 3-30 demonstrates the locations of these regions relative to their position in the branch line. As mentioned previously, the first region (R1) is believed to be dominated by a cavity-like flow structure, the second region (R2) exhibits an unclear transition from the cavity-like flow structure to the swirl that persists into the branch line, and the third region (R3) contains a vortex like flow, rotating about the branch line axis until reaching the penetration boundary (PB). Measurements

conducted on the ReBL-TF loop (Section 3.2.2) determined that the distinct features of R1 and R2 may not be significant over longer time periods, as their average characteristics trend towards the vortex like flow seen in R3.

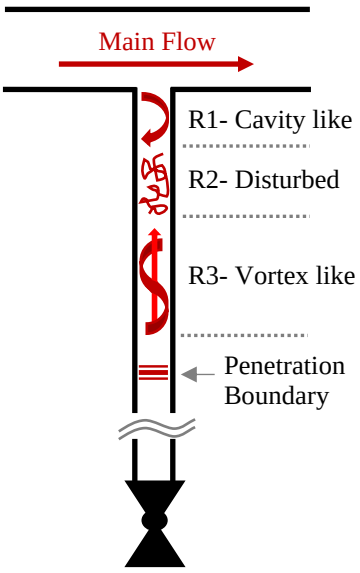

Figure 3-30 Representation of the regions of interest in the branch line.

Measurements in the regions of interest were conducted using T-PIV and LDV techniques. Measurement locations were selected for T-PIV measurement based initially on the findings of [21] so that the perceived flow behaviors of each region could be quantified. LDV measurements were made to track the flow swirl trend as done in Section 3.4.1. LDV was also used to verify the results captured using T-PIV as needed. Locations of measurements are referenced using L/D values, where L is a distance into the branch line from the opening and D is the branch line diameter.

3.5.1 Branch Line Swirl Tangential Velocity – HCL

Initial investigation into the characteristics of the flow in the HCL were conducted using the LDV for pointwise measurements at various depths in the branch line. Of particular interest was the tangential velocity of the swirl and how its intensity decayed further from the main line. To capture the tangential component of the flow, the beams of the LDV were oriented on a horizontal plane, orthogonal to the branch line axis. The point of measurement was held near 2 mm inside the pipe wall. Per experimental run, measurements were gathered at various L/D depth positions in the branch line.

As swirl trend measurements were collected at different velocities, an inflection point became apparent near L/D = 4. Before this point, as can be seen in Figure 3-31, the tangential velocity trends contained the greatest fluctuation and the greatest degree of difference in average velocity. The arc-like feature of the average velocity trends at L/D < 4 positions likely betrays a feature of the flow's initial development in the branch line flow; however, this velocity dependent difference does not appear to affect the swirl decay trend beyond that point. The agreement between the trends in Figure 3-32 where L/D > 4.3 can be used to predict the decay trend of a flow swirl in the branch line. Investigation at lower L/D values was desired to further define the swirl's initial development, but this was prevented by a flange at the connection to the

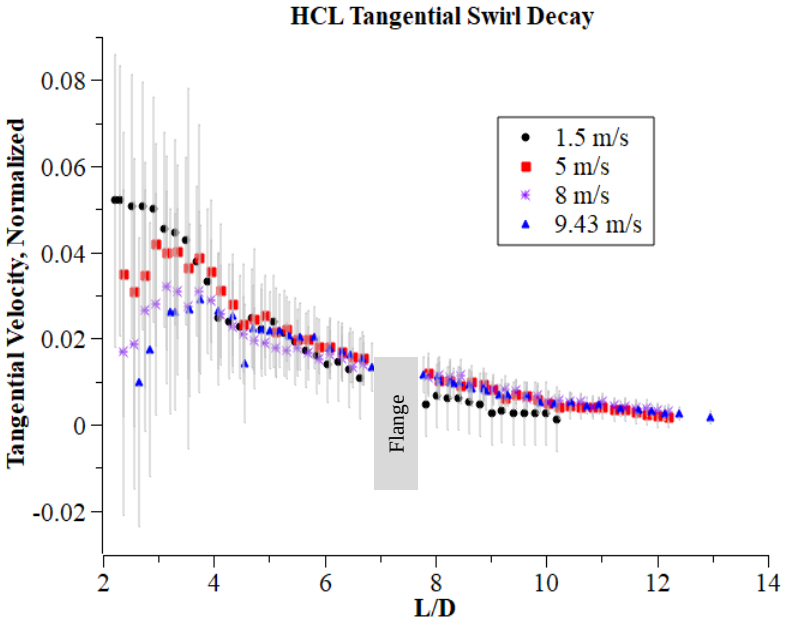

Figure 3-31 Tangential swirl decay in the branch line of the HCL at selected velocities.

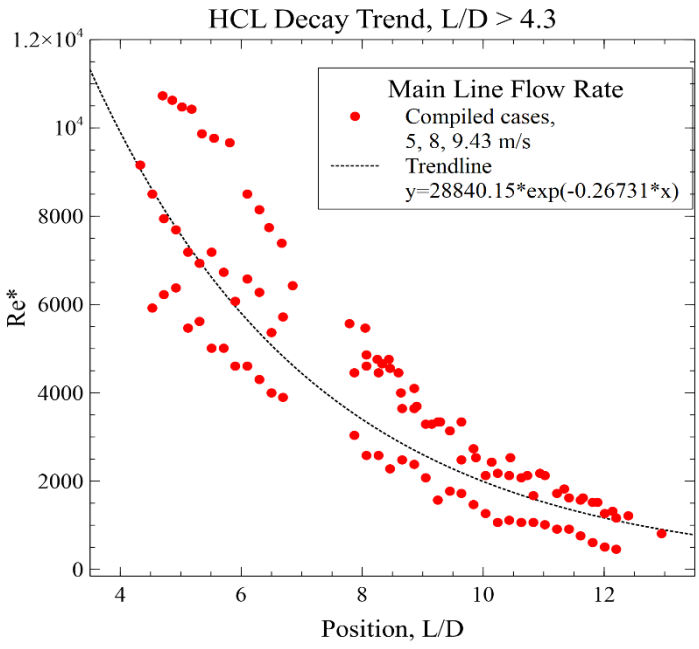

Figure 3-32 Decay trend of branch line swirl flow in HCL

main line. The flange about 7 L/D does not appear to have obstructed any deviations from the preceding trend so measurements were not repeated with a different piping arrangement.

The swirl's tangential velocity decay when compared with those gathered from the SSEF studies in Section 3.4.1 showed strong agreement. Figure 3-33 shows the agreement between selected trends – note that the SSEF trends are both shifted to the right by the given L/D amounts shown in the legend. This shift in position is necessary to compare the curves because of the difference in how L/D = 0 was defined and how the swirl was generated. As discussed in 3.4.4, the 1000 rpm case required a larger shift as the high-speed rotation caused an early onset to the decay portion of the trend when compared to lower velocity cases. The agreement in the swirl's behavior between the two facilities provides evidence that the paddle generated swirl of the SSEF studies may be sufficient to replace the HCL generated swirl for downstream branch line experiments. Such experiments would include investigations into how the swirl interacts or terminates in elbow or tee geometry piping, for example.

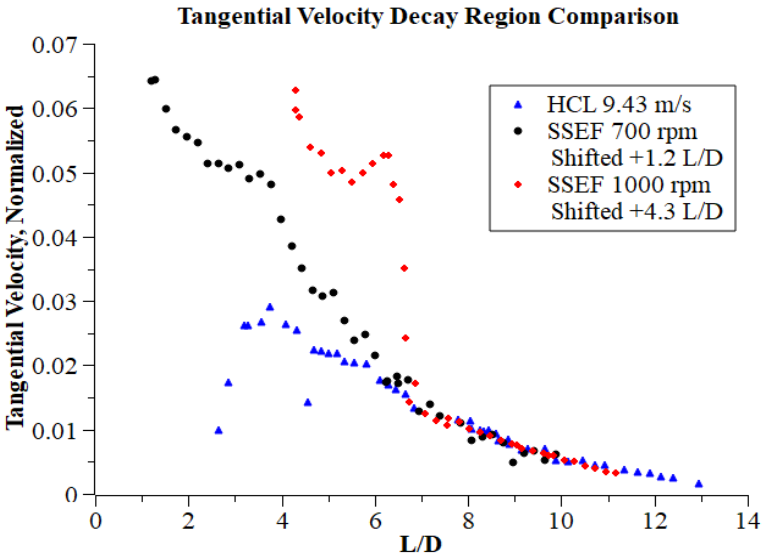

Figure 3-33 Comparison of swirl tangential decays in the HCL and SSEF experiments.

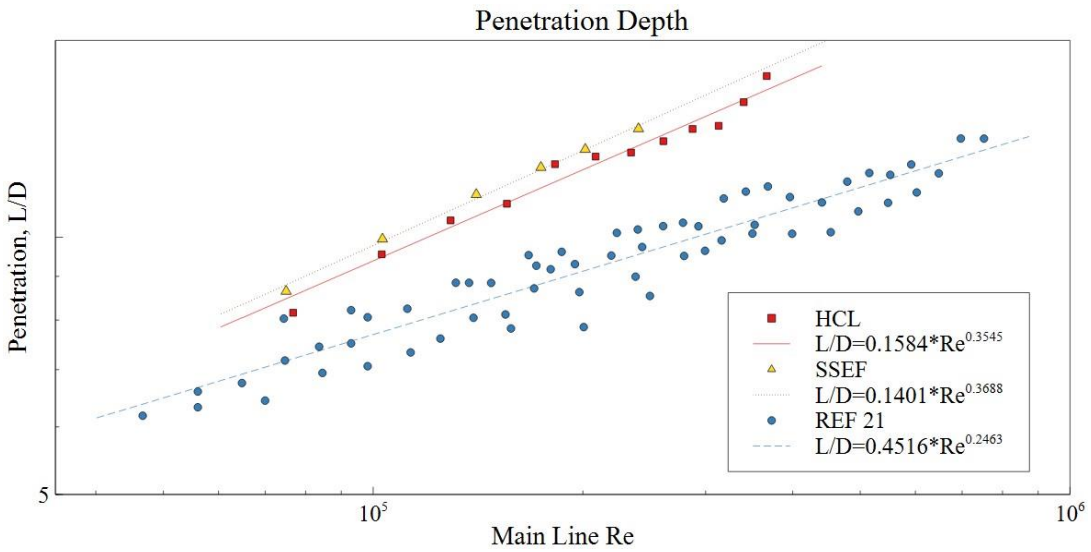

Figure 3-34 Penetration boundary assessed visually for HCL, SSEF, and Ref [21]

In determining the penetration boundary (PB) of the branch line swirl, LDV measurement was not suitable for low velocity flows, as the count rates are in turn extremely low. However, the PB could be identified using high-speed videos of tracer particles in the flow. The positional uncertainty of this method was estimated to be within ±5 mm. Using this approach, the PB was determined from both the HCL and SSEF and then compared with the results presented in reference [21].

The disparity between the data collected for this dissertation and that of reference [21] is likely due to the geometric difference between the setups and/or the visualization particles used. The 10μm diameter glass spheres used in this work are neutrally buoyant and yield a Stokes number less than 0.1 for the entirety of the measurement domain. There is not enough information to calculate the same from [21], but it is clear from the images in the paper that the polystyrene tracer particles used were significantly larger. That aside, the rectangular main line of the [21] facility may have an effect on the flow in the branch line that cannot be ignored. The narrowness of the channel was a concern raised previously when designing the comparable RPL (Section 2.3.2).

The comparison between the PB found for the HCL and that of the SSEF cases were closely aligned, as can be seen in Figure 3-34 Penetration boundary assessed visually for HCL, SSEF, and Ref [21]. Similar penetration trends between a flow driven branch line swirl and that of a paddle driven branch line swirl is evidence that a setup like the SSEF will be sufficient for future experimental campaigns investigating swirl penetration into piping geometries such as elbows. The similarity observed in HCL and SSEF penetration trends casts further doubt on the experimental setup in [21], which shows the importance of revisiting the findings with a facility like the RPL.

3.5.2 T-PIV 3D Velocity Field Measurements – HCL

3.5.2.1 R1 – HCL

Measurements of R1 ($0 \leq L/D \leq 3$) were not achieved at this point because of instrumentation setup limitations. As addressed in 2.2.3, when a measurement was being made through the round surface of the piping, a refractive index matching fluid prism was utilized. Due to the large viewing angle of the cameras (See Figure 2-9, Linear), the top of the corrective prism obstructed the view of the topmost camera when trying to capture the $L/D < 3$ segment of the flow. To obtain measurements of R1 in future HCL campaigns, it will be necessary to employ the cross formation for the cameras. Currently the lab is not equipped with the appropriate mounting frame to achieve this.

3.5.2.2 R2 – HCL

The R2 region as proposed by [21] spans about $3 \leq L/D \leq 7$, for main line flow rates near 10 m/s. T-PIV measurements were made in that segment of the flow, yielding the results in Figure 3-35. These center plane velocity fields show that the average flow resembles the vortex like flow

observed in previous measurements of R2 and R3 (Section 3.2.2). In the case of these 3D field measurements however, the vortex structure was not just interpreted from Vy revolving the flow about the branch line axis and Vz transporting fluid upward near the core of the pipe. The 3D fields clearly revealed the time resolved flow structures of the vortex. An example of the flow captured is in the instantaneous flow representation of Figure 3-36. Vector arrows illustrate the magnitude flow component as the color fields of the nine slices show the Vz aspect of the flow.

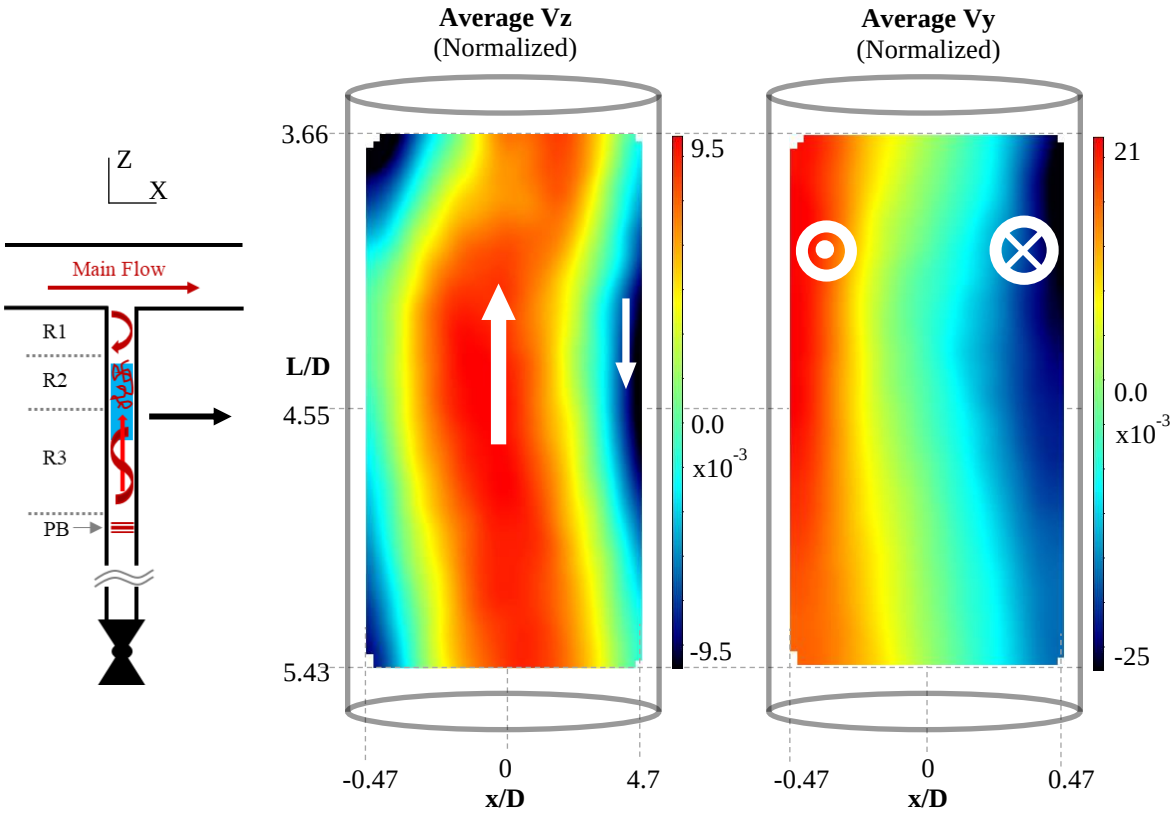

Figure 3-35 Composite average of results from three separate measurements taken in the R2 portion of the branch line.

Although the R2 portion of the branch line flow is very chaotic on a short time scale, which is readily seen by eye, the average vortex flow structure can be deduced from less than 2 seconds of time resolved measurement data. In the case of these measurements, velocity fields were captured at a rate of 2.3 kHz for 2.66 seconds each. As each data set was processed, a very similar

dominant average structure emerged. Figure 3-35 is actually a composite of three separate measurements at the same main line flow rate, which varies little from the individual measurement results. Given the measurement acquisition process (measure, assess particle images captured, save data, re-measure, etc.), each of these measurements were gathered at random times during main line steady running conditions. It was expected that there would be a higher degree of variation among the results of each gathered set, reflecting different snippets a cyclic evolution in this "disturbed" region. Longer measurement times may have revealed longer term evolutions in the flow's characteristics, but they were not possible with the 12 GB limit of camera memory.

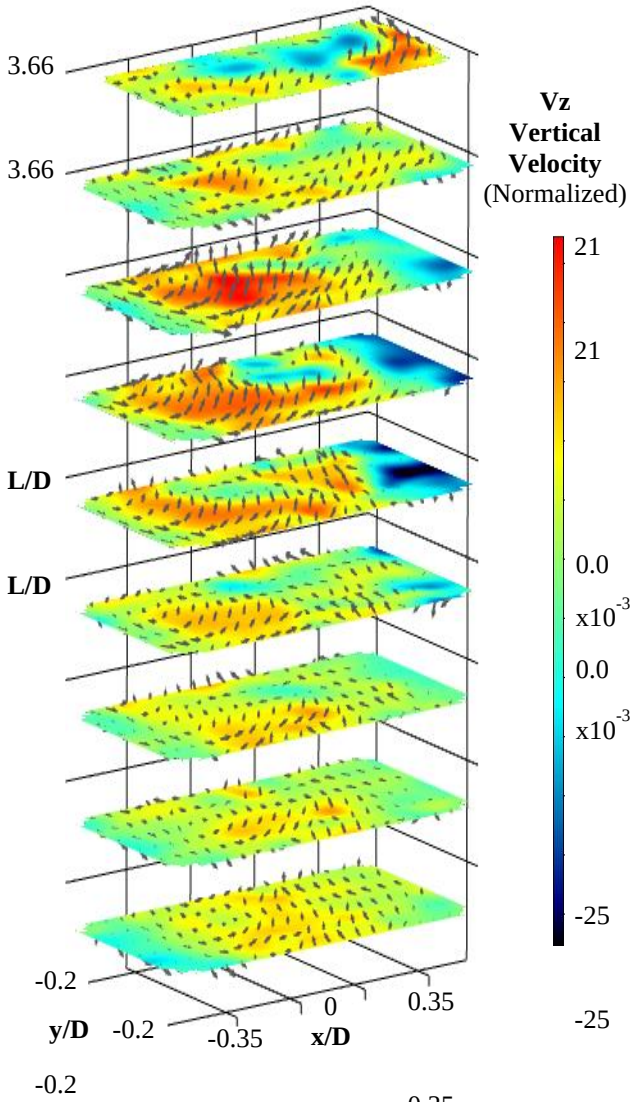

Figure 3-36 Instantaneous velocity field of 3D measurement. Component of the average velocities provided in the previous figure. Colored y-x planes how Vz flow magnitudes in each cross-section, vector arrows show velocity magnitude.

Aside from the confirmation that the average flow in the R2 portion of the branch line was vortex like, the most significant revelation was the magnitude difference between the components of the flow. As can be seen in Figure 3-35, the max/min magnitudes between the swirling and vertical components are significant. This was expected, given the swirl's persistence further into

the branch line, but the two components had never been simultaneously quantified before. This provides critical information that will aid in validating CFD models for isolated branch line flows.

3.5.2.3 R3 – HCL

The results of Ref. [21] showed that the R3 flow segment of the branch line could be expected to end near 10 L/D downstream of the branch line inlet at main line flow velocities near 10 m/s. By eye, it was clear that the penetration lasted longer than that in the HCL branch line (near 15 L/D as discussed in Section 3.5.2.4). T-PIV measurements of R3 were made about the 10.5 L/D position. The average, center plane results of one measurement are shown in Figure 3-37 for discussion.

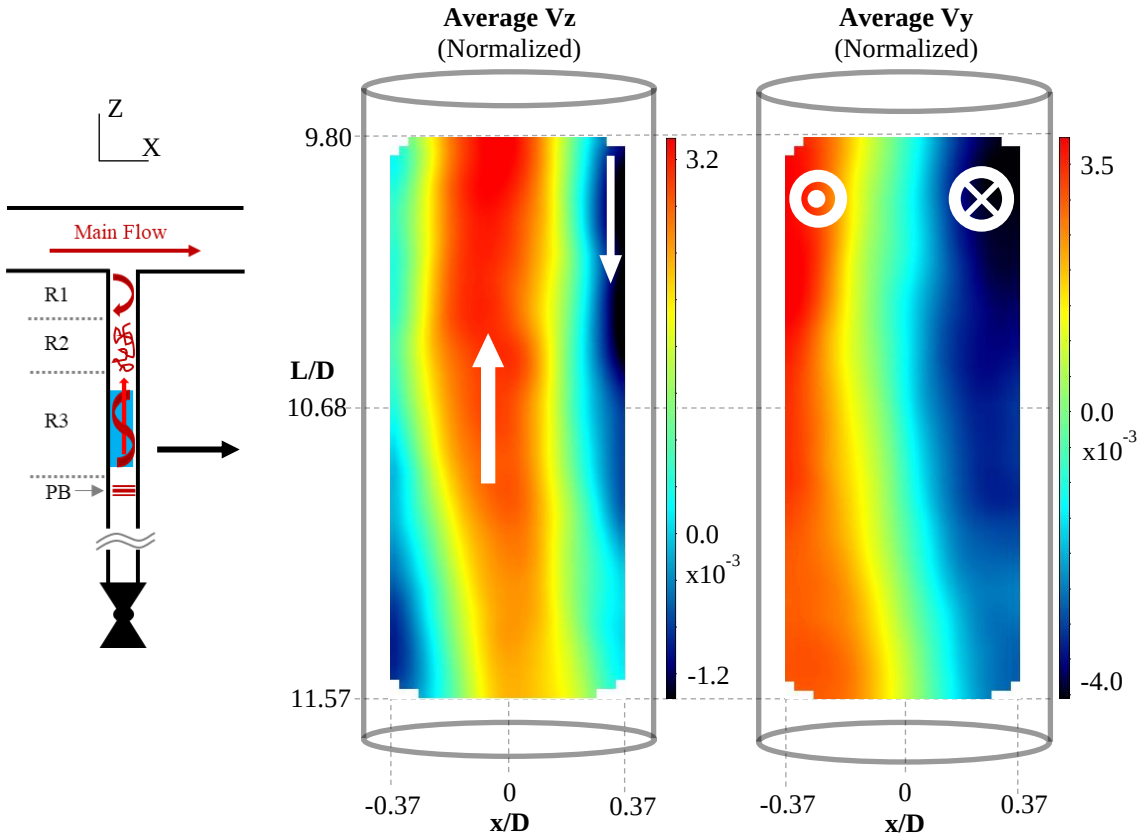

Figure 3-37 Average velocity fields in R3.

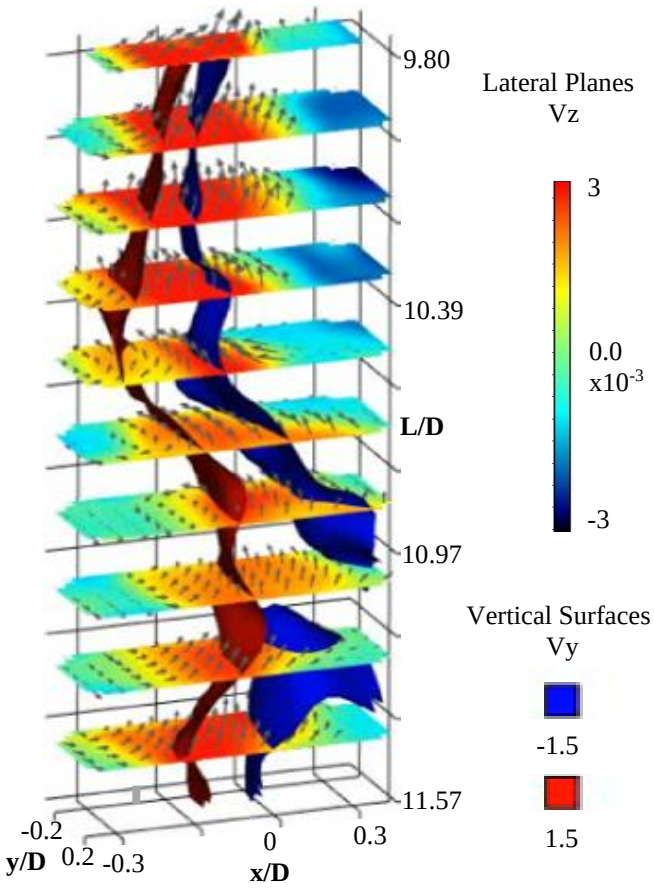

Figure 3-38 Instantaneous velocity field of 3D measurement in R3. Component of the average velocities provided in the previous figure.

As expected, R3 measurements revealed the vortex flow previously observed. Unlike the average vortex flow in R2, the tangential velocity and the axial velocity max/min magnitudes are more proportional. The instantaneous features of the flow are also less chaotic. As can be seen in the iso-velocity surfaces highlighted in Figure 3-38 (red, blue – vertical surfaces), the central rotating feature of the vortex is rather congruous axially. The vortex in this portion of the branch line's flow still experiences fluctuations caused by competing minor vortices, but they are not of the magnitude or frequency observed in R2.

3.5.2.4 Penetration Boundary – HCL

Through the optically clear glass of the HCL branch line, the penetration boundary (PB) can be observed by eye as the branch line's flow begins to stagnate. During previous measurement runs, the PB was determined to be near 15 L/D for main line velocities near 10 m/s. Measurements of the branch line about that position are reported in Figure 3-39. The termination of the vortex flow from the previous section of the piping (R3) is apparent in the measurements of the PB. Center planes of the measurement presented in Figure 3-39 show how the axial swirl dissipated and distorted at the extent of its penetration. For the tangential velocity feature of the flow (Vy), the core of the swirl appeared to curl as it approached 16 L/D. The vertical component of the flow petered out in the same region where the downward flow can be seen returning towards the main

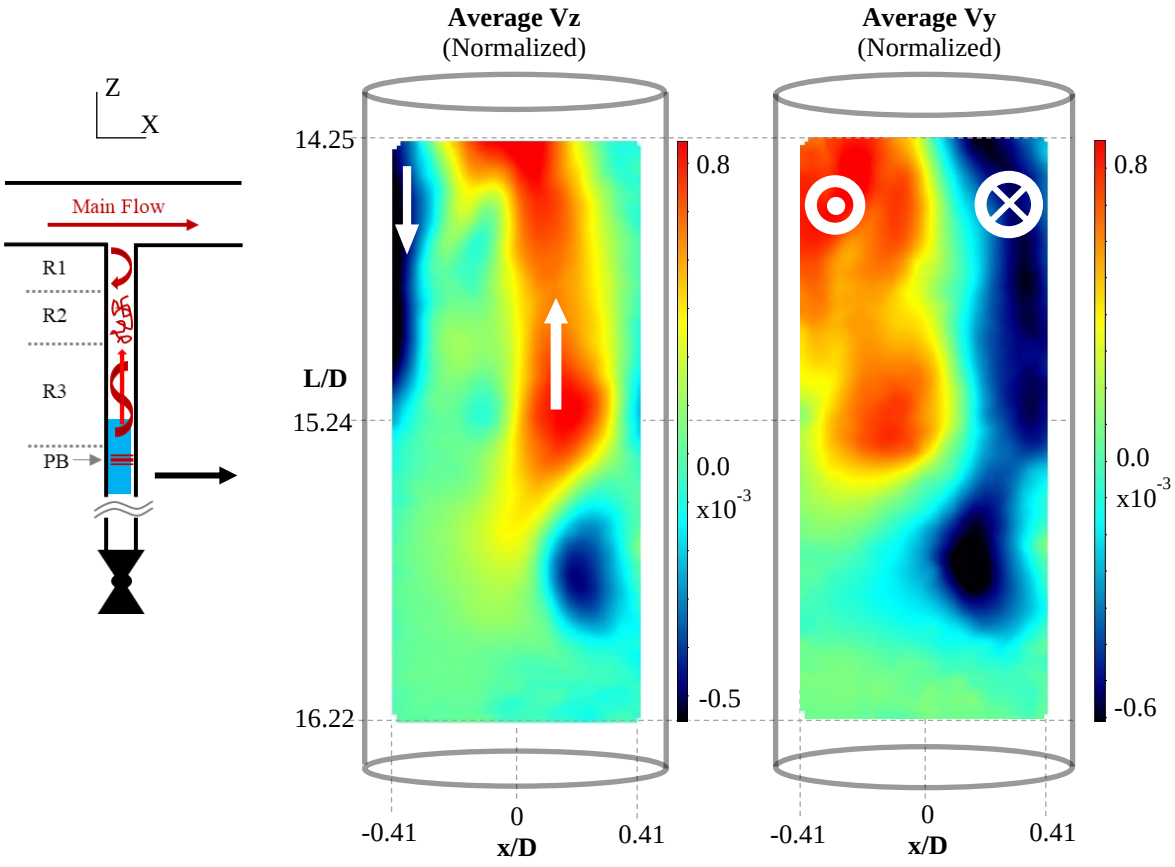

Figure 3-39 Measurement results of the penetration boundary reached by the branch line swirl.

line. As the max/min velocity magnitudes of the swirl and linear components of the flow reached parity, the vortex feature of the flow distorted and faded.

The effective end of the flow is also visualized here using a particle tracing representation as in Figure 3-40. Because T-PIV measurements rely on the movement of particles, where there is essentially no movement the particle "paths" cannot be traced. In this figure, the particles are being tracked over 25 frames. In the region highlighted with the gray arrow, the flow effectively terminates as there is a general void of track lines in the remaining portion of the volume (L/D ~ 16).

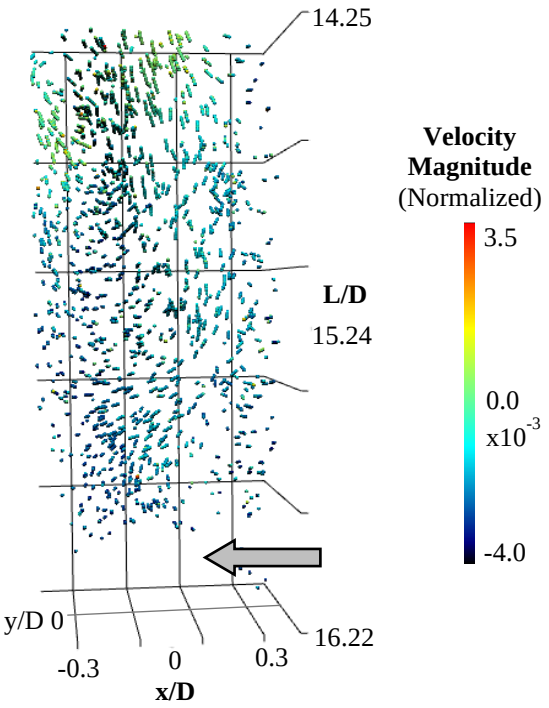

Figure 3-40 Particle tracing image of instantaneous velocity field. Component of average velocities presented in the previous figure.

Chapter 4 CFD efforts

CFD validation campaigns are dependent upon quality experimental data that capture the relevant phenomena. Using the data gathered so far, preliminary CFD simulations have been run to determine which models and boundary conditions will be best suited for the computational analysis of swirl penetration in branch lines [36]. Both T-PIV and LDV data for the SSEF and HCL facilities have been used for model validation.

4.1 SSEF Validation Efforts

As discussed in Section 3.4.4, the SSEF branch line swirl measurements of the high rpm cases present an interesting case for CFD RANS model validation work due to the well-defined boundary conditions and high-resolution of the data. This is primarily due to the T-PIV and LDV capture of the turbulent structure breakdown (the drop) that precedes the exponential decay portion of the branch line swirl. Seeing that this breakdown led to an early onset of the swirl's decay, it was of interest to see if this could be replicated numerically.

All simulations run for this case to date have failed to capture the drop accurately and have over predicted the swirl's penetration. The distinct drop in tangential velocity of the swirl in the measurement data does not appear in the simulations even after selectively altering factors like the slip boundary condition in segments of the piping. The persistence of the swirl well beyond the expected range from the measurements is likely a reflection of CFD RANS models that lack the

ability to accurately account for viscous decay forces both at the wall and within the fluid, given the drastic flow regime change. Further investigation and model application will be required.

Further investigation is underway (at the time of completing this dissertation) with multiple academic and industry partners within an OECD/NEA international benchmark, which uses selected data from the present dissertation. The high-resolution 3D velocity field data acquired from SSEF T-PIV measurements are the basis of a benchmark campaign for CFD RANS model validation.

4.2 HCL Validation Efforts

For the CFD model validation simulations regarding the data gathered from the HCL, Star-CCM+ was used exclusively. Best practices were observed in establishing the geometry and mesh utilized in the simulations [39, 40]. To reduce the demand of computational cells used for each simulation, two common practices were employed. First, the main line flow boundary conditions (velocity magnitude, turbulent kinetic energy, and turbulence dissipation rates, etc.) that would be used at the geometry inlet were established in a separate simulation. This was done by simulating flow through a straight, short segment of pipe with the same ID as the HCL. Utilizing a periodic boundary condition that would inform the flow "entering" the pipe based on the flow "exiting" the other end as the simulation progressed, allowed a fully developed turbulent flow profile to converge while using minimal computational resources [41].The Second, the main line pipe geometry about the branch line junction was halved using a symmetry boundary (Figure 4-1). Reducing the main line in this manner was justified by comparing separate simulations where the full main line diameter was preserved and where the

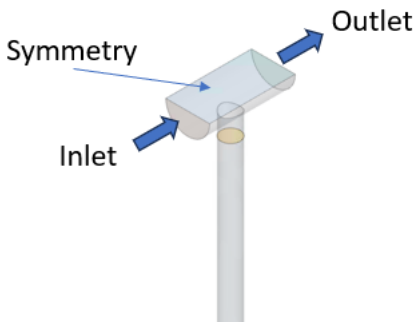

Figure 4-1 Resultant HCL facility geometry used for CFD simulations.

main line was halved. There was no discernible difference between the resultant velocity and turbulent kinetic energy fields around the branch line opening.

The resultant meshing scheme utilized uniformly distributed hexahedral elements. Having previous CFD meshing experience, the initial mesh generation base size selected was 2mm. For comparison, base sizes of 1.5mm and 1mm were also used to generate meshes. Although there was minimal observable difference between results from the 1.5mm case and the 1mm case, the mesh generated from the 1mm base size was used for all of the validation simulations conducted.

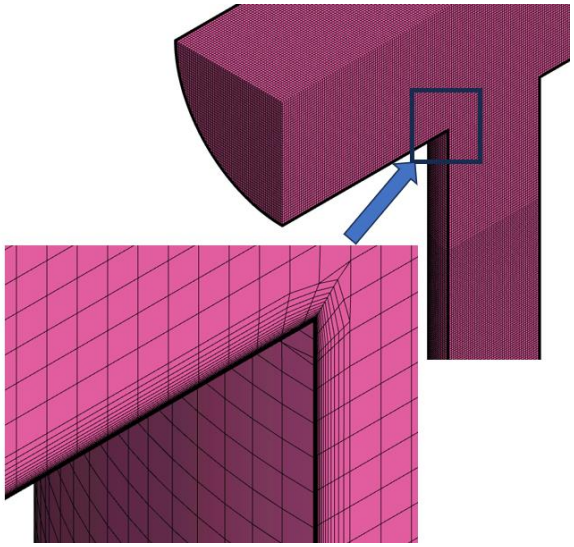

Figure 4-2 Visualization of a step in the mesh convergence process, highlighting near wall treatment.

CFD simulations of the involved flow phenomena have to account for the fully developed turbulent flow in the main line, the turbulent swirl in the branch line that transitions to laminar flow, and the near stagnation of the flow at the penetration boundary. The decaying aspect of the flow in the branch line highlights the need to properly estimate the friction generated at the branch line's pipe wall. To appropriately address the friction estimations, Reynolds-Averaged Navier-Stokes (RANS)

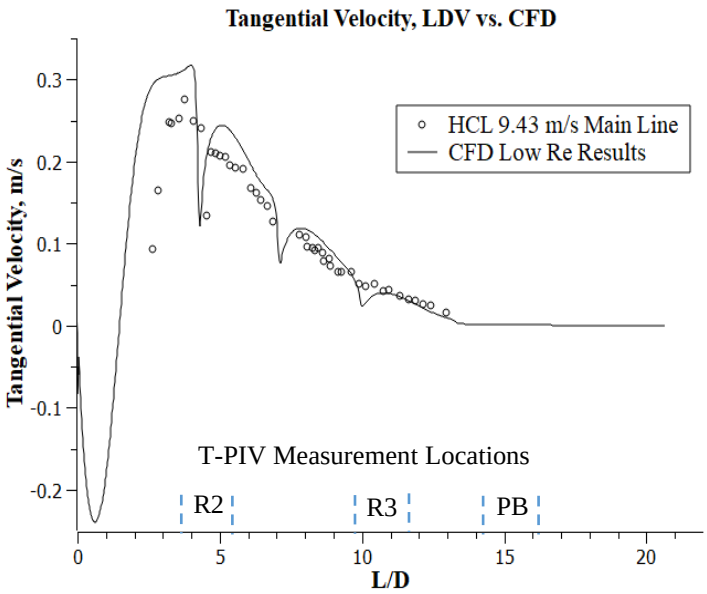

Figure 4-3 Measurement and CFD comparison. Positions of correlating T-PIV measurements denoted along x-axis.

models with a resolved, viscous sub-layer, such as SST-k-ω [41] and Low-Re k-ε [42, 43], were prime candidates. With special attention being given to the sub-layer, the near wall mesh was generated with an aspect ratio of 1.2, allowing a y+ <1 to be maintained.

In theory, flow dynamics surrounding the dead-ended branch line swirl case could be modeled using Direct Numerical Simulations (DNS). However, the practical implementation of DNS becomes infeasible due to computational costs. Key factors that drive the cost up are the Reynolds number of the main line (especially in the HCL cases) exceeding 1E6 and the need for high resolution meshing of wall layers to account for transitions to boundary layer turbulence [45, 46]. Additionally, the wide range of flow time-scales observed, which span from milliseconds in the main line to tens of seconds at the penetration depth within the branch line add complexity.

The feasibility of adopting a Large Eddy Simulation (LES) approach is equally challenging [46]. Accurate simulation of such flows necessitates the consideration of wall presence and its associated effects, a requirement that standard LES methodologies do not primarily address (see wall-resolved LES models [47]) As a result, this method also requires considerable computational resources and extended simulation durations.

Thus, given these considerations, the only viable alternative is the use of either Reynolds-Averaged Navier-Stokes (RANS) or Unsteady RANS (URANS) simulations. These approaches are significantly more computationally efficient. By selecting an appropriate turbulence model, they facilitate wall-resolved simulations with moderate computational demand.

One of the most widely used turbulence models is the Standard k-epsilon two-equation model [48, 49]. However, near the wall region, this model relies on semi-empirical formulas known as wall functions [50], and its application to flow patterns dominated by wall presence is debatable [51]. A specialized variant of the k-epsilon model, Standard k-ε Low-Re, addresses these

deficiencies by resolving the boundary layer region [43, 52]. Additionally, this model is capable of handling both laminar and turbulent flow regimes, as well as transitions between these regimes, being sensitive to periodic re-laminarization and transition, respectively.

To date, simulations using Low-Re k-ε turbulence models have yielded the closest results to measurement findings. As discussed in Sections 3.5.1 and 3.5.2, there were limitations to the physical ranges measured due to physical obstructions (opaque flanges) and camera viewing area. Figure 4-3 illustrates the range of the LDV and T-PIV measurements relative to the CFD results gathered [36]. As can be seen in the figure, the tangential velocity calculated in the simulation agrees well with the LDV measurements for $L/D > 4$. At positions of $L/D < 4$ there is greater disagreement, but the arc trend is still present in the CFD result. These same trends were present in the simulations of the other measured velocity cases presented in Section 3.5.1 as well.

Features that are readily visible in the discrepancy between the CFD data and that of the LDV results in Figure 4-3 are the "dips" near L/D = 5,7,10 in the CFD trends. These dips are also visible on a surface representation of the swirl 2 mm from the wall of the branch line as shown in Figure 4-4. It is evident in this surface representation of CFD results that the dips are products of azimuthal variation in the tangential velocity along the axis of the branch line.

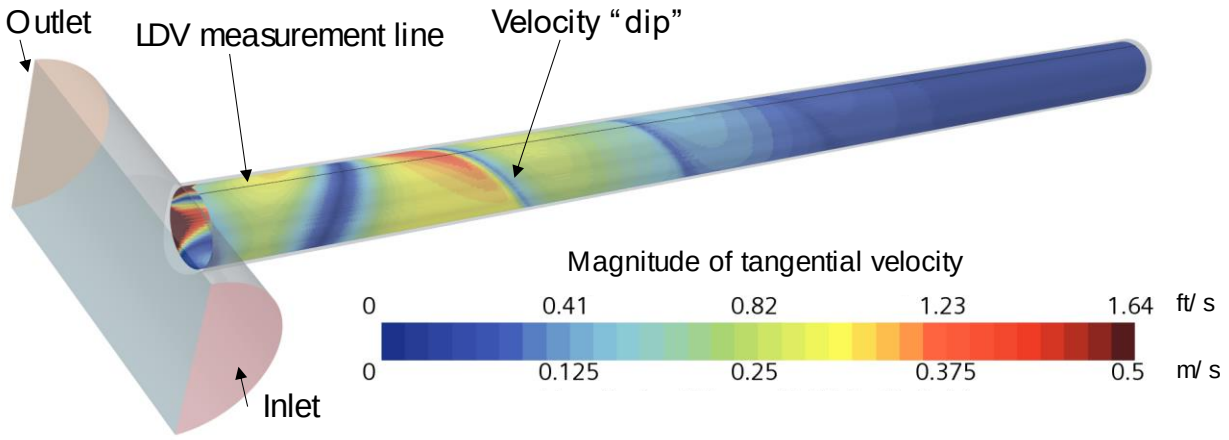

Figure 4-4 Simulation of HCL Conditions for Validation: Magnitude of Tangential Velocity on a Cylindrical Surface Located 2 mm from the Branch Line Wall.

The exact azimuthal description of the spiraling pattern, especially far from the main line, might not be predictable deterministically in simulations. However, looking at the azimuthal variation in the CFD results was instructive. Potential circumferential shifts in the CFD results of the tangential velocity were accounted for by plotting each velocity calculation along the branch line per azimuthal angle, as in Figure 4-5. Each red dot in Figure 4-5 corresponds with a velocity value along the circumference of the branch line surface from Figure 4-4 at each L/D position. As can be clearly seen, the tangential velocity values form a red band that closely follows the trend of the LDV data for L/D>3. Figure 4-5 presents a strong case for model agreement with measurement results, as all the LDV data points fall within the statistical cloud created by the extracted azimuthal CFD data. The decay trend of the flow swirl is also very well captured.

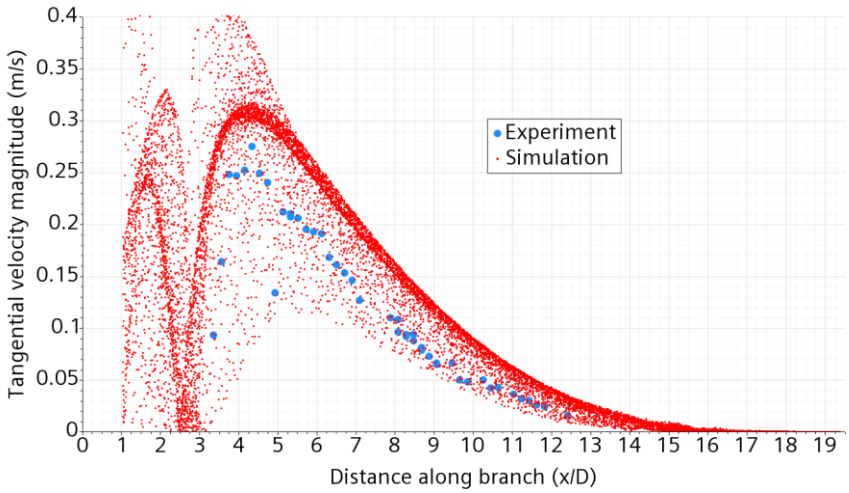

Figure 4-5 Comparison between LDV data and CFD results taken at all azimuthal angles along the branch line.

Although there was strong agreement between the tangential velocity trends of the branch line swirl in LDV measurements and CFD results, the overall flow fields, measured via T-PIV differed from CFD results in magnitude. As can be seen in Figure 4-6 to Figure 4-8, the CFD simulations resulted in higher magnitude flow conditions than what was observed in T-PIV measurements. With the over prediction of flow magnitudes, the CFD results naturally over predicted the penetration depth by more than a branch line pipe diameter (Figure 4-8). Although

this seems discouraging, in context of other CFD efforts and in comparison to the accuracy of current TF screening correlations, the result is impressive. Other models, such as the standard k-ε, yielded penetration depths that grew and grew with increasing iterations, ultimately reaching the full depth of the branch line. In the case of the Low-Re k-ε modeling, the swirl reaches a penetration point and does not continue penetrating after the simulation converges. This is owed to the fact that the Low Re model inherently factors in the viscous forces that diminish the laminar penetrating swirl's effects.

The flow characteristics of the swirl or vortex in the branch line measurements were present in the CFD results. This is most visible in Figure 4-6, where the axial flow is in the positive z-direction near the central portion of the flow for L/D > 3. The tangential velocity component of the flow is not as balanced in the CFD results about the axis as was measured using T-PIV (Figure 4-7). Notwithstanding, it is obvious that the vortex is calculated as expected from measurement findings. An aspect of the swirl's development in the CFD results that was interesting to observe was the break in the initial flow structures in the branch line near L/D = 3. Both velocity components make an interesting switch near that point, signaling a transition to the vortex flow from the initial entry flow. This inflection point corresponds well with the LDV findings discussed previously.

Although the CFD simulations to date have over predicted the penetration depth of the branch line flow, T-PIV measurement data is leading to more accurate results. A significant aspect of that improvement has come from capturing flow data of the tangential velocity and the axial velocity simultaneously. This is because the flow in the branch line quickly develops the axial

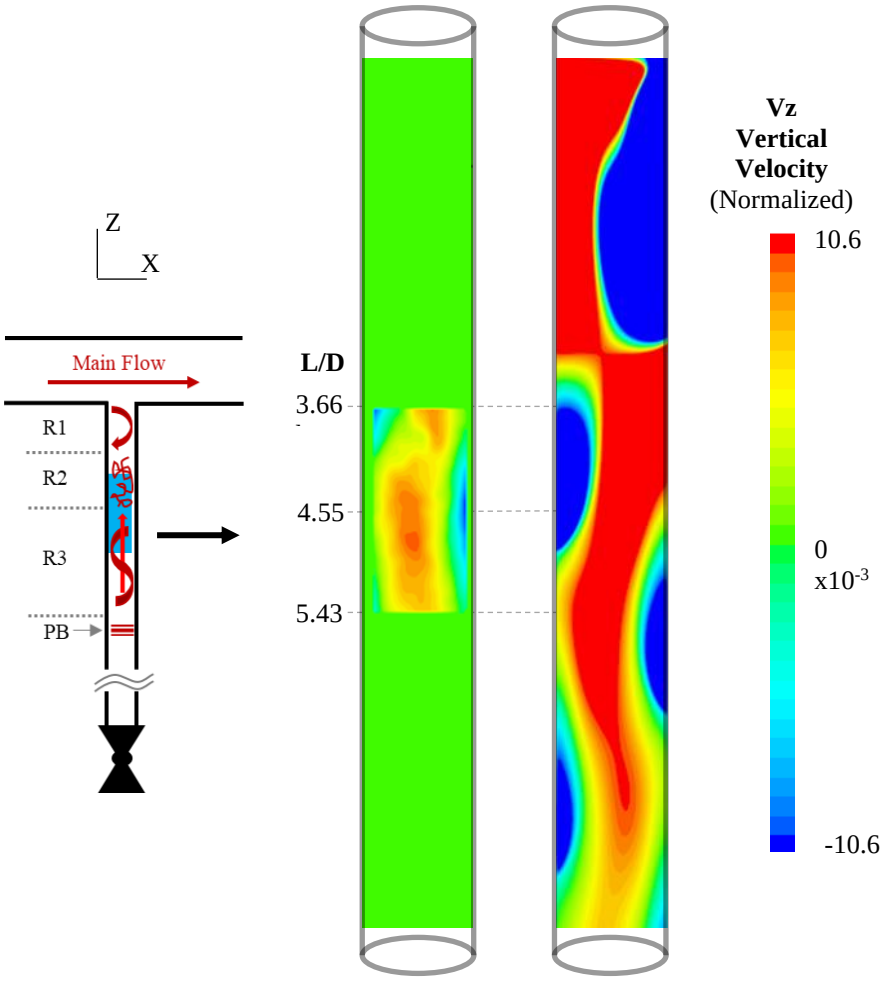

Figure 4-6 Measurement data vs CFD results for the 9.43 m/s main line velocity case. Vertical flow component.

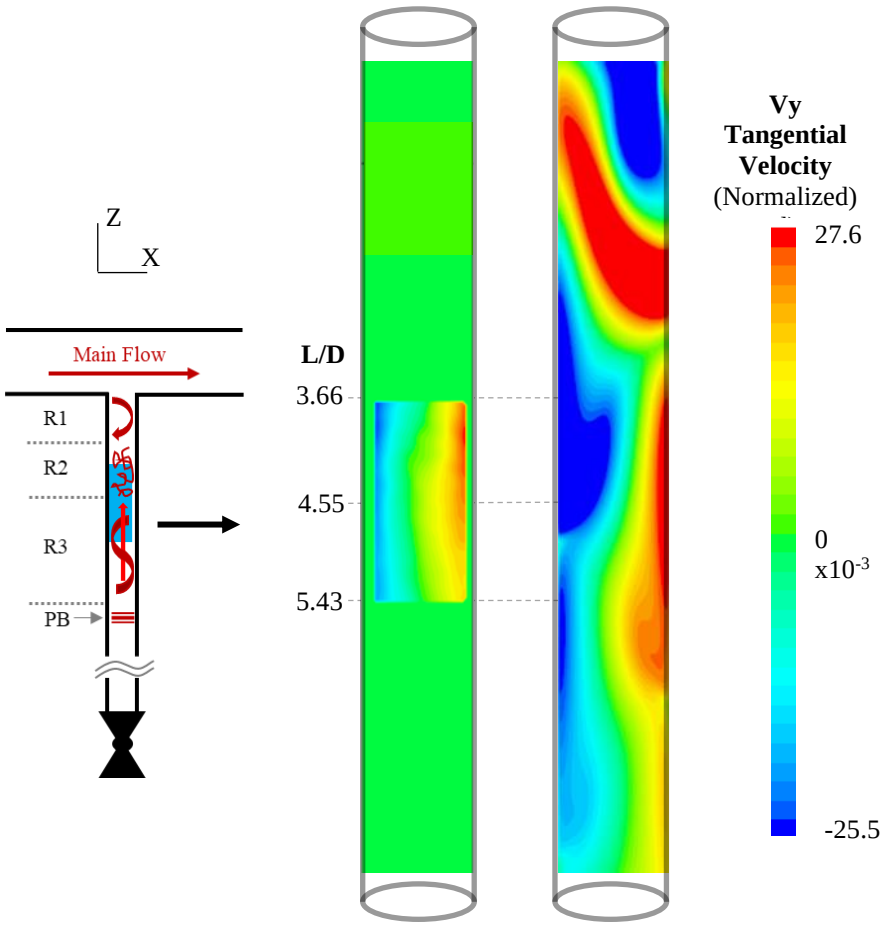

Figure 4-7 Measurement data vs CFD results for the 9.43 m/s main line velocity case. Tangential flow component.

swirl that persists in the branch line and drives the axial flow. Simultaneously quantifying the branch line flow components (in R3 in particular) allowed low Re models to be justified for CFD simulation.

Justifying Low-Re k-ε models for the simulation of branch line flows has significant benefits. Primarily, Low-Re k-ε models are computationally less expensive than other CFD models such as LES. Requiring less computational power allows sufficient simulations, like those shown in Figure 4-6 to Figure 4-8, to be accomplished with ~48 hrs iteration time on a standard desktop PC. Reducing the resources needed not only facilitates rapid iterative computational studies, but it makes CFD a more reasonable option for use in design modification studies for future power plant applications and for pipe maintenance screening efforts.

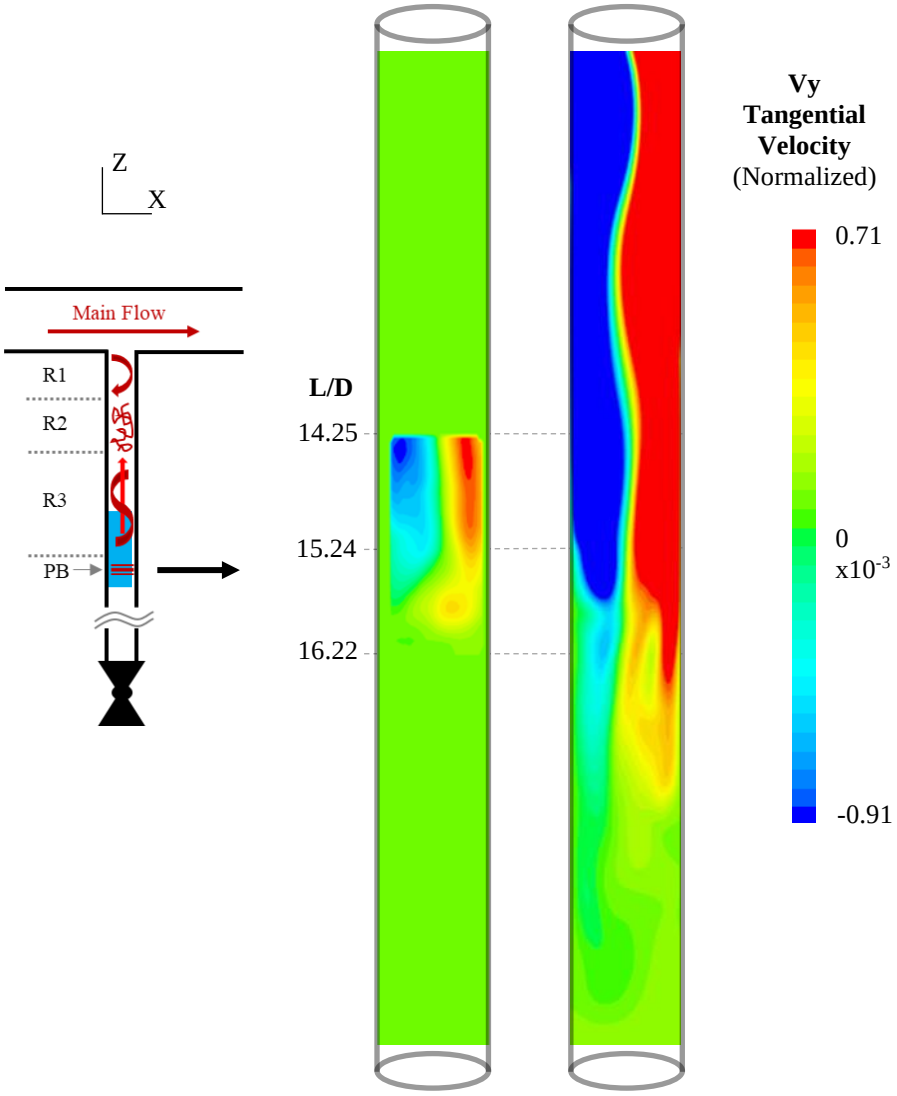

Figure 4-8 Measurement data vs CFD results for the 9.43 m/s main line velocity case near the PB. Tangential flow component

With further studies, CFD models will be validated from the T-PIV data being gathered. The T-PIV data gathered to date for CFD validation efforts is listed in Table 4-1. Emphasis has been given to collecting data about the penetration boundary region, as determining its location and fluctuation is a key driver of this work and it is critical that CFD accurately reports on this region.

Table 4-1 List of T-PIV measurements completed in the HCL branch line.

Region	Main line velocity case (m/s)
R2	7.3, 9.43
R3	5.97, 9.34
PB	5.53, 6.52, 7.94, 8.62, 8.85, 9.4

Chapter 5 Future Work

Further efforts to quantify the flow phenomena in isolated reactor coolant branch lines for CFD validation will involve studies that deviate from the current efforts in three major ways:

1. Changes to main line flow conditions. Initial cases were conducted with a fully developed, turbulent flow profile in the main line. Swirling the main line flow before or tripping the flow near the branch line opening of the branch line will facilitate validation efforts for other branch line opening boundary conditions. Preliminary CFD results show that a swirling main line flow can have a great effect on overall penetration depth. Such swirling in the main line is comparable to the effect of a circulation pump shortly upstream of a branch line opening.
2. Changes to piping geometry. The changes would include the alteration of the branch line opening geometry as discussed in Section 2.3.2 and the addition of elbows along the branch line (Figure 5-1). Penetrating flow interaction with elbows is of particular interest to the nuclear power industry as elbows are particularly susceptible to thermal fatigue failure.

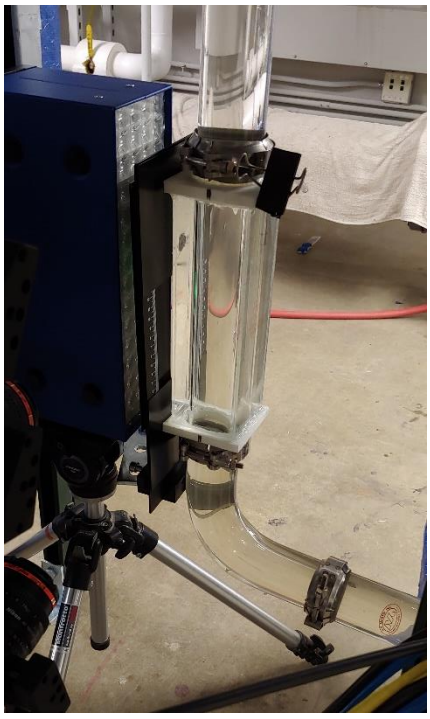

Figure 5-1 Elbow installed in the branch line piping of the HCL.

3. Non-isodensity fluid cases. For the measurements presented previously, isodensity conditions were maintained by using a single working fluid at any given time. However, the thermal fatigue phenomenon at the heart of this work is directly tied to the thermal/density differences between the stagnant branch line coolant and the coolant of the main line. To better understand the effect of thermal difference on penetration depth, two fluids of different density will be used in a measurement facility.

As data is collected, it will be used directly for CFD validation efforts and informing maintenance guidelines. This will include in-house CFD simulation campaigns as well as campaigns conducted by research partners at other institutions. The primary focus will be on validating lower cost models such as CFD RANS by appropriately adjusting the turbulence parameters.

Chapter 6 Conclusions

Experimental facilities to further the investigation of flow phenomena in dead-ended branch lines and for CFD validation were designed, built, and operated in the ECMF lab at the University of Michigan within the scope of the present dissertation. These facilities included a preliminary, low-capacity setup known as the ReBL-TF facility, the SSEF for investigating the branch line flow swirl in isolation, the RPL, which was adapted from the ReBL-TF facility to achieve NPP coolant line flow velocities through a rectangular main line channel, and the HCL, a high-capacity experimental loop for high flow velocities in the main line while maintaining a round main line cross-section.

Within these facilities, high-resolution measurements were conducted using LDV, PIV, and T-PIV methods. LDV pointwise measurements were able to capture details about the axial development and decay of the branch line swirl. PIV measurements established a foundation of velocity field data and exposed the need for simultaneous capture of the third velocity component (out of 2D plane). T-PIV measurements expanded the value of high-resolution measurements in the branch line as they captured 3D velocity field data. For the first time, quantitative high-resolution measurements have been made of the complex flow structures occurring in isolated branch lines.

This work has laid a solid foundation of high-resolution data and practical analysis to better understand the phenomena occurring in isolated branch lines. The experimental data collected is also suited for the validation of CFD models, which will enhance their predictive capabilities for

flow swirl characteristics and development in dead-ended branch lines akin to those found in NPP systems. To date, one CFD validation benchmark campaign has been initiated utilizing 3D velocity field data from the SSEF measurements referenced in this dissertation. The OECD/NEA international benchmark will bring together several academic and industry partners worldwide to validate CFD RANS models. In addition, the experimental database built within this dissertation work can aid the development of better and more accurate correlations for the prediction of swirl penetration depth in isolated branch lines.

Other relevant and supplementary findings are as follows:

- LDV tracking of the tangential velocity about the branch line axis in the HCL near the wall of the pipe identified an inflection point near L/D = 4. This may have been the cavity flow region's boundary proposed by reference [21], but given the discrepancy in determined location, it is unclear. The discrepancy most likely arises from the geometric differences between the two facilities used, which merits further investigation. The RPL was designed in part to facilitate such studies that more closely resembled those by the previous researchers by utilizing a rectangular main line flow channel.
- LDV measurements between the HCL and SSEF demonstrate that after initial swirl development, the decay behavior of the swirl as it approaches the penetration boundary is rather similar. The overall trend of decay is not significantly hindered or enhanced by the cascading disturbances seen in flow loop style measurements. Isolated swirl measurements, therefore, provide a reliable path forward to conducting certain branch line flow experiments with significantly lower complexity. The applicability of these experiments would only exclude flow cases where the effects of main line flow conditions or branch line opening are of interest.

- LDV measurements in the SSEF confirmed that the axial branch line swirl develops and decays in a similar fashion regardless of fluid's kinematic viscosity. Accounting for the kinematic viscosities role in the swirl's intensity can be adequately accomplished by considering its local Re* value.
- PIV measurements in ReBL-TF demonstrated that the average flow structures in R2 and R3 were similar. R2, the disturbed flow region as proposed by previous research, only differs from the vortex flow of R3 by the intensity and frequency by which the dominant swirl is impinged upon by upstream flow disturbances.
- PIV measurements in ReBL-TF of the penetration boundary quantified the effective depth of penetration in relation to main line velocity. The examination of turbulent kinetic energy in this region showed that increasing the main line velocity effectively lengthened the final entrainment portion of the vortex.
- Proper orthogonal decomposition of PIV data from radial cross-sections of ReBL-TF R3 showed that deviations in the flow behavior have relatively little individual effect. The average flow characteristics were shown to dominate the flow on time scales of seconds to tens of minutes.
- T-PIV measurements in SSEF quantified the expected flow characteristics in the R3 and PB portions of the branch line. Measurements showed that in R3, the axial swirl's tangential velocity component magnitude was greater than that of the axial velocity's component. At the extent of penetration, the velocity magnitudes of each component reach parity.
- T-PIV measurements in the upper portion of SSEF quantified a flow feature that was unintentionally introduced due to the facility's design. Aside from causing an earlier onset

of the decay region, this feature did not affect the flow of the swirl in the SSEF. The data of the flow feature presents an interesting, although directly separate from this work, case for CFD validation exercises.

- T-PIV measurements in HCL R2 and R3 added to what was gathered from ReBL-TF 2D measurements. R2 was found to exhibit a consistent average flow structure that could be resolved with less than two seconds of time resolved data. R3 contained the expected vortex-like flow previously measured in both the ReBL-TF and SSEF facilities. The overall nature and magnitudes of the flow in R3 between the HCL and SSEF cases differed only in that the HCL swirl was minorly disturbed by the competing flow phenomena.
- T-PIV measurements in the HCL about the PB revealed the expected flow magnitudes and characteristics that were previously observed in ReBL-TF and SSEF measurements. The L/D position to which the PB reached in the branch line was greater than predicted from the previously published correlations [21]. The discrepancy most likely arises from the geometric differences between the two facilities used, which merits further investigation. The RPL was designed in part to facilitate such studies that more closely resembled those by the previous researchers by utilizing a rectangular main line flow channel).

Bibliography

[1] R. Shumway, Nuclear Power Safety, Pergamon, 1976, pp. 281-302.

[2] J. D. Keller, A. J. Bilanin and S. T. Rosinski, "DEVELOPMENT OF A THERMAL FATIGUE SCREENING AND EVALUATION METHODOLOGY FOR PRESSURIZED WATER REACTOR PLANTS," in *Pressure Vessel Piping*, San Diego, California, USA, 2004.

[3] L. Hu and M. Kazimi, "LES benchmark study of high cycle temperature fluctuations caused by thermal striping in a mixing tee," *International Journal of Heat and Fluid Flow*, vol. 27, pp. 54-64, 2006.

[4] T. Frank, C. Lifante, H. M. Prasser and F. Menter, "Simulation of turbulent and thermal mixing in T-junctions using URANS and scale-resolving turbulence models in ANSYS CFX," *Nuclear Engineering and Design*, vol. 240, pp. 2313-2328, 2010.

[5] J. Westin, F. Alavyoon, L. Anderson, P. Veber, M. Henriksson and C. Anderson, "Experiments and unsteady CFD-calculations of thermal mixing in a T-junction," in *Computational Fluid Dynamics for Nuclear Reactor Safety*, Munich, Germany, 2006.

[6] H. Ayhan and C. N. Sokmen, "CFD MODELING OF THERMAL MIXING IN T-JUNCTION: EFFECT," in *The 15th International Topical Meeting on Nuclear Reactor Thermal - Hydraulics, NURETH-15*, Pisa, Italy, 2013.

[7] O. Braillard and D. Edelin, "Advanced experimental tools designed for the assessment of the thermal load applied to the mixing tee and nozzle geometries in the PWR plant," in *1st International Conference on Advancements in Nuclear Instrumentation, Measurement Methods and their Applications*, Marseille, France, 2009.

[8] J. M. Stephan and F. Curtit, "High-Cycle Analytical Thermal Fatigue Tests on Pipe Structures," in *ASMEDC*, Vancouver, BC, Canada, 2002.

[9] X. Schuler and K. H. Herter, "Thermal Fatigue due to Stratification and Thermal Shock Loading of Piping," in *30th MPA-Seminar in conjunction with the 9th German-Japanese Seminar*, Stuttgart, 2004.

[10] D. I. Song, Y. D. Choi and M. S. Park, "Experimental research for identification of thermal stratification phenomena in the nuclear powerplant Emergency Core Coolant System," in *Korean Society of Mechanical Engineers*, Jeonju, South Korea, 2001.

[11] A. Hernandez and B. Mallet, "EDF to review new nuclear repair strategy on Friday, source says," *Reuters,* pp. https://www.reuters.com/business/energy/edf-review-new-nuclear-repair-strategy-friday-source-says-2023-03-09/, 9 March 2023.

[12] A. Pecout and P. Mouterde, "Large crack discovered on nuclear power plant further complicates situation for France's EDF," *Le Monde,* pp. https://www.lemonde.fr/en/economy/article/2023/03/08/large-crack-discovered-on-nuclear-power-plant-further-complicates-situation-for-france-s-edf_6018624_19.html#, 8 March 2023.

[13] M. Roberts, "CORKSCREW FLOW PATTERN IN PIPING SYSTEM DEAD LEGS," Electricite de France, 1992.

[14] E. Deutsch, P. Montanari and C. Mallez, "Isothermal study of the flow at the junction between an auxiliary line and primary circuit of pressurised water reactors," *Journal of Hydraulic Research,* vol. 6, no. 35, pp. 799-812, 1997.

[15] H. M. Bel and O. Simonin, "Second-moment Predictions of Confined Turbulent Swirling Flow," in *Proc. 5 International Symposium on Refined Flow Modeling and Turbulence Measurements*, Paris, France, Sept. 1993.

[16] N. R. Commission, *NRC BULLETIN NO. 88-08, SUPPLEMENT 3: THERMAL STRESSES IN PIPING CONNECTED,* Washington, D.C.: NRC, 1989.

[17] J. Kim, A. Deardorff and R. Roidt, "Thermal stratification in nuclear reactor piping system," in *JSME/ASME joint international conference on nuclear engineering,* Tokyo, 1991.

[18] J. Kim, R. M. Roidt and A. F. Deardorff, "Thermal stratification and reactor piping integrity," *Nuclear Engineering and Design,* vol. 139, pp. 83-95, 1993.

[19] JSME, "Guidelines for Evolution of High-Cycle Thermal Fatigueof a Pipe," Japan Society of Engineers, 2003.

[20] N. Takenaka, S. Hosokawa, A. Saito, T. Oumaya, A. Nakamura and K. Miyoshi, "EXPERIMENTAL STUDY ON TEMPERATURE FLUCTUATION PHENOMENA IN A CLOSED BRANCH PIPE CONNECTING TO HIGH VELOCITY AND HIGH TEMPERATURE FLOW IN A MAIN PIPE," in *International Heat Transfer Conference*, Washington D.C., 2010.

[21] T. Iguchi, A. Saito, N. Takenaka, K. Miyoshi and A. Nakamura, "EXPERIMENTAL STUDY ON PENETRATION LENGTH IN A SMALL SIZE BRANCH PIPE IN A NUCLEAR POWER PLANT," in *International Topical Meeting on Nuclear Reactor Thermalhydraulics*, Toronto, 2011.

[22] K. Miyoshi and A. Nakamura, "INVESTIGATION OF FLOW STRUCTURE TO PREVENT THERMAL FATIGUE IN A DOWNWARD BRANCH PIPE WITH A CLOSED END," in *Pressure Vessels and Piping Conference*, Waikoloa, Hawaii, 2017.

[23] N. KASAHARA, T. ITOH, M. OKAZAKI, Y. OKUDA, M. KAMAYA, A. NAKAMURA, H. NAKAMURA, H. MACHIDA and M. MATSUMOTO, "Development of thermal fatigue evaluation methods of piping systems," *E-Journal of Advanced Maintenance* , vol. 6, no. 1, pp. 14-23, 2014.

[24] T. Lu, H. Li and X. Zhu, "Numerical simulation of thermal stratification in an elbow branch pipe of a tee junction with and without leakage," *Annals of Nuclear Engineering*, vol. 60, no. 1, pp. 432-438, 2013.

[25] H. Ikeda, K. Nakada and T. Murofushi, "Prediction of Thermal Stratification Phenomena In a Branch Pipe Using Numerical Simulation," in *International Conference on Nuclear Engineering,*, Nagoya, Aichi, 2007.

[26] B. J. THOMPSON and E. WOLF, "Two-Beam Interference with Partially Coherent Light," *JOURNAL OF THE OPTICAL SOCIETY OF AMERICA*, pp. 895-902, 1957.

[27] P. M. Doran, Bioprocess Engineering Principles, Elsevier Ltd., 2013.

[28] M. Raffel, C. Willert, S. Wereley and J. Kompenhans, Particle Image Velocimetry - A Practical Guide, Springer, 2007.

[29] M. Raffel, C. Willert, S. Wereley and J. Kompenhans, Particle Image Velocimetry - A Practical Guide, Springer, 2007.

[30] K. Peiponen, R. Myllyla and A. Priezzhev, Optical Measurement Techniques, Springer, 2009.

[31] G. Elsinga, F. Scarano and B. Wienke, "Tomographic particle image velocimetry," *Experiments in Fluids,* vol. 41, pp. 933-947, 2006.

[32] F. Scarano, "Tomographic PIV: principles and practice," *Measurement Science and Technology,* vol. 24, no. 1, 2013.

[33] B. Wienke, "Improvements for volume self-calibration," *Measurement Science and Technology,* vol. 29, no. 8, 2018.

[34] G. Elsinga, J. Westerweel, F. Scarano and M. Novara, "On the velocity of ghost particles and the bias errors in Tomographic-PIV," *Experiments in Fluids,* vol. 50, 2011.

[35] N. Takenaka and A. Saito, "EXPERIMENTAL STUDY ON TEMPERATURE FLUCTUATION PHENOMENA IN A CLOSED BRANCH PIPE CONNECTING TO HIGH VELOCITY AND HIGH TEMPERATURE FLOW IN A MAIN PIPE," in *International Heat Transfer Conference,* Washington DC, 2010.

[36] *Various MRP reports, personal communications,* Electrical Power Research Institute.

[37] J. Nikuradse, "Gesetzmassigkeiten der turbulenten stro-mung in glatten rohren," *Forschung auf dem Gebiet des Ingenieurwesens,* Vols. (Translated in NASA TTF-10, 359, 1966), no. 3, pp. 1-36, 1932.

[38] E. Szwabowski, "M4 Aerospace Engineering," 2020. [Online]. Available: https://www.m4-engineering.com/q-criterion-for-vortex-visualization/. [Accessed 10 May 2021].

[39] S. Rodriguez, Applied Computational Fluid Dynamics and Turbulence Modeling - Best Practices of the CFD Trade, https://doi.org/10.1007/978-3-030-28691-0_6: Springer, 2019.

[40] N. Martins, N. Carrico, H. Ramos and D. Covas, "Velocity-distribution in pressurized pipe flow using CFD: Accuracy and mesh analysis," *Computers & Fluids,* vol. 105, pp. 218-230, 2014.

[41] W. Munters, C. Meneveau and J. Meyers, "Shifted periodic boundary conditions for simulations of wall-bounded turbulent flows," *Physics of Fluids,* vol. 28, no. 2, p. https://doi.org/10.1063/1.4941912, 2016.

[42] F. Menter, "Two-Equation Eddy-Viscosity Turbulence Models for Engineering Applications," *American Institute of Aeronautics and Astronautics,* vol. 32, no. 8, p. https://doi.org/10.2514/3.12149, 1994.

[43] K.-Y. Chien, "Predictions of Channel and Boundary-Layer Flows with a Low-Reynolds Number Turbulence Model," *American Institute of Aeronautics and Astronautics,* vol. 20, no. 1, pp. 33-38, 1982.

[44] V. C. Patel, W. Rodi and G. Scheuerer, "Turbulence Models for Near-Wall and Low Reynolds Number Flows: A Review," *American Institute of Aeronautics and Astronautics,* vol. 23, no. 9, pp. 1308-1319, 1985.

[45] I. Marusic, B. McKeon, P. Monkewitz, H. Nagib, A. Smits and K. Sreenivasan, "Wall-bounded turbulent flows at high Reynolds numbers: Recent advances and key issues," *Physics of Fluids,* vol. 22, no. 6, p. https://doi.org/10.1063/1.3453711, 2010.

[46] I. Celik, "RANS/LES/DES/DNS: The Future Prospects of Turbulence Modeling," *Fluids Engineering,* vol. 127, no. 5, p. https://doi.org/10.1115/1.2033011, 2005.

[47] S. Kawai and J. Larsson, "Wall-modeling in large eddy simulation: Length scales, grid resolution, and accuracy," *Physics of Fluids,* vol. 24, no. 1, p. https://doi.org/10.1063/1.3678331, 2012.

[48] J. Bardina, P. Huang and T. Coakley, *Turbulence Modeling Validation, Testing, and Development,* USA: National Aeronautics and Space Administration, 2013.

[49] N. Takemitsu, "An Analytical Study of the Standard k–ε Model," *Fluids Engineering,* vol. 112, no. 2, pp. 192-198, 1990.

[50] D. Lacasse, E. Turgeon and D. Pelletier, "On the judicious use of the k–ε model, wall functions and adaptivity," *International Journal of Thermal Sciences,* vol. 43, no. 10, pp. 925-938, 2004.

[51] X. Albets-Chico, C. Perez-Segarra, A. Olivia and J. Bredberg, "Analysis of wall-function approaches using two-equation turbulence models," *International Journal of Heat and Mass Transfer,* vol. 51, no. 19-20, pp. 4940-4957, 2008.

[52] Y. Nagano and M. Tagawa, "An Improved k-epsilon Model for Boundary Layer Flows," *Journal of Fluids Engineering,* vol. 112, pp. 33-39, 1990.

[53] LaVision, *Particle Image Velocimetry - Product Manual*, 2018.

[54] H. M. Merklinger, Focusing the view camera, H. M. Merklinger, 2010.

[55] Y. Ishikawa and Y. Okuda, "NUMERICAL ESTIMATION OF FLOW PENETRATING DEPTH INTO STAGNANT BRANCH PIPES FOR THERMAL FATIGUE PREDICTION," in *Pressure Vessels & Piping Conference*, Anaheim, CA, 2014.

[56] J. Downing, V. Petrov and A. Manera, "Flow Structure in Dead-Ended, Coolant Loop Reactor Branch Lines Related to Thermal Fatigue Onset," in *NURETH-18*, Portland, OR, 2019.

Appendix A

CFD simulations can vary greatly if modeling parameters are not properly applied. One measure used to ensure that the model is meshed properly is the y+ value. This non-dimensional number is essentially a way of determining how models (RANS, k-ε in this case) will treat the flow as it transitions from a bulk turbulent flow to a laminar boundary layer flow near the wall. Figure A- 1 illustrates the wall treatments of two separate simulations related to the discussion about main line diameter sizing studies in Section 2.3.1. The trends exhibit the expected behavior in each region: a linear relationship between the dimensionless velocity and wall distance (U+ and y+), in the viscous sublayer, a departure from that relationship in the buffer layer, and a trend that mimics the log-law in the next region.

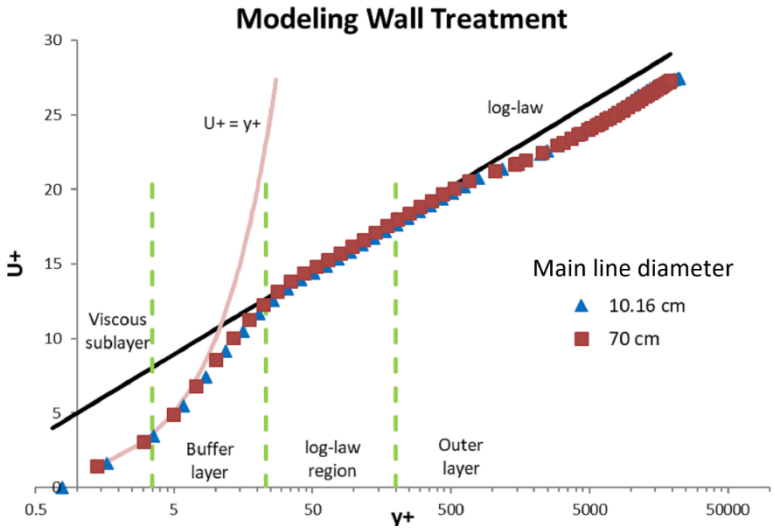

Figure A- 1 Modeling wall treatment of two simulations with two different main line diameters, highlighting the proper treatment of meshing in the boundary layer.

Additional simulation results, complementing those discussed in Section 2.3.1, are shown in the figures below. Figure A- 2 focuses on velocity magnitudes within the branch line, showing similar trends for the two main line diameters examined. Figure A- 3 adds to the plots shown in Figure 2-14 and Figure 2-15, showing velocity and turbulent kinetic energy results for the "Plane 2" cross-section.

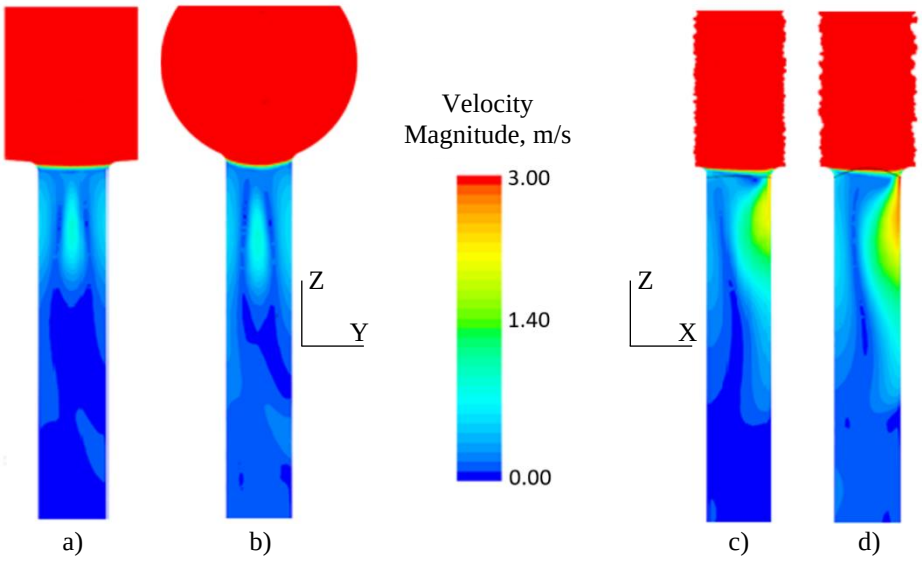

Figure A- 2 Time-averaged velocity magnitude (capped at 3 m/s) from preliminary CFD results. Main line diameters: a,c) 70 cm, b,d) 10.16 cm. Cross-sections: a,b) viewing angle colinear with main line axis, c,d) viewing angle perpendicular to the main line axis. These results were used to inform the design of the main line diameter.

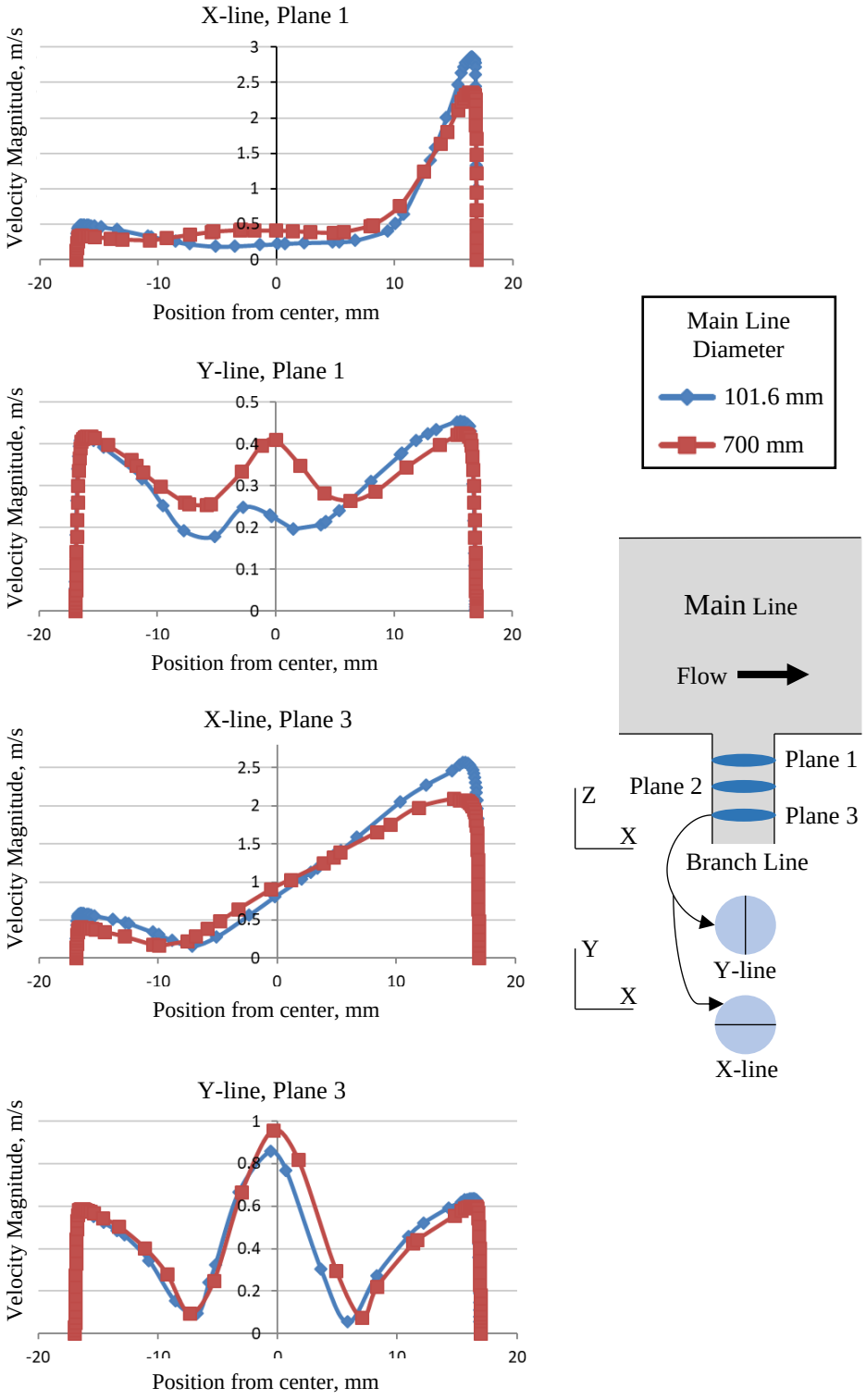

Figure A- 3 Time-averaged velocity and TKE profiles from preliminary CFD results. These results were used to inform the design of the main line diameter.